GEOMATICS SYNTHESIS PROJECT

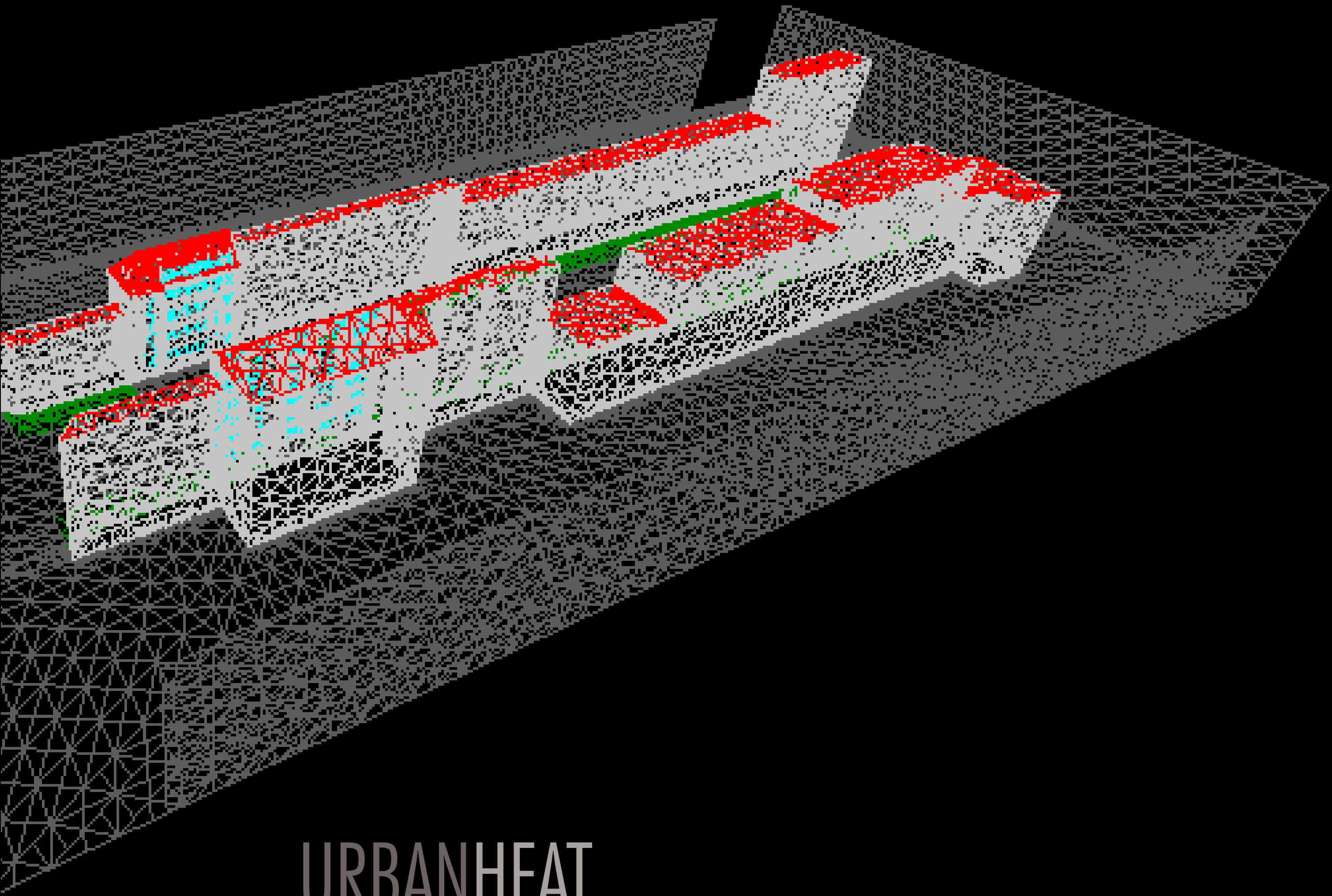

URBANHEAT

The effect of 3D geometry complexity on simulating radiative, conductive and convective fluxes in an urban canyon.

Submitted by	Supervisors
1312227 Roeland Boeters	Prof. Dr. Massimo Menenti
1356461 Sjors Donkers	Dr. Ir. Ben Gorte
4180941 Danbi Lee	Ir. Edward Vebree
1504541 Vera Liem	
4184084 Sina Montazeri	
1216813 Jelte van Oostveen	
1280155 Peter Pietrzyk	

GM2100 - Geomatics Synthesis Project | 8 November 2012

TU Delft Delft University of Technology in partnership with LSIIT

Abstract

The Geomatics Synthesis Project (GSP) is an eight-week culminating group project by seven second-year MSc. Geomatics students. The objective was to undertake group and fieldwork through a real-world project with an external organization. In association with Laboratoire des Sciences de L'Image Informatique et Teledetection (LSIIT) at the University of Strasbourg, the 2012 GSP explored the impact of 3D geometry complexity on the accuracy of simulating radiative, convective and conductive fluxes in an urban canyon. The research involved the collection of meteorological data near the urban canyon in Strasbourg, France, for input into a model called LAtent, SEnsible, Radiation Fluxes (LASER/F), which simulates the aforementioned fluxes. The preparation of seven geometry scenarios with different complexities was completed and test run in LASER/F. The results were validated with thermal images of two facades collected during the field campaign in Strasbourg. The results show that LASER/F systematically underestimates facade surface temperatures due to various model assumptions. One of those is the oversimplified 1D parametrization of the wind and was demonstrated by comparing it with a vertical wind profile extracted from a Computational Fluid Dynamics (CFD) model. Nevertheless, it was concluded that the most complex 3D geometry does not necessarily improve simulation accuracy, especially during warming periods of the day. The inclusion of balconies on the facades is influential and should be used for future simulation experiments when it is a significant feature of the facade. Further research is required to better understand canyon geometry effects such as canyon orientation, aspect ratio and the volumetric influence on internal heat storage in buildings.

Acknowledgements

Our first thanks goes to our supervisors Massimo Menenti, Ben Gorte, and Edward Verbree who since the inception of this project have been most enthusiastic and supportive of realizing our vision for the GSP. They challenged us to think critically in answering our research question, and it was by their interest, advice, and guidance that we have been able to learn and experience work found within the entire Geomatics information chain. Of course we could not have executed this project without Jérôme Colin, Françoise Nerry, Pierre Kastendeuch, Georges Najarr, Laure Roupioz and Robin Faivre of the LSIIT group at the University of Strasbourg. It was only through a partnership with them that we could define our research question and receive generous technical and scientific support. Their gracious hospitality toward us in our two week visitation to their research lab and homes was an invaluable and memorable experience. Thanks also to Patrick Schrijvers of the Transport Phenomena group at Delft University of Technology (TU Delft) for allowing us to utilize the TU Delft CFD model to enhance our analysis. The consistent technical training, feedback, and support were constructive moments in our learning process that we could not have done without. Finally, we thank our guest speakers of the GSP Symposium who kindly volunteered to present their research highlights to a public audience.

Contents

List of Figures

Acronyms

aGPS assisted GPS.

ASCII American Standard Code for Information Interchange.

ASE ASCII Scene Export.

CAD Computer-Aided Design.

CFD Computational Fluid Dynamics.

DGPS Differential Global Positioning System.

FLIR Forward Looking InfraRed.

FoV Field of View.

GDOP Geometric Dilution Of Precision.

GPS Global Positioning System.

GSP Geomatics Synthesis Project.

GUI Graphical User Interface.

LASER/F LAtent, SEnsible, Radiation Fluxes.

LoD Level-of-Detail.

LSIIT Laboratoire des Sciences de L'Image Informatique et Teledetection.

RANS Reynolds Averaged Navier-Stokes.

RMSE Root Mean Square Error.

SVF Sky View Factor.

TKE Turbulent Kinetic Energy.

TU Delft	Delft University of Technology.
UBL	Urban Boundary Layer.
UCL	Urban Canopy Layer.
UHI	Urban Heat Island.
VRML	Virtual Reality Modeling Language.

Chapter 1

Introduction

The GSP is an opportunity for second year MSc. Geomatics students to undertake real-world Geomatics research as a small group; practising skills in acquisition, visualization, processing, analysis and interpretation of geospatial data. The GSP also allows students to practice fieldwork, group work and project management with external research institutes and/or companies.

This year the GSP continues to align with the TU Delft Climate City Campus initiative, a campaign to model and simulate climate conditions in urban environments, using the TU Delft campus as a local laboratory. In the 2012 edition of the GSP, the research was conducted in collaboration with the LSIIT group of the University of Strasbourg, France.

The general objective of the GSP was to contribute to a new three-year research campaign by LSIIT on simulating radiative, conductive and convective fluxes in an urban canyon using a model called LASER/F. This campaign is interested in measuring and modelling the air quality of cities, where the Urban Heat Island (UHI) effect plays an important role in pollutant dispersion models. A two-week workshop and field campaign was undertaken from September 10^{th} to September 21^{st}, 2012, wherein the GSP group worked on-site in the urban canyon and at the LSIIT laboratory to acquire the needed data and train in the LASER/F model, among other things. Upon returning to Delft, the group worked to post-process the gathered data, run the 3D geometry simulations on LASER/F, and validate the results.

The LASER/F model has been used in combination with data obtained from a measurement campaign by LSIIT in 2002 for similar research on heat flux in urban canyons [7]. However, the geometry used to run the model was relatively simple. Thus it was the specific goal of the GSP to determine the sensitivity of the LASER/F model to various levels of detail in the 3D geometry of the urban canyon, including surface properties (materiality) and general vegetation effects. This is believed to provide valuable insight into the level of effort that is required to accurately model radiative, convective, and conductive fluxes in an urban canyon and thus better simulate flux patterns within entire cities. An important part of the methodology was to validate the outputs of the model by comparing it to thermal images of two specific facades in the canyon.

Based on the results, the GSP aimed to advise on how the LASER/F model could be improved or best utilized. On one hand, the research results will inform to what level of detail 3D geometry should be prepared in order to achieve satisfactory results that balance accuracy, precision and time. This leaves the LASER/F model untouched. On the other hand, the vertical wind profile used by LASER/F was placed in question as the results of a CFD model suggested an area for improvement.

The intent of this final report is to outline the purpose, objectives, research approach, methodology, results and discussion of the research project. It also provides a detailed process review in Appendix A. The results of the research are expected to be of interest to urban climatologists, policy planners and architects challenged with modelling the urban heat at the canyon scale.

1.1 Problem statement

The UHI effect is an anthropogenic phenomena of interest to urban climatologists, health professionals, urban planners and architects. By the settlement and building-up of land, an artificial macro- and micro-climatic condition is shaped whereby the temperature in the urban area is elevated compared to neighbouring rural areas. For cities that experience hot summers, this could potentially add several degrees to the experienced warmth in a city, possibly creating discomfort and unhealthy living conditions. There are also concerns that the entrapment of heat by cities increases the attenuation of air pollutants in the city, leading to various public health and environmental effects.

Of interest in studying UHI is the influence of urban morphology. How aspects of the urban 'surface' (or urban fabric) influence UHI is important to understand in order to change the way urban areas are built and managed. Research in this area characterizes processes of urban heat flux into two physical layers: the Urban Boundary Layer (UBL) (troposphere depth until the top of the average height of roofs) in studying macro-scale flux processes, and the Urban Canopy Layer (UCL) (the depth from top of roofs to the ground) in studying micro-scale flux processes [8]. The flux between the layers can be studied, but this research project looked specifically within the UCL.

The urban fabric is composed of buildings arranged in blocks and separated by roads. This organization creates a variety of urban canyon geometries. The geometry, materiality, and vegetative coverage of the urban canyon is thought to influence heat and turbulent fluxes, and thus its overall contribution to UHI at the macro-climatic scale (city-wide). The parametrization of flux processes at the canyon scale could improve prediction models of UHI effect and air pollution dispersion. Models utilizing 3D geometry (such as LASER/F) have been developed to simulate radiative, conductive and convective fluxes in an urban canyon. CFD models for canyons can also simulate turbulent fluxes and generate wind profiles. However, the sensitivity to the level of detail in 3D geometry complexity had not been tested yet with LASER/F.

1.2 Approach, hypothesis, and sensitivity testing

The LASER/F model was initially developed to obtain more precise estimates of radiative, conductive, and convective fluxes at the UCL, using a generalized 3D representation of urban canyon geometry and materiality, in order to determine the influence of the urban canyon on the overall heat generated in an urban area. Here the urban canyon behaves as one object in a collection of objects in a city. The details of the urban canyon are not considered as important as its overall contribution to UHI.

However, the GSP examined a finer level of detail to challenge the position that canyon details are insignificant - not only at the boundary of the urban canopy layer, but also within it. The hypothesis was that the level of detail does influence the accuracy of the model, especially with respect to the characteristics and design of the building facades. If true, it follows then that 3D geometry complexity also influences the simulated fluxes at the top of the canyon, and therefore its overall contribution to UHI in an urban area. Thus the experimentation with LASER/F is really a sensitivity test to 3D geometry complexity.

LASER/F takes as an input various meteorological conditions at the urban canopy layer to initialize the simulation (forcing conditions). Thus, this model needed as an input (i) the 3D geometry (at various levels of detail) and (ii) the meteorological data for forcing conditions (air temperature, relative humidity, air pressure, wind speed and direction). The CFD model from TU Delft was intended to be used as a third input, whereby the CFD simulation could parametrize the wind profile for LASER/F. However, the scope of this research component was limited to the comparison of vertical wind profiles between LASER/F and the CFD model. The output of the LASER/F simulations were compared with thermal measurements taken on-site.

The many parts of this research approach involved the utilization of knowledge in photogrammetry, Global Positioning System (GPS), 3D modelling and visualization, literature review on urban climatology and general project management.

1.3 Project process

The GSP was planned as a four-phased process to be completed in eight weeks. Prior to initiating the GSP, the group engaged in a planning process to secure the project with LSIIT and generate preliminary research questions that were refined in phase I. Following the completion of this final report, a symposium was held on 8 November, 2012 where the GSP outcomes were presented to a public audience.

Phase I (week 1) kicked-off the GSP with meetings between the students, LSIIT and TU Delft supervisors Massimo Menenti, Ben Gorte and Edward Verbree. Here project and research objectives were clarified and preparations were made for the field campaign in Strasbourg in phase II (week 2 and 3). The literature review was also initiated and completed in phase III.

The field campaign in Strasbourg included training on the LASER/F model, the instruments for measuring meteorological conditions near the urban canyon, and use of a Forward Looking InfraRed (FLIR) thermal camera. A standard meteorological station was set-up and operational for five consecutive days. A 24-hour measurement campaign of surface temperatures of two facades in the canyon were also taken. Meanwhile, the complex 3D geometry set of the urban canyon for the LASER/F model underwent preparation (different levels of generalization were implemented). Details of the methodology are found in Chapter 5 and Chapter 6.

Phase III (week 4 to 6) involved the running of LASER/F with prepared 3D geometry scenarios, running the CFD wind model to generate a vertical wind profile, and the processing of the thermal images for comparison to the LASER/F simulations. The end of this phase involved the validation and interpretation of the results against the research question. Phase IV wrapped-up the project with the generation of recommendations for future studies and the preparation of the final presentation and GSP symposium. The overall flow of the research approach is outlined in Figure 1.1.

To ensure that project and course objectives were being met, weekly allocation meetings were held by the GSP team. Weekly follow-up meetings with supervisors were scheduled in order to seek advice and guidance on setting a methodology and interpreting results. The GSP team self-organized into various team roles and divided into sub-groups based on interest and ability in particular tasks. This is detailed in Appendix A.

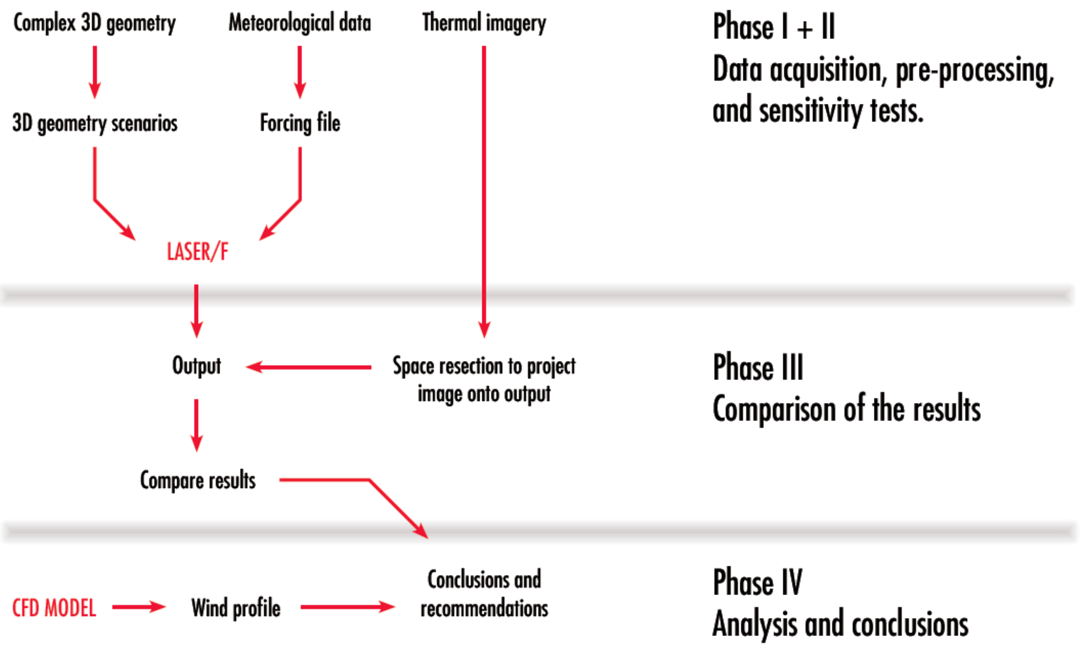

FIGURE 1.1: Overall research approach and process to the 3D geometry complexity sensitivity test of LASER/F

Chapter 2

Urban climate studies

Investigating and analysing the climate of urban areas began in the early 1800's with the work of Luke Howard who made daily measurements of the pressure, temperature, humidity, precipitation and evaporation in rural and urban areas to pinpoint the climate difference between them [9]. The urban population increased from approximately 0.75 billion in 1950 to 3.63 billion in 2011 and if this trend continues, in the year 2050 almost 6.25 billion people will be urban dwellers [10], it is no surprise that interest in urban climatology has steadily increased. Concerns about air pollution, energy consumption, and liveable urban climates has brought together research from a variety of disciplines examining urban regions to urban canyons [11]. This chapter is organized as follows:

Section 2.1 gives a brief introduction of the UHI phenomenon and its causes and effects on urban climate. Section 2.2 explains the urban energy balance followed by Section 2.3 which describes in details the effects of urban geometry, surface heating, and wind turbulence. Finally, Section 2.4 explains each term of the urban energy balance equation mathematically.

2.1 Urban Heat Island effect

A popularized phenomena stimulating research in urban climatology is the Urban Heat Island effect. According to U.S. Environmental Protection Agency [12], the UHI effect is when "...urban and suburban areas experience elevated temperatures compared to their outlying rural surroundings; this difference in temperature is what constitutes an urban heat island." Based on various works by Dr. Tim Oke, a pioneer researcher in the field, urban climatological studies can be divided into two physical domains: the Urban Canopy Layer and the Urban Boundary Layer. The UCL is the layer from the ground up to the mean roof level (including the atmosphere and built environment), whereas the UBL is the atmospheric layer above the mean roof level to (often) the top of the troposphere (Figure 2.1). While UHI can be based on the surface or air temperature, the most common UHI studies are focussed on air temperatures within the UCL [13].

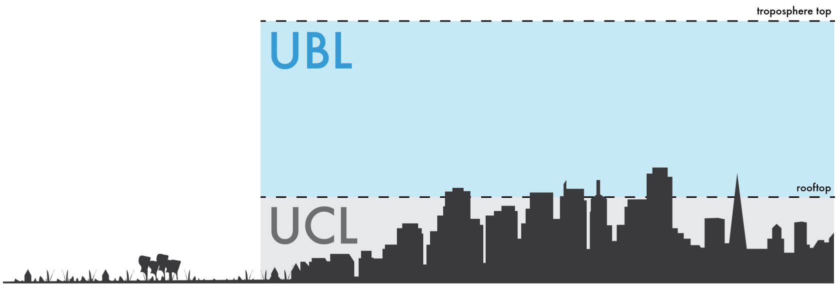

Figure 2.1: Conceptual diagram illustrating UBL and UCL

Based on the literature by Oke [8], Rasheed and Robinson [11] and Kleerekoper et al. [14], it seems that the strength of the UHI phenomenon is strongly dependent on geographic location, size and the meteorological conditions of the urban area. This means that urban morphology has a significant role to play in UHI mitigation strategies since cities cannot be moved nor climates changed.

UHI is caused by a combination of heat generation (by anthropogenic sources), heat retention (by increased surface area of materials with low albedo and high heat storage capacity, reduced sky views, lower latent heat flux due to reduced vegetation, and reduced turbulent heat transport), and heat entrapment (by canyon geometry or down-reflected radiation by greenhouse gases) Figure 2.2.

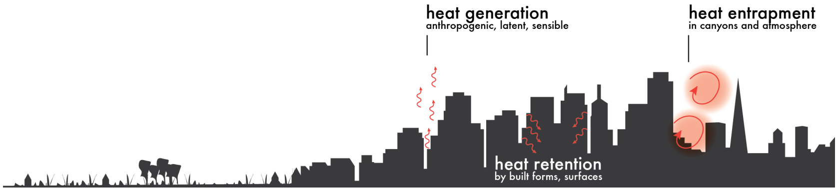

Figure 2.2: Overview of UHI causes

This may lead to an uncomfortable urban climate, air pollution accumulation and shifts in energy consumption levels. Furthermore, UHI effect is more pronounced at night than during the day, because of the slow release of heat by the city compared to rural areas (Figure 2.3). UHI could be mitigated by increasing surface albedo, sky view factor, vegetation and flowing water bodies (throughout the city). However the efficacy of each intervention will depend on the city's location and macro-climatic conditions.

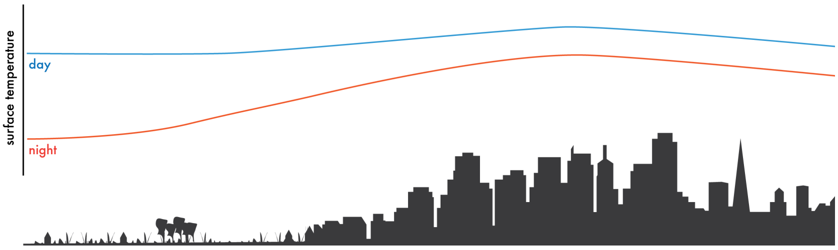

Figure 2.3: UHI is more pronounced at night than during the day

2.2 Urban energy balance

To further elaborate on the causes of UHI it is necessary to understand the energy balance of urban areas. It must be taken into account that these causes stem from several energy exchange processes at different scales, which can be divided into processes at meso-scale (10^{-2} to 10^3 m) and at micro-scale (10^4 to $2 \cdot 10^5$ m). While the energy balance processes observed at any scale are similar, they are affected by spatial variability of the surface such that as scale decreases, spatial variability in general decreases, and the influence of surface details can be increasingly generalized [15].

The concept of scale hence plays a fundamental role in the urban energy balance models. As was aforementioned, the UCL extends from ground level to the mean roof level. Its energy balance is mainly controlled by micro-scale, site-specific characteristics and processes [15]. The UBL extends from above the mean roof level up to the top of the troposphere and is mainly controlled by the exchange of heat between the city and the atmosphere above it [16]. Moreover, the UCL and UBL layers interact and a plethora of research has been focussed on describing this relationship [11, 17].

An overview of radiative processes in the UBL is shown in Figure 2.4. Incoming solar radiation (1) is partly scattered back by particles in UBL and partly transmitted (2) towards the surface. A part of the directly received radiation is then absorbed by the surface and the rest is reflected back into the UBL (3). Here again a part is transmitted, but also a part is scattered back (4) and absorbed by the surface. The long-wave part of the radiation (thermal radiation) is mainly responsible for heat exchange from the surface to the air. It can be seen that long-wave radiation is emitted from the surface (5). This radiation is then partly absorbed by the layer. Further incoming long-wave radiation from the sky (6) is either absorbed by the layer or transmitted to (7) and absorbed by the surface. The last flux is the absorbed long-wave radiation by the UBL, which is re-emitted to the sky and to the surface (8), where it is absorbed.

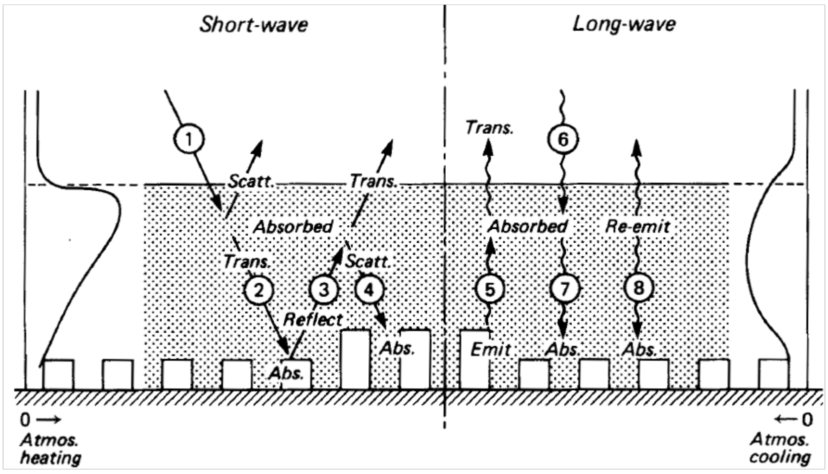

FIGURE 2.4: Overview of radiative processes in the Urban Boundary Layer

2.3 Urban canyon studies

Based on the previously mentioned concept of balancing energy, it is conceivable that just a fraction of the incoming solar radiation eventually reaches the UCL where the same processes of reflection, scattering, absorption and transmission are observed at the surfaces of the urban fabric. This incoming amount must again be balanced within the UCL, since energy cannot be created nor destroyed. A common scale of research in the UCL is at the urban canyon level.

There are several ways to describe the urban fabric as a surface type. It can be parametrized by its texture or physical heterogeneity and related to air turbulence phenomena [2]. Moreover, in this way, different land use types could be parametrized. For example, surface roughness of a Canadian suburban residential area would likely be different from a typical dense and compact Dutch city centre.

The urban fabric is organized into blocks and streets, with blocks generally being built up to the block edge, forming walls that frame the streets. The experience of the street at ground-level is thus shaped by the roadway down the middle and a street wall on either side. When this pattern is consistent along the entire block, this geometry compilation is called an urban canyon. It is interesting to research the radiative, conductive and convective fluxes within a canyon because it can improve predictions at the top of the UCL, thus more accurately determining its contribution to the UHI effect in a city.

Oke [1] defines a basic urban canyon to be made up of the following components: (i) the floor, (ii) the walls and (iii) the air mass in between the walls. The sky above could be considered a fourth component, as it is a sink for outgoing terrestrial long-wave radiation [2, 18]. The idealized, or ‘regular’, urban canyon is symmetric about the centre of the road and consists of two long uniform volumetric blocks with flat roofs, flanking either side of the canyon floor (Figure 2.5). The materials of the walls would behave homogeneously (heat capacities, albedo and emissivity). Of course this is not a realistic assumption, but is often necessary to implement such control variables for research.

The literature suggests that there are three overarching features to characterize an urban canyon with respect to impact on micro-climate: geometry, surface properties and vegetation (Figure 2.6). In this research project, of concern was geometry and to some extent, the effect of vegetation.

Urban canyon geometry is described by the (1) orientation (cardinal direction), (2) aspect ratio and (3) Sky View Factor (SVF) (Figure 2.7). The orientation of the canyon describes the direction of the street in relation to a referenced north. This is important because it determines the coverage and incidence angle of direct solar radiation and thus solar gain by canyon surfaces [19]. The aspect ratio is the ratio of canyon height to width (H/W). This is an important index of the building massing in relation to the street and

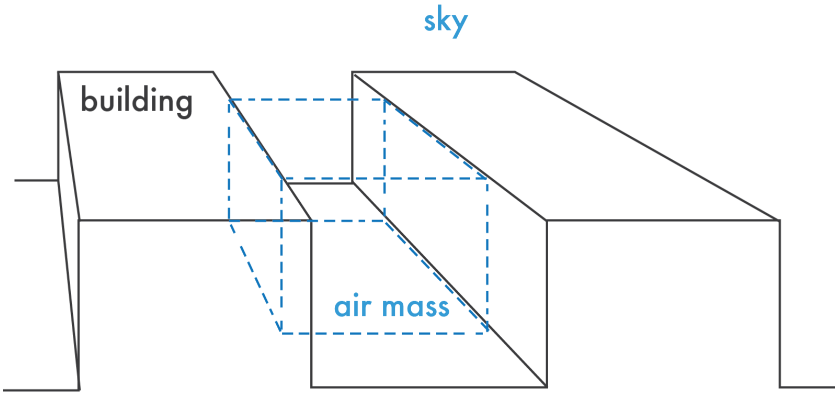

FIGURE 2.5: Conceptual diagram illustrating the idealized, or 'regular' urban canyon (adapted from Oke [1])

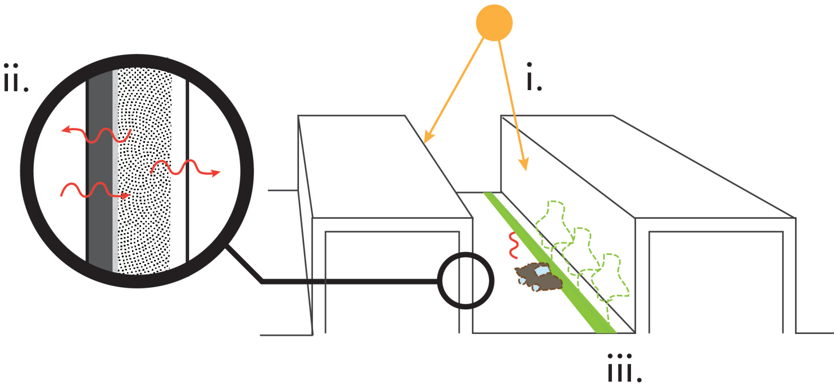

FIGURE 2.6: Three overarching features to characterize an urban canyon (i) canyon geometry, (ii) surface properties, (iii) street vegetation and furniture causing mechanical turbulence

has an implication on the SVF and thus the amount of heat gain by the canyon surfaces and heat dissipation through the sky.

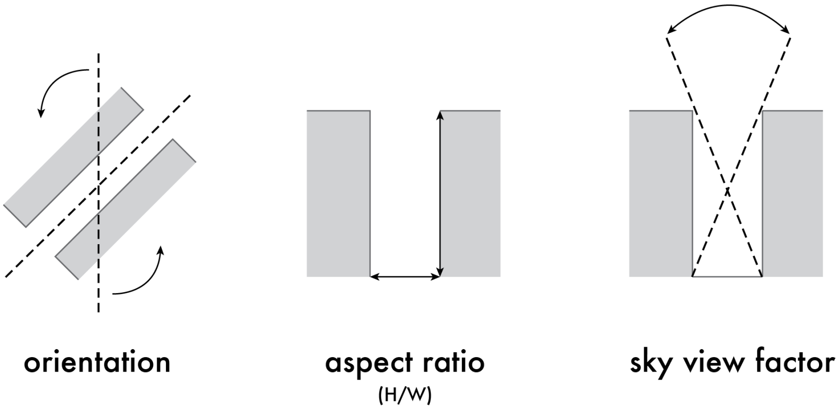

FIGURE 2.7: The geometry of an urban canyon can be described by orientation, aspect ratio and sky view factor

The SVF is an index (between 0 and 1) of the sky visibility from a given point in the canyon. This is an important variable because the sky acts as a net heat sink from the canyon. In general, a smaller SVF (for example, due to a narrower canyon) decreases the flux of heat out of the canyon top and heat can become trapped. However, more shading and isolation from the sky decreases the total amount and time of direct solar radiation reaching canyon surfaces, resulting in cooler canyon air temperatures [18]. This seemingly contradictory concept can be further examined.

Takebayashi and Moriyama [19] compare both east-west and north-south oriented streets against surface temperature measurements in Tokyo. They determined that for north-south streets, any shadowing effect of a tall building in the canyon has less of an impact on solar gain than for east-west streets. This can be intuitively understood. Thus, the conflicting effects of shading versus heat entrapment in a canyon is less pronounced in a north-south oriented street, where the aspect ratio is more relevant to the capacity to release heat to the sky above.

Takebayashi and Moriyama [19] also claim that in the summer the majority of net solar gain was found in the roofs of buildings rather than the floor and walls of the canyon. This suggests that mitigating roof albedo might have a significant role in attenuating UHI effect at the top of the UBL. Susca et al.'s study of green roofs determined the added thermal resistance helps regulate building temperatures in winter and summer (and thus less energy is expended by buildings) [20]. A white roof (high albedo) also has a similar effect.

The relationship between aspect ratio, wind speed and air temperature has also been studied. Memon et al. [21] have run simple 2D simulations to generate vertical isothermal profiles of street canyons of eight different aspect ratios using fixed synoptic (top-of-canyon) wind speeds. When the canyon was uniformly heated or wall-heated, a strong positive correlation between air temperature and aspect ratio was found. This suggests that increasing building heights has a net warming effect. This corresponds to the discussion on SVF and heat entrapment. There was also a strong negative correlation between wind speed and average air temperature, suggesting a net cooling effect of wind. Oliveira Panão et al. [22] have shown that narrow canyons in windy conditions entrap air and reduce thermal losses, whereas wide streets have increased thermal losses. However, if a narrower canyon with taller buildings (high aspect ratio) also has increased vertical wind speed along canyon walls, the cooling effect of wind might negate the heat entrapment by the geometry.

Many studies have simulated and measured the air turbulence of an urban canyon in all three dimensions (e.g. [2, 3, 23]). In particular, a nice overview of the air turbulence patterns is given in Vardoulakis et al. [24]. When the wind is on an oblique angle to the canyon orientation, the wind spirals through the canyon which can be an effective ventilation mechanism, but the effect depends on the strength of the synoptic winds. Most studies examine the effect of aspect ratio on the eddy formations within and the relationship between turbulence and air pollutant concentration. A canyon with a low aspect ratio observes isolated roughness flow of cross-winds (perpendicular to the canyon orientation), where the air flow does not become trapped in the canyon [2] (Figure 2.8). This corresponds to Oliveira Panão et al. [22]'s study of aspect ratio and thermal losses.

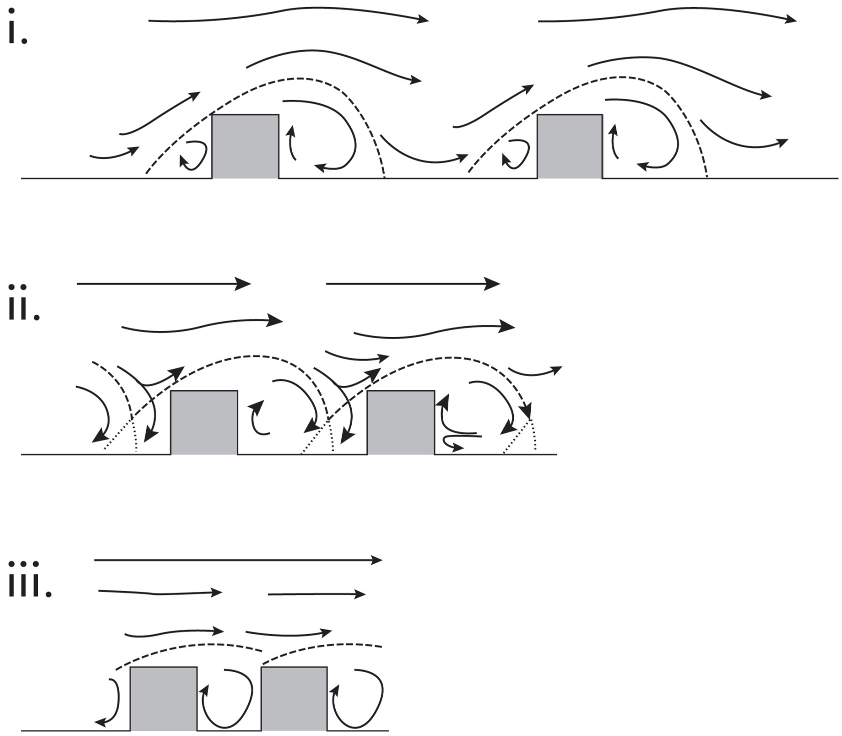

Figure 2.8: Turbulence in canyons created by cross-winds at ¿ $1.5 - 2\,\mathrm{m\,s^{-1}}$ for various aspect ratios (i) isolated roughness flow, (ii) wake interference flow and (iii) skimming flow (adapted from Oke [2])

The heating of canyon walls also stimulates convective heat exchange (results in rising, buoyant air) that is also affected by surface roughness. Moreover, the contribution of convective heat exchange to the overall energy balance becomes increasingly important with decreasing thermal resistance of the facades [25].

Higher aspect ratios of a regular symmetrical urban canyon with a cross-wind creates a major eddy formation toward the windward side and a minor counter circulation pattern on the leeward side [24]. Asymmetric configurations (termed step-up or step-down, with respect to the direction of the cross-wind) show similar eddy formations but with different intensities and shapes(Figure 2.9).

This aligns well with experiments on the concentration of air pollutants in canyons due to cross-winds, where the highest concentrations can be observed in the minor eddy formation, on the leeward side, where there is also somewhat warmer air temperatures and lower kinetic energy in the same areas [21, 26, 27]. However it should be noted that the turbulence profile changes throughout the day. Xie et al. [3] show that the profile and the pollutant concentration depends on the surface which is being heated (leeward, windward, or ground), which changes during the day as the sun moves across the sky.

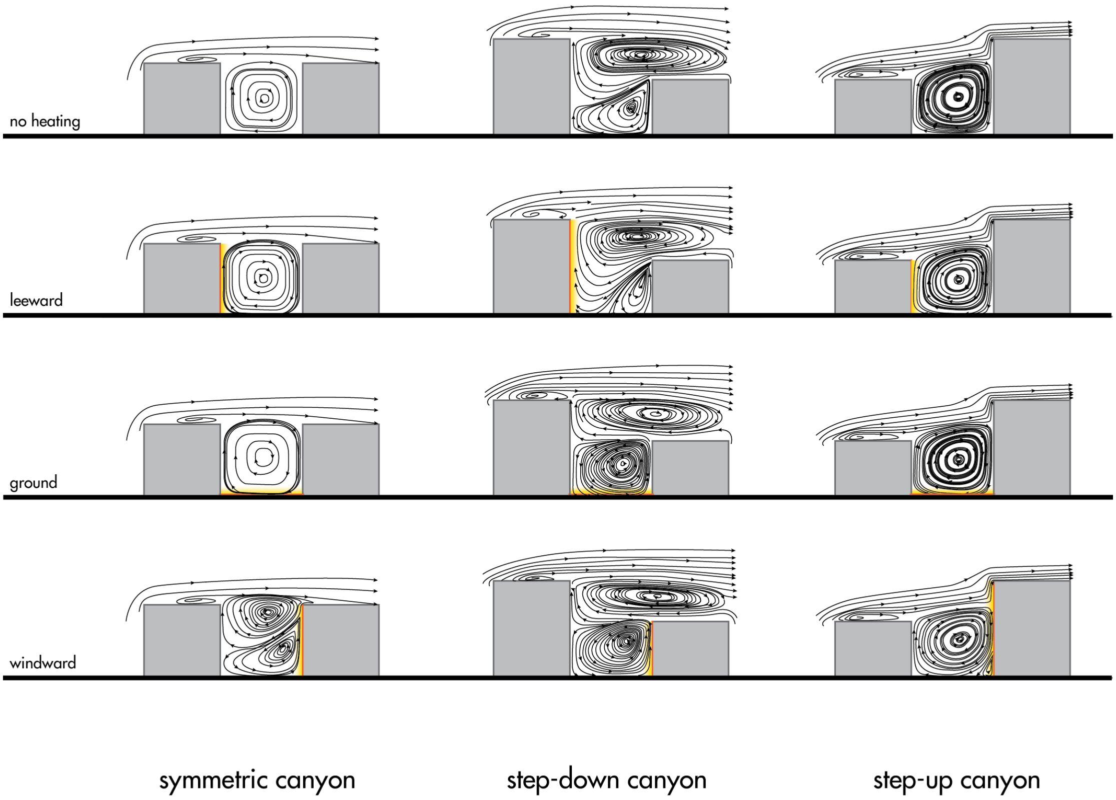

FIGURE 2.9: Expected vertical wind profiles of various canyon aspect ratios and surface heating scenarios - Given a cross-wind of 2m/s, different heating scenarios will change the circulation pattern in the canyon by creating buoyant air (adapted from Xie et al. [3]).

Vegetation, and other street furniture, also create mechanical air turbulence leading to complex air flow patterns near the ground [28]. Tree-lined streets add shading that decreases surface heating, but it also increases latent heat flux through evapotranspiration (by being a convective heat sink). This can attenuate some heating effects due to canyon geometry alone. However, the effectiveness depends on the tree variety and leaf temperature and therefore geographic location and season [29].

A complete picture of the relationship between geometry, surfaces and vegetation can be made from these studies. With an increasing aspect ratio, heat will be trapped since the SVF is decreased and eddy formation is favoured over a skimming flow. However, due to the increased shading effect there is also decreased solar gain and therefore less air heating by surfaces. This is apparently more pronounced in east-west oriented streets. However, when a surface is heated, adjacent air becomes more buoyant and affects the turbulent flow processes, but probably not enough to move air through the entire canyon and only enough to better mix the air within. Vegetation and street furniture (like news stands) may also generate smaller eddies that trap heat and pollution.

Streets with tall buildings in cities that experience more windy weather might not have such a pronounced effect of a reduced SVF since increased wind helps to transport heat out of a canyon, especially when it is parallel or the aspect ratio is small (isolated roughness flow). But this is not a desirable pedestrian condition. A comprehensive story of the relationship between the variables - air temperature, surface temperature, air turbulence profile, surface heating and buoyant air, vegetation and street furniture, aspect ratio, SVF and pollution concentration - has yet to be told in good theory but the current research points toward some compelling trends.

2.4 Surface energy balance

To understand the phenomenon of UHI and the influence of urban canyons on meso-scale level, one must have a clear understanding of the surface energy balance processes at the UCL scale. In Section 2.2 a clear first insight is given on the parameters that influence the energy balance at the surfaces within the urban canyon. All presented formulas will relate to the physics behind LASER/F as described in Section 4.2. The link between the theory of the surface energy balance and the implementation of this balance in LASER/F can also be found there.

2.4.1 Energy balance equation

The basic surface energy balance equation (Equation 2.1) accounts for all exchanges of energy on a specific surface by simulating all radiative, latent, sensible and surface heat fluxes that act in the UCL [30]. The assumption is that this surface is homogeneous in its radiative, thermal and geothermal properties [31]. If not, then the surface has to be fragmented into different elements so that the surface energy balance can be calculated for each element individually, which is the case for LASER/F and thus discussed in more detail in Section 4.2.

$$Q^* = K^* + L^* = Q_H + Q_E + Q_G (\mathrm{W\,m^{-2}}), \tag{2.1}$$

In Equation 2.1, Q^* represents the net wave radiation describing the sum of the net short-wave (solar) radiation K^* and the net long-wave (infrared) radiation L^*. The right hand side of the equation describes the non-radiative heat transfer mechanisms: the sensible heat flux Q_H, the latent heat flux Q_E and the (sub)surface or ground heat flux Q_G.

Sensible heat flux is equal to the amount of heat released by a substance with a resulting change in temperature. This is related to convection and conduction phenomena. The latent heat flux is the heat emitted or absorbed when changing states, without a change in temperature. Evapotranspiration and condensation are related to this quantity. Boiling water is an example of a latent heat flux since energy is released in the form of water vapour, but the temperature remains unchanged. As discussed in the previous chapter, vegetation in an urban canyon will provide shading but also an increased latent heat flux through evapotranspiration. Ground heat flux describes the energy exchange between the surface and sub-surfaces of the Earth, regulated by the heating and cooling of the surface. Heat-exchange processes between different layers in the ground have their influence on the ground heat flux.

The urban energy balance is the sum of all separate energy balances of each individual surface in the urban canyon, weighted to the size of the surface [32]. To mark the differences between the energy balance applicable to UBL and to UCL, Equation 2.2 which holds for the UBL is formulated.

$$Q^* + Q_F = K^* + L^* = Q_H + Q_E + \Delta Q_S + \Delta Q_A, \tag{2.2}$$

In Equation 2.2, Q_F represents anthropogenic heat flux, which is the flux caused by human activities. Often, a value at the top of the UCL is taken which can represent the effect of chimneys, air-conditioning etc. Furthermore, ΔQ_S and ΔQ_A are the storage and advective heat fluxes, respectively. The first term comprises the absorption and emission of heat by air flow in the urban space, integrated with the previously discussed ground flux. The second term represents the heat flux caused by advection along the vertical edges of the considered volume [32].

As the focus of this research is on the processes within the UCL, so processes in the UBL will not be elaborated further.

2.4.2 Short-wave radiation (K*)

The short-wave radiation K^* in Equation 2.1 consists of two parts: incoming and outgoing solar radiation. In this subsection the derivation of these terms is discussed. Incoming short-wave radiation is the amount of direct solar radiation that is incident on a surface. Outgoing solar radiation can be interpreted as the reflected solar radiation by terrestrial surfaces. Incoming and outgoing parts of the short-wave radiation are given in Equation 2.3.

$$K^* = K\downarrow + K\uparrow, \tag{2.3}$$

In Equation 2.3, $K\downarrow$ is the total incoming short-wave radiation and $K\uparrow$ the sum of all outgoing short-wave radiation. All incoming solar radiation is given by Equation 2.4.

$$K\downarrow = S + D, \tag{2.4}$$

Where S is direct solar radiation and D the diffuse solar radiation. The first term only takes the contribution directly from the sun into account. The latter one consists of two parts: the diffuse radiation from the sky (atmospheric diffuse radiation) and reflected radiation from the environment (reflected terrestrial radiation).

The terrestrial reflected radiation originates from all objects on the earth's surface. Complex geometry influences the surface energy balance through this term. Therefore it will be an important term to consider within this project. The reflected radiation D in the incoming radiation equation is different from the one in the outgoing term of the short-wave radiation (Equation 2.5). The distinction between the two can be explained as the incoming reflected radiation D being the sum of all outgoing (thus reflected) short-wave radiation for the surfaces that have a line of sight with the 'receiving' surface. The outgoing solar radiation is related to the incoming solar radiation through Equation 2.5.

$$K \uparrow = \alpha K \downarrow = (1 - \zeta_{short}) K \downarrow, \tag{2.5}$$

Where α is the albedo, the reflecting power of a surface. The albedo can be determined for different materials by dividing the net outgoing (reflected) radiation by the net incoming radiation, all in the short-wave spectrum. Here, albedo values from the literature are used to characterize the different materials. In Equation 2.5, ζ_{short} is defined as the absorptivity of short-wave radiation of a surface, which is the fraction of radiant energy retained by this surface.

2.4.3 Long-wave radiation (L*)

Similar to the short-wave radiation, the net long-wave (infrared) radiation has an incoming and outgoing part, described in Equation 2.6. The absorbed radiation is emitted as infrared radiation. The received infrared radiation by the surface can originate from two sources: atmospheric and terrestrial radiation.

$$L^* = \zeta_{long} L \downarrow - L \uparrow, \tag{2.6}$$

In Equation 2.6 $L \downarrow$ is the absorbed incoming long-wave radiation and $L \uparrow$ is the outgoing long-wave radiation. These terms are related through ζ_{long}, the absorptivity of long-wave radiation, which is a property of the material of the surface of interest.

The outgoing infrared radiation is described via the Stefan Boltzmann formula stating that the total energy emitted (by a unit surface per unit time) is proportional to the temperature of a black body to the power four. With the black body being an object that absorbs all incoming radiation. When only a part of the incident energy is absorbed, one can use Stefan's Law for grey bodies (Equation 2.7). This introduces the emissivity ϵ, which is the ability of a surface to emit infrared radiation. In LASER/F model the assumption is made that the complement of the emissivity defines the reflectivity Kastendeuch and Najjar [7].

$$L\uparrow = \sigma \epsilon_s T_s^4, \tag{2.7}$$

In Equation 2.7, σ is the Stefan-Boltzmann constant ($5.670\,400 \times 10^{-8}\,\mathrm{Wm^{-2}K^{-4}}$) and T_s the surface temperature in K. The down welling long-wave radiation can be determined by using Equation 2.8.

$$L\downarrow = L\downarrow_{sky} + L\downarrow_{env}, \tag{2.8}$$

Where $L\downarrow_{sky}$ is the reflected/emitted long-wave radiation from the sky and $L\downarrow_{env}$ the reflected radiation from the environment. The amount of radiation received from the sky is influenced by the sky view factor. This quantity is equal to 1 for an entirely visible sky and 0 if the sky is totally blocked from a certain position.

2.4.4 Heat fluxes

The electromagnetic terms in the surface energy equation are balanced by the non-radiative fluxes. In LASER/F model these fluxes are calculated by using methods which are not further investigated in here. For a full overview, the reader is referred to the following references.

- *Sensible heat flux* - determined by using methodology described in Al-Sanea [33]. The thermal performance of roofs, which is discussed in this paper, is extended to other materials in LASER/F model.
- *Latent heat flux* - the Penman-Monteith method as described in Howell and Evett [34].
- *Ground heat flux* - the Fourier's law of heat conduction is used to describe this Incropera et al. [35].

2.4.5 Solving surface temperature

With all parts of Equation 2.1 now discussed, the equation can be rewritten in a form that is solely dependent on the surface temperature (Equation 2.9).

$$K^* + L^*(T_s) + Q_H(T_s) + Q_E(T_s) + Q_G(T_s) = 0 \tag{2.9}$$

The way to obtain surface temperature in LASER/F, is described in Section 4.2. In short, for every unique combination of place and time, the surface energy balance has to be recalculated. This can be done iteratively until it is converged below a user defined threshold.

Chapter 3

Site description

From Chapter 2 it is deduced that the geographic location, geometry and surface conditions of the urban canyon have an influence on the climate experienced within the canyon. This chapter provides the necessary site description of the canyon in Strasbourg which was used for the research. Section 3.1 describes the geographic and urban context which merits consideration while Section 3.2 describes the relevant features of the canyon itself.

3.1 Geographic context

The urban canyon chosen for this research project is 'Rue de l'Argonne', in Strasbourg, France. The canyon is used as the study site primarily because it has previously been used by LSIIT for an extensive climatological field campaign in 2002 [36]. At the time of the field campaign there is access given to the building of the Department of Geography from which it was possible to take thermal images of the canyon floor and also to set-up the field measurement station overnight.

3.1.1 Urban context

The canyon is located in the city center of Strasbourg, (48.33° N, 7.38° E), a city in the Alsace region with a population of nearly 280,000 inhabitants (see Figure 3.1). The average height in adjacent urban blocks around the canyon are between 5 and 7 storeys. The canyon represents a typical city center street and the buildings are used for mixed residential-commercial use. The canyon is located half-way between two canals that are about 700 m east and west respectively. While the surrounding urban area is densely built, nearby about 200 m south-west there is a botanical garden, which may influence the climatic conditions in the neighborhood.

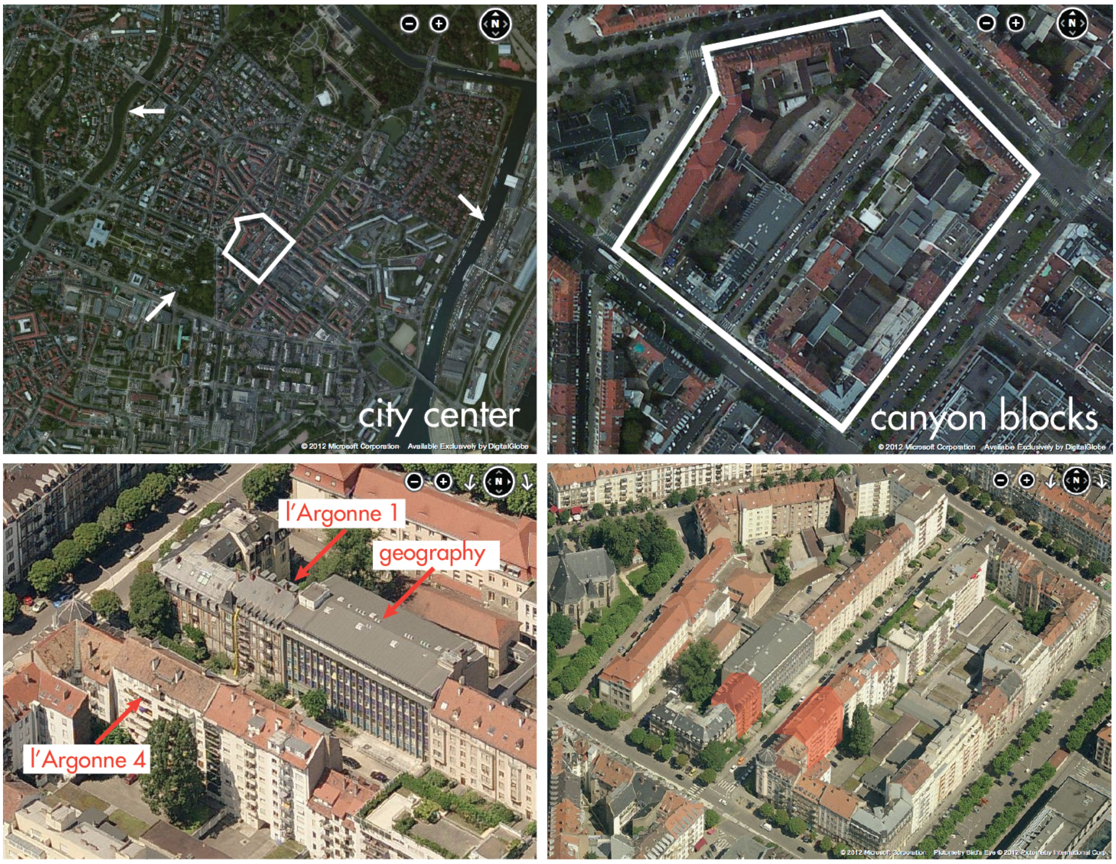

FIGURE 3.1: The urban canyon (Rue de l'Argonne) from a birds eye and isometric view

3.1.2 Local summer climate

Late August and early September is a seasonal transition period between summer and autumn. The average daily high temperature is between 21 and 24 °C and lows between 10 and 13 °C, which is the annual temperature peak. The average precipitation is about 58-80 mm in this season. This coincides with the annual precipitation peak, but with only 10 to 12 days of precipitation. Relative humidity at this time was measured at around 20 %. During field measurements, the sunrise was around 07:10 and sunset at 19:40 and there was no precipitation. Wind in the area around the canyon was blowing from differing directions depending on the day at an average of $1.4\,\mathrm{m\,s^{-1}}$.

3.2 Rue de l'Argonne

Rue de l'Argonne was an ideal study site not only because of its consistency of the street wall (height, adjacency and setback), but also because it was located within the city center area with a similar urban fabric as described in the previous section.

3.2.1 Geometry

This urban canyon is roughly 170 m long, 20 m wide (from facade to facade), and 15-20 m high, depending on the individual buildings. Therefore the aspect ratio (H/W) is between 0.75 and 1. The street can be considered as a regular symmetric urban canyon. It is flanked by buildings as both ends of the canyon enter a T-intersection (actually, a broken grid form). It is oriented at about 35° from the north, which means the east-facing side of the street is illuminated in the morning and the west-facing side in the afternoon. Due to its orientation, the southern end of the canyon is illuminated for longer than the north end throughout the day (morning shadows in the northern end), although the difference was not measured directly. The SVF has also not been measured directly, but sky view is not significantly obstructed (especially since the aspect ratio is close to 1).

3.2.2 Surface conditions and street objects

The building materials that are used on the surfaces of the canyon are typical for most urban areas. Facades typically feature stone bricks and concrete with glass windows. There are also buildings with ceramic tiles on all or part of the facades. Some buildings exhibit steel framed balconies, or balconies that share the same surface material as the wall (e.g. respectively 1 and 4 Rue de l'Argonne). The dark traffic road is probably paved with asphalt concrete, although this was not verified.

The buildings on both sides are set back about 5 m from the edge of the traffic road. Within this setback there is a front garden for nearly every building along the street, consisting of a few trees (covering some facades), bushes and shrubs no more than 2.5 m in height. Very little grass is present along these vegetation strips. A single row of on-street parking flanks the traffic roads and is consistently occupied with vehicles.

3.2.3 Buildings of interest

The level of complexity in the 3D geometry model provided for this project is inhomogenous along the canyon walls. Thus, it was decided to run the experiments by varying just a slice of the canyon which has the most complex geometry (including balconies, roofs, windows and window frames) as the starting point of model generalization. Based on this criteria, the two buildings chosen for the experiment and validation are 1 and 4 Rue de l'Argonne. These two buildings are located across from each other in the canyon. They are not identical in height or material properties, nor are they perfectly aligned opposite each other, but they are easy to measure on site and also have the least obstruction by vegetation. It was also ideal to choose opposing buildings in order correctly measure the reflectance from the buildings that have the most influence on each other.

Additionally, it was interesting to take thermal measurements of the street as well as the facade from a higher angle. This was possible for 4 Rue de l'Argonne, since access was granted during field measurements to the building across the street (Department of Geography). The second floor of this building was an ideal position to measure heat from the top of balconies, whereas images taken at the ground could not capture the balcony tops. The following paragraphs describe the two selected buildings of interest.

Building of interest: 1 Rue de l'Argonne

This building is situated to the west of the department of Geography, on the north side of the canyon (see Figure 3.2). The material on the podium of the facade is primarily made of pre-cast concrete, whereas the remaining floors have red stone brick and stone fenestration the windows. It has a considerable amount of glazing (around 50 %, but some windows have closed screens (so no reflection can be detected in a thermal image). However, note that the percentage of glazing on the facade was not measured. Part of the complex facade in the model are the three steel framed balconies.

GPS location building: 48.583994° N, 7.771494° E

Building of interest: 4 Rue de l Argonne

This building is situated on the south side of the canyon, opposing 1 Rue de l'Argonne and the Department of Geography building. It was interesting to measure this building because the surface materials are different than 1 Rue de l'Argonne and the facade shape is more complex (more extruded and recessed parts). The facade is primarily treated with ceramic tiling at the podium and first floor level. The remaining facade surfaces are concrete and painted stone. It also has a lower share of glazing than 1 Rue de l'Argonne.

GPS location building: 48.583869° N, 7.771839° E

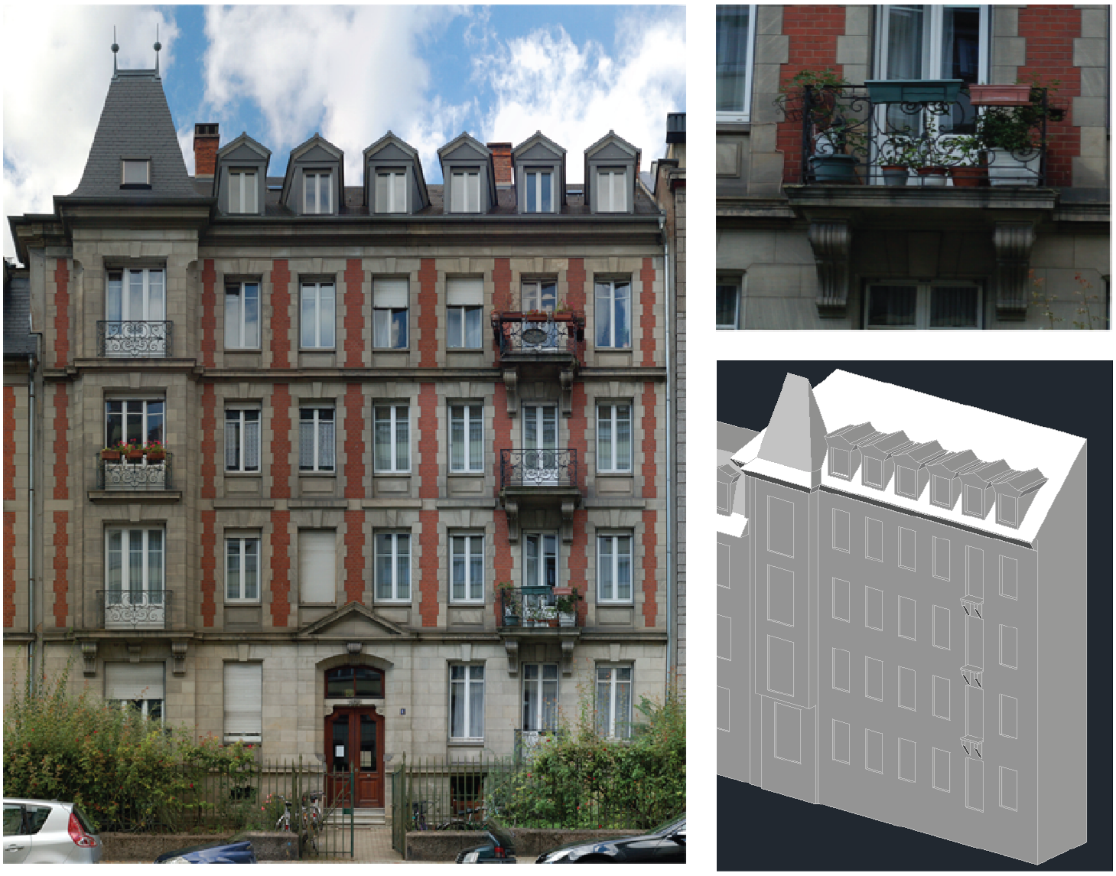

Figure 3.2: Rue de l'Argonne 1 facade features and model shows a great deal of complex shapes and heterogeneous surface materials

Figure 3.3: Rue de l'Argonne 4 facade features and model show the extreme shape of the balconies and complex result in the 3D model

Chapter 4

Radiative transfer model LASER/F

The LASER/F model was developed by Kastendeuch and Najjar [7] to simulate the micro-climate of urban areas. The model solves the energy balance at the soil-atmosphere interface using energetic terms as radiation, soil heat flux, sensible and latent heat flux. The result of the simulation model are all the components of the energy balance equation for every mesh [7].

In this chapter the input to LASER/F (Section 4.1), the modelled processes (Section 4.2) and the output from LASER/F (Section 4.3) are described.

4.1 Input of the LASER/F model

The model uses geometry and weather conditions as input. How the geometry is converted into the required format, .geo, is described in Subsection 5.1.2. The .geo file also contains references to object, face and material types for every polygon in the dataset. The actual information on these types are stored in separate material and surface files.

As previously stated the .geo input file contains for each face the material type. This material type is parametrized within LASER/F by means of two different tables: material properties and material structure. The material properties table contains for each type the direct and diffuse reflectivity, emissivity, conductivity, specific heat, density and refraction index. On the other hand there is a table material structure which builds up a complete face from different layers of material in which for each layer a thickness is defined. For instance a wall has first a layer of plaster after which it has several layers of concrete to be able to parametrize the walls as good as possible.

The weather conditions are provided in a so called forcing file. The forcing file contains the measurement data which was acquired as described in Section 5.4. The data needs a constant time interval. Since the irradiance measurements were taken every two minutes and the air measurements every fifteen minutes, the time interval of the data in the forcing file is set to fifteen minutes.

4.2 Modelled processes

LASER/F is created to simulate the terms of the energy balance, as described in Section 2.4, at a high spatial resolution and in a full 3D environment Kastendeuch and Najjar [7]. To better understand the processes that are modeled by LASER/F it is important to look at what the hierarchical geometry structure looks like. This hierarchy is shown in Figure 4.1. The simulations are done on a scene which consists of objects. Objects can be buildings, terrain or street furniture for example. These objects are built from different faces with different material properties. In LASER/F these faces are further fragmented into a triangular mesh for which at each center point of the mesh the energy balance equation is solved as described in Equation 2.1 in Section 2.4 (Figure 4.2).

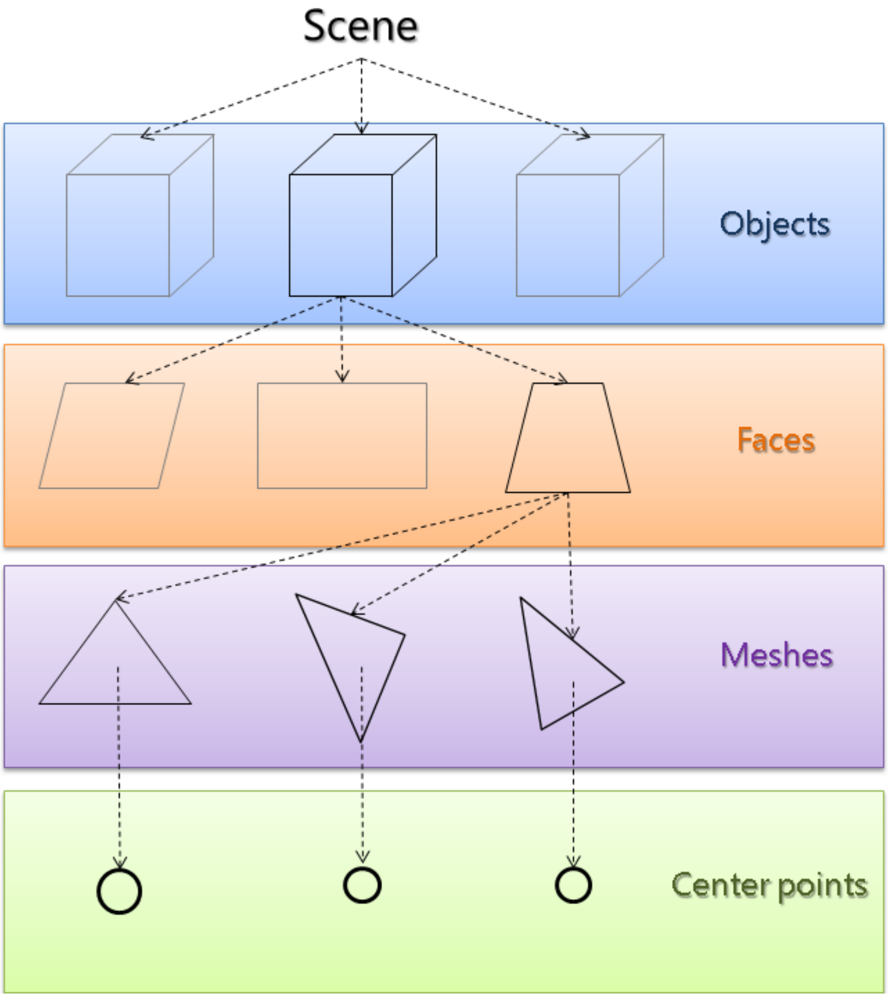

FIGURE 4.1: Hierarchical geometry structure of LASER/F

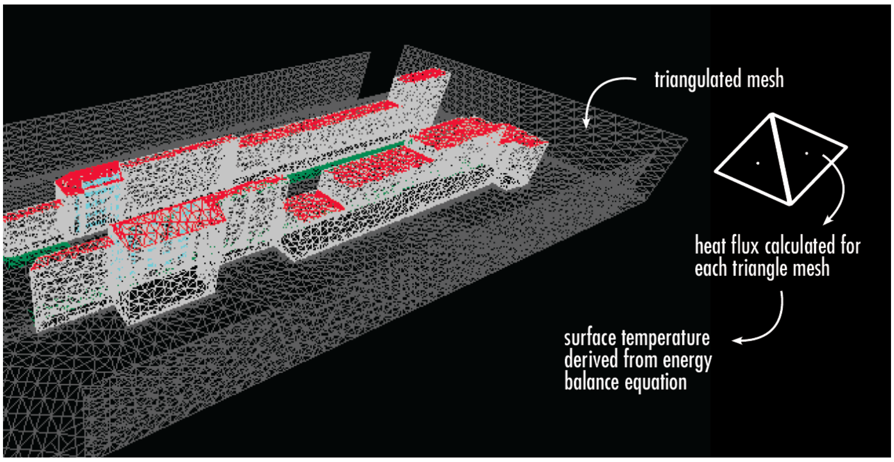

Figure 4.2: Basic concept of the LASER/F calculation process

The maximum size of the triangles is set to be $5\,\mathrm{m}^2$, which is a balance between computation time and level of detail. The model uses a hemisphere to simulate the sky, which needs to be fragmented as well. For the simulation the sky is divided into 256 faces. For each of those faces, it needs to be determined to which geometry fragments these have free line of sight. For this, a SVF and a form factor (see Kastendeuch and Najjar [7]) are introduced, which both evaluate the visibility of all the sky meshes for each geometry mesh. The SVF uses the form factor, which is different for each unique combination of sky mesh and terrestrial mesh, in combination with a visibility factor v. This visibility factor is 0 when the terrestrial mesh does not see the sky at all and 1 when it is completely visible, so in case of testing geometry this value will be somewhere between 0 and 1. The use of these factors will discussed hereafter.

The simulation has to be run at a time interval which can be no larger than the fifteen minutes specified in the forcing file (which specifies incoming meteorological conditions at the top of the canyon). In a conversation with P.P Kastendeuch (September 2012) it is discussed that having a smaller time step than the default would not result in higher accuracy, thus 900 seconds is used here as well. The simulation requires a stabilization period (see Subsection 5.5.1) of one day to get the micro-climate into a state of equilibrium due to the fact that the soil and building interiors need to be heated as well. This requirement doubles the simulation time when the results over one day are desired.

As with every model, LASER/F is an approximation of the natural processes which are known as surface energy exchanges. In Section 2.4 it is briefly discussed how the different radiation fluxes are modeled during the simulation. Currently, the ground, latent and sensible heat fluxes are based on parametrization as described in other papers. These approximations can introduce errors in the eventual calculation of radiant exitance and surface temperatures. As a part of the surface energy balance, the net radiation balance (Rn in Equation 4.1) is the term that is simulated in LASER/F using parametrizations in combination with measured quantities as forced input to compute radiant terms. This net radiation balance can be divided into a solar and a infrared balance.

The solar - or short-wave - radiation balance relates to the equations in Subsection 2.4.2. From this equation the direct solar radiation, atmospheric diffuse radiation and the reflected terrestrial radiation are modeled in LASER/F. The first (S in Equation 2.4) is calculated using a forced (via measurements) direct solar radiation, corrected for the incidence angle on the normal of the surface. This computation is based on ray-tracing, which means that the sun shoots parallel lines of sunlight into the scene. The location of the sun is known, so if there is a surface in between the receiving triangle and the origin of the sun ray, a transmission value t is applied to this ray: 0 for completely opaque surfaces, 1 for no obstacle on the trajectory and a value between 0 and 1 for transparent materials. The second and third (both stated as D in Equation 2.4) are also based on measured values by the meteorological station as described in Section 5.4. Atmospheric diffuse radiation uses the aforementioned meshed hemisphere in combination with a form factor (between the sky mesh and the terrestrial mesh) and again a transmission value t. The amount of reflected radiative solar energy is calculated by summing the reflection contributions of all the triangles visible from the mesh where the surface energy balance is calculated for at that moment.

The infrared - or long-wave - radiation balance relates to the equations in Subsection 2.4.3. LASER/F makes a division between the origins of the radiation. On one hand the atmosphere and on the other infrared radiation from terrestrial components. The atmospheric infrared radiation is only dependent on the line of sight to the sky and therefore the SVF comes into play using the forced external radiation data. The radiation from terrestrial components is calculated with the use of Equation 2.7, with the assumption made in LASER/F that $1 - \epsilon$ equals the reflectivity. This term is then used in combination with the emitted infrared radiation by a terrestrial mesh to calculate the total incoming radiation from all the visible meshes in the scene to the triangle where the surface energy balance is solved for at that moment. LASER/F takes into account two reflections from emitted long-wave radiation from other buildings. Longer reflection paths are assumed to have a negligible effect on the surface temperatures of the buildings in the urban canyon. For this reason they are not modeled.

Next to the radiant exitance (IR), the surface temperatures are given as an output of LASER/F. After simulating or forcing all parameters as input for the energy balance, the next step is to start solving for the surface temperatures for every center point of every mesh in the triangulated scene. These are computed in two steps.

1. All the flux terms are computed. They serve as input for the energy balance equation, which is stated in Kastendeuch and Najjar [7] as:

$$Q^\tau + Rn^\tau + Le^\tau + S^\tau = \frac{\rho \cdot c \cdot \Delta h}{2\Delta\tau}(T_s^\tau - T_s^{\tau-1}), \tag{4.1}$$

where Q equals the ground heat flux Q_G, Le equals the latent heat flux Q_E and S the sensible heat flux Q_H. Rn is the net radiation with short-wave K_{tot} and long-wave L_{tot} included. The right hand side represents the heat storage in a mesh for a time step τ.

With all the computed flux terms, the surface temperatures T_s are calculated. Having these temperatures, the fluxes change and they will have to be redetermined. This will continue until the two successive iterations give a temperature difference of $< 0.01\,\mathrm{K}$.

2. Following this, the radiant exitance can be calculated using the surface temperatures iteratively until two successive iterations give a radiant exitance difference of $< 1\,\mathrm{W\,m^{-2}}$. With this, the final surface temperatures can be calculated.

The internal heat storage and inertia of heating the building is evaluated based on building volume. This volume is calculated from the footprint of the roofs and the associated height. It thus does not take into account details on the walls of the buildings.

4.3 Output of the LASER/F model

The simulation data is stored in binary '.reb' as wel as American Standard Code for Information Interchange (ASCII) text file. After the simulation the .reb file can be imported into LASER/F. The user will be presented with a 3D representation and options to choose which parameters should be projected onto the model. The possible settings are shown in Figure 4.3.

LASER/F stores all attributes for every triangle in the mesh. These values can be retrieved using the Graphical User Interface (GUI) for one point at a time. The comparison will require many if not all points in the model, as such a text output functionality in the LASER/F program was requested and implemented. An example can be found in Appendix D. The output consists of one line for every triangle containing the object id, triangle vertex coordinates, center point coordinates, surface temperature as well as emittance and reflectance.

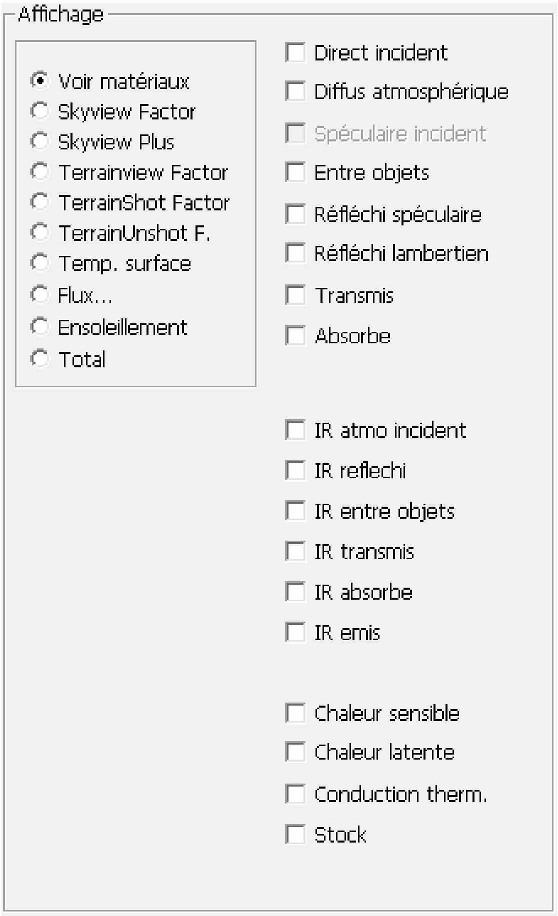

Affichage

● Voir matériaux
○ Skyview Factor
○ Skyview Plus
○ Terrainview Factor
○ TerrainShot Factor
○ TerrainUnshot F.
○ Temp. surface
○ Flux...
○ Ensoleillement
○ Total

☐ Direct incident
☐ Diffus atmosphérique
☐ Spéculaire incident
☐ Entre objets
☐ Réfléchi spéculaire
☐ Réfléchi lambertien
☐ Transmis
☐ Absorbe

☐ IR atmo incident
☐ IR reflechi
☐ IR entre objets
☐ IR transmis
☐ IR absorbe
☐ IR emis

☐ Chaleur sensible
☐ Chaleur latente
☐ Conduction therm.
☐ Stock

Figure 4.3: Visualisation settings in LASER/F

Chapter 5

LASER/F simulation methodology

With the research goal and theoretical information clear, it is time to discuss the LASER/F simulation methodology. In this chapter, an overview is given of the different methods and design choices made with respect to the acquisition and processing of data. Appendix E part A provides an overview of the work flow of the processes described in this chapter and how it relates to the others.

To this end in Section 5.1, the 3D geometry input to LASER/F is discussed. In Section 5.2, the different simulation scenarios that are to be simulated by LASER/F are discussed. The radiative transfer model also needs (meteorological) forcing conditions for which the measurement set-up is elaborated on in Section 5.4. Finally some results that are needed for the baseline determination are discussed in Section 5.5.

5.1 3D Geometry

In this section the geometric input of the LASER/F model will be discussed as well as the conversion to the LASER/F geo file format.

5.1.1 AutoCAD model

For both models which are simulating microclimate aspects on an urban canyon scale (LASER/F and the CFD model), a detailed AutoCAD model of the 'Rue de l'Argonne' in Strasbourg is being used as a base. This geometric 3D model (see Figure 5.1) was acquired by the Faculty of Architecture of Strasbourg in July 2001 using photogrammetry. The acquisition of the photos was done only from within the canyon itself, meaning that there is no detailed 3D information on the facades at the back of buildings that are inside the canyon. Since the validation of the simulation will be done on the facades of two specific buildings at the inside of the canyon, one might argue that there is also no need for complex geometry at the back of the buildings however this is not entirely the case. As discussed in Chapter 4 the LASER/F model takes into account the heat storage of buildings as a function of their volume. A larger volume of a building causes an increased thermal inertia which makes the air inside the building warm up more slowly. The inside temperature of the building has a direct influence on the surface temperature of all the faces which make up the building.

Throughout the canyon also the complexity of the buildings is not homogeneous. Since it is not possible to simulate the full canyon in LASER/F with the highest geometry complexity only two buildings which are opposing each other (and have the relatively highest complexity) are used for the simulations (which is elaborated further in Section 5.2).

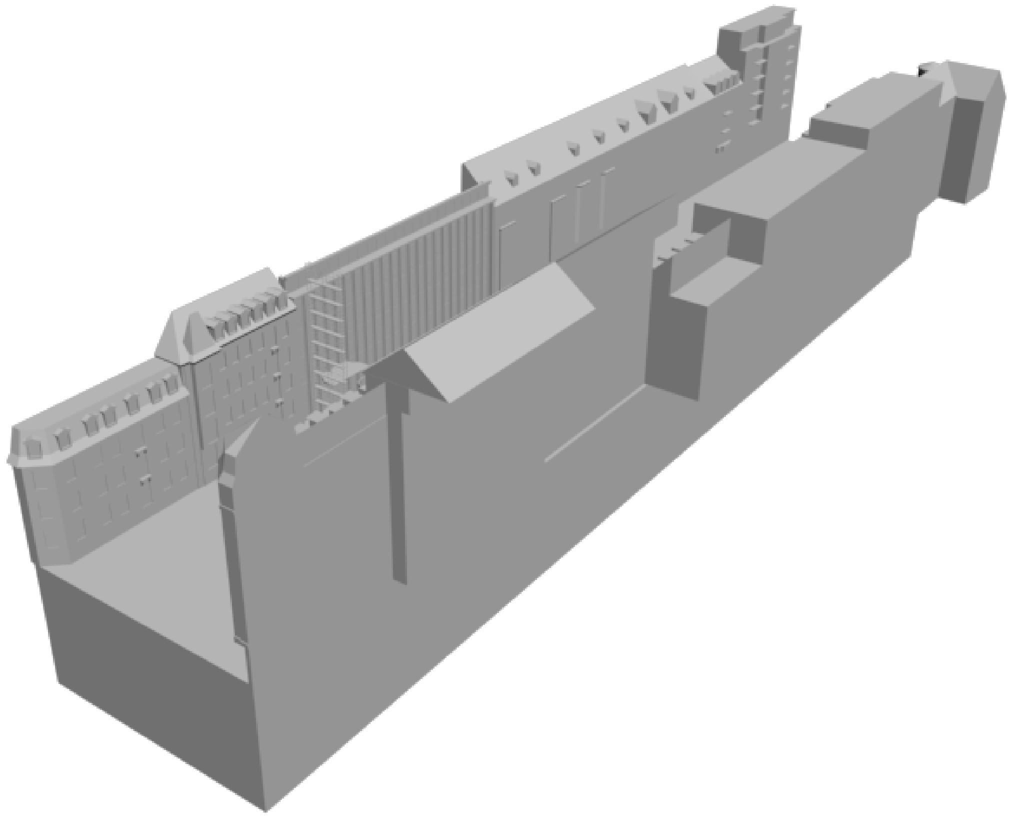

Figure 5.1: AutoCAD model of Rue de l'Argonne

5.1.2 Conversion to LASER/F file format

The base for the geometry of the simulations is provided in the AutoCAD '.dwg' format. The input to the LASER/F program is however in its own '.geo' file format. To be able to convert the AutoCAD model into the LASER/F file format the .dwg file is first converted to an ASCII Scene Export (ASE) file using Autodesk 3DS Max. This is done separately for each building/object. With the same program the different faces are given different colours (materials). A Python program is developed to read the ASE files (get the vertexes, faces and materials from the file), convert this data to the .geo file format syntax and to write a Virtual Reality Modeling Language (VRML) file for visualisation of the scene. Furthermore .tri and .xyz files are written with faces and vertices for reference when a certain error would occur. The complete conversion chain can be seen in Figure 5.2. An example of an ASE file can be found in Appendix C.

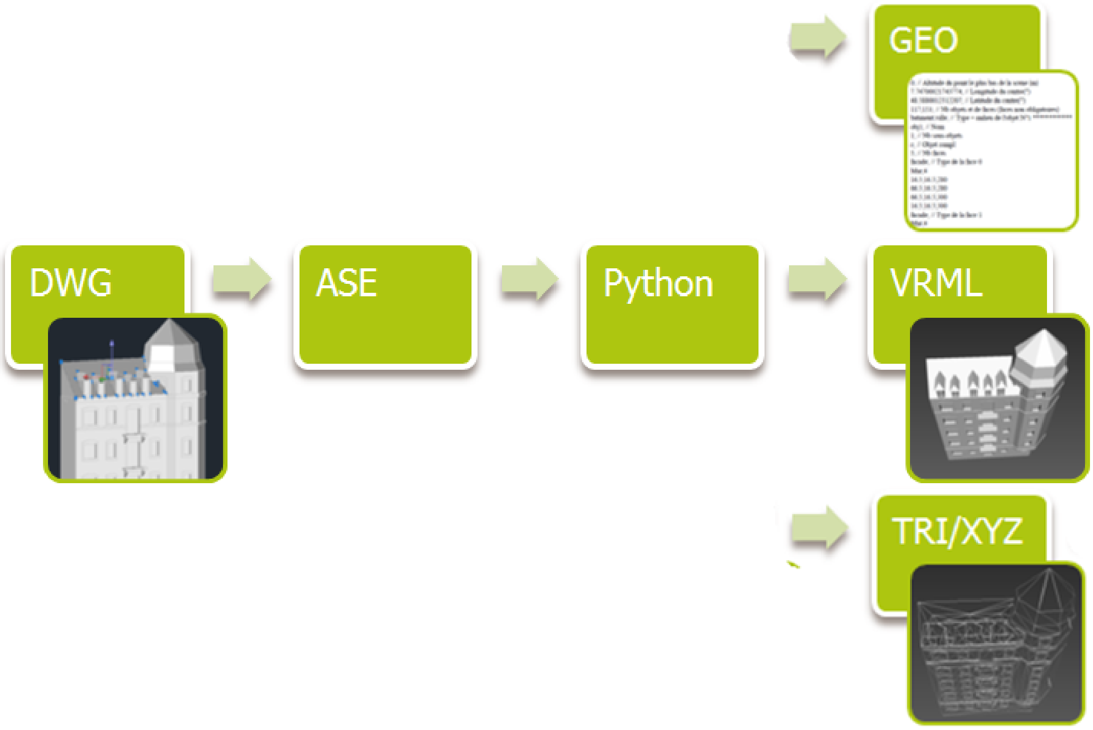

Figure 5.2: Conversion chain from AutoCAD to LASER/F file format

5.1.3 Reference system

Since the reference system of the input geometry into LASER/F is of high importance for the calculations done in the model, this is described here. The input geometry should have its y-axis pointing from south to north, the x-axis from west to east and the z-axis perpendicular to that with the zero altitude at mean sea level. The center point of the canyon in longitude and latitude should be given as input to the model. [37] This is for the purpose of simulating the sun's position and the atmospheric conditions correctly. It is however unknown by the developer of LASER/F in which reference system the latitude longitude needs to be. The x and y-axis are confirmed to be in the right orientation however the z-axis is not. Compared to the mean sea level, which is measured by the tidal gauge in Marseille (IGN NGF 69), the z-coordinates are 140 meters off. Therefore 140 m is added in the .geo file to compensate for that.

5.2 Simulation scenarios

One of the research questions for this project is to determine the influence of detailed geometry in the 3D model on the accuracy of the LASER/F model. A few trial runs have proven that a simulation in the canyon with as much geometric detail as in the AutoCAD model is not feasible as the estimated simulation time is going to be in the order of weeks and the program is not stable enough to be able to guarantee results. Therefore generalizations of the canyon are needed. There are two options for generalizations. It is either possible to generalize according to the LoD structure defined in the CityGML standard or to define different geometric features, which are added to the buildings.

5.2.1 Generalization options

Multiple options need to be made to determine the LoD needed for this research project. Two options are explained along with their strengths and weaknesses.

LoDs according to CityGML

CityGML is an information model for the representation, storage and exchange of 3D models of cities. The data format of the canyon representation is not of importance as it is only used for input in the LASER/F model. However, the multi-scale structure in CityGML could be useful for the purpose of this project. In CityGML there are five LoDs defined [38]:

- *LoD 0* - regional, landscape
- *LoD 1* - city, region
- *LoD 2* - city districts, projects
- *LoD 3* - architectural models (outside), landmarks
- *LoD 4* - architectural models (interior)

In terms of its geometry the definitions can be better understood by looking at Figure 5.3. Whereas LoD 0 is only a digital terrain model, LoD 1 to 4 actually contain building information. LoD 1 is only extruded blocks, whereas LoD 2 and 3 add simple roofs and other geometric features respectively. LoD 4 yields a full 3D model both from the outside and inside, the latter of which is not of importance for the purpose of this project.

As stated before the AutoCAD model does not have homogeneous complexity throughout the canyon. Simulation scenarios with LoDs as defined in CityGML would thus yield different kinds of generalization. Besides, LoD 1 and LoD 2 would not result in a proper

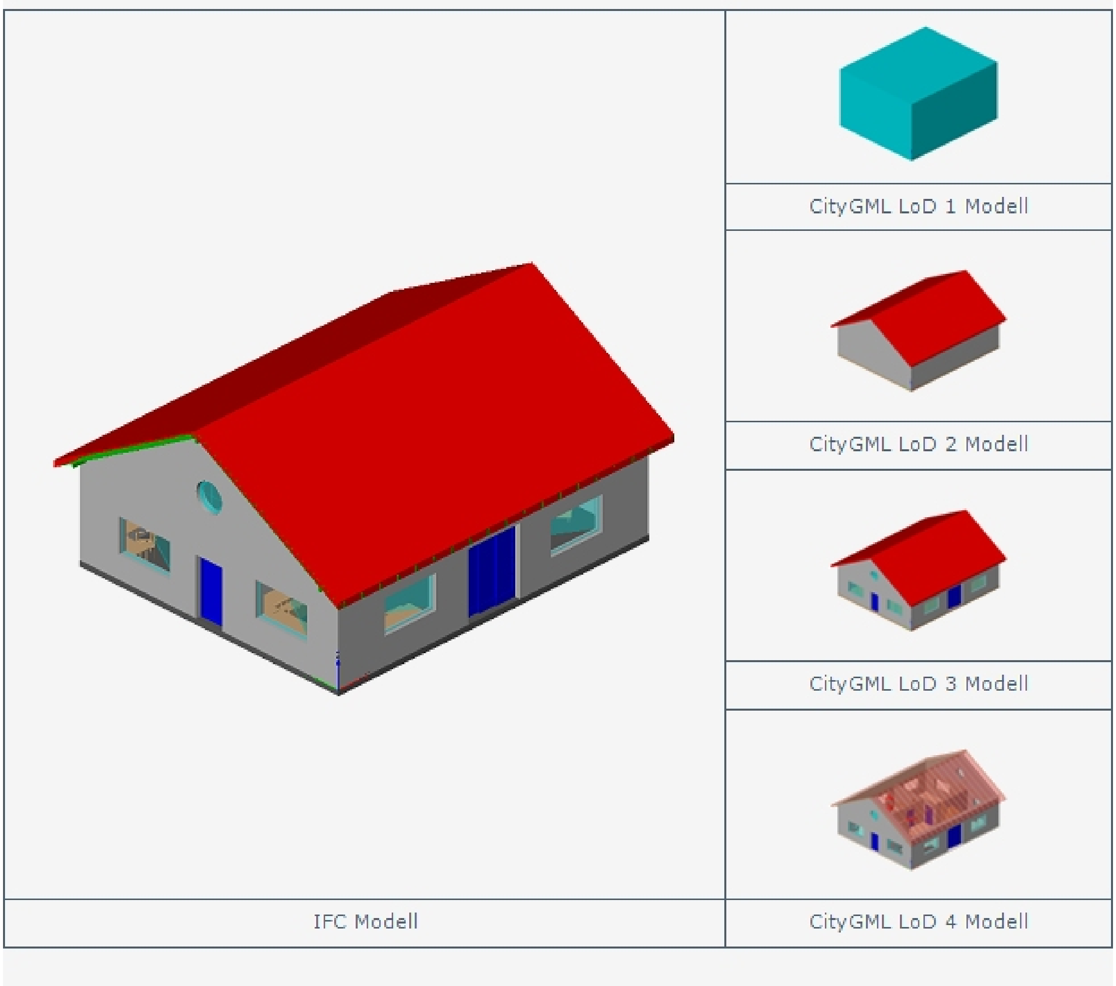

FIGURE 5.3: LoDs as defined in CityGML [4]

answer to the research question as they are only extruded blocks with simple roofs and by using these LoDs it would not be possible to test the influence of different kinds of complexity. On the other hand simulations on an urban canyon with LoD 3 is found computationally too expensive. Instead it is more convenient to split LoD 3, to be able to see the influence of distinct geometric features, which is described next.

Generalizations by adding geometric features

Since radiation and heat simulations are computationally very expensive, it is a good idea to look at the influence of distinct geometric features such as windows, balconies and roofs. To limit the computation time further these geometric features can, for example, only be added to the buildings that are to be validated. In this way the level of complexity is however inhomogeneous throughout the canyon, and thus the LoDs defined in CityGML do not hold.

Generalization plan

Based on the previous comparison it is decided to perform simulations on a simple base case, and only add certain geometric features to the buildings on which the validation is done.

The possible improvement in accuracy of the LASER/F simulation is to be determined from the comparison between the simulations with the added geometric features and the simple base case. Therefore it is chosen to let the simple base case be the canyon with extruded blocks. The blocks are obtained by extruding the footprints of the buildings in the canyon upto the height where the roof starts. The gabled roofs are assumed to have a negligible effect on the produced shadows. The cases with different geometric features are chosen such that a minimal increase in geometric details is obtained, causing the simulation time to increase with a minimal amount as well. The different simulation cases that are defined are:

- *Base case* - extruded blocks
- *Base case + simple roofs* - extruded blocks with simple roofs
- *Base case + complex roofs* - extruded blocks with the full complexity of the roofs
- *Base case + windows* - the shape of the windows are projected on the extruded blocks
- *Base case + balconies* - the geometry of the balconies is connected to the extruded blocks
- *Complex case* - the most complex geometry
- *Complex case + vertex welding* - the most complex geometry is simplified using vertex welding

It should be stressed once more that all cases, except the base case, only apply to the two buildings that are to be validated (refer to Chapter 3 for the building descriptions).

5.2.2 Base case + simple/complex roofs

To determine the influence of roofs on the simulation two roof cases are considered: a simple and a complex roof case. The most complex roof case contains the roofs as they are present in the AutoCAD model for the two buildings (see Figure 5.4). The simple roof case contains the same roofs but without the dormers and extensions on them (see Figure 5.5)

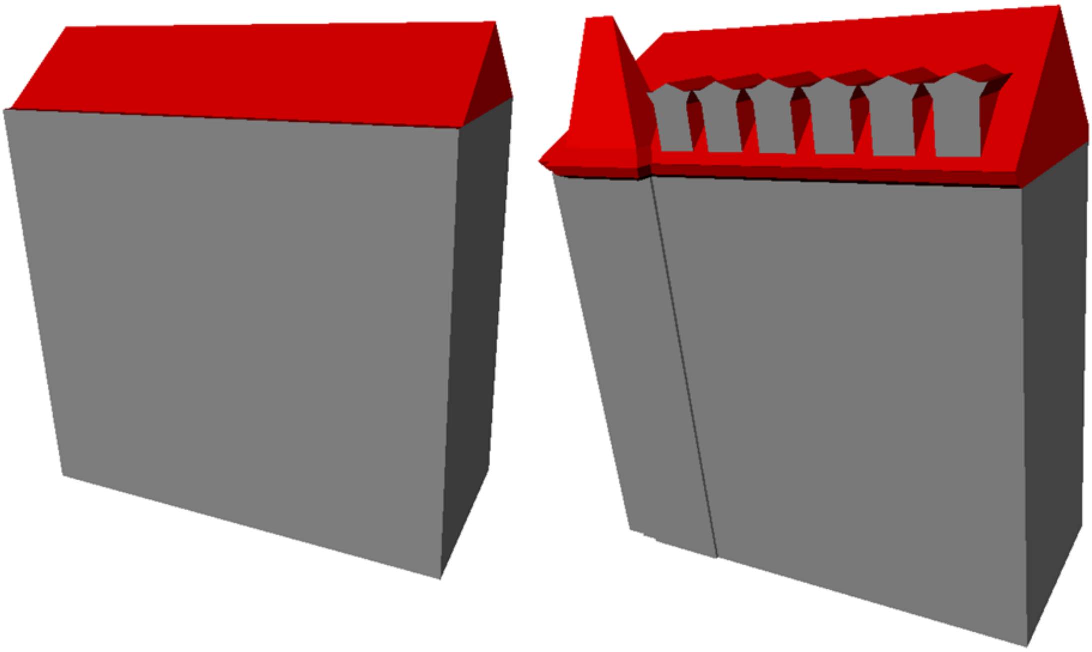

FIGURE 5.4: The base case + complex roof contains the roofs as in the AutoCAD model

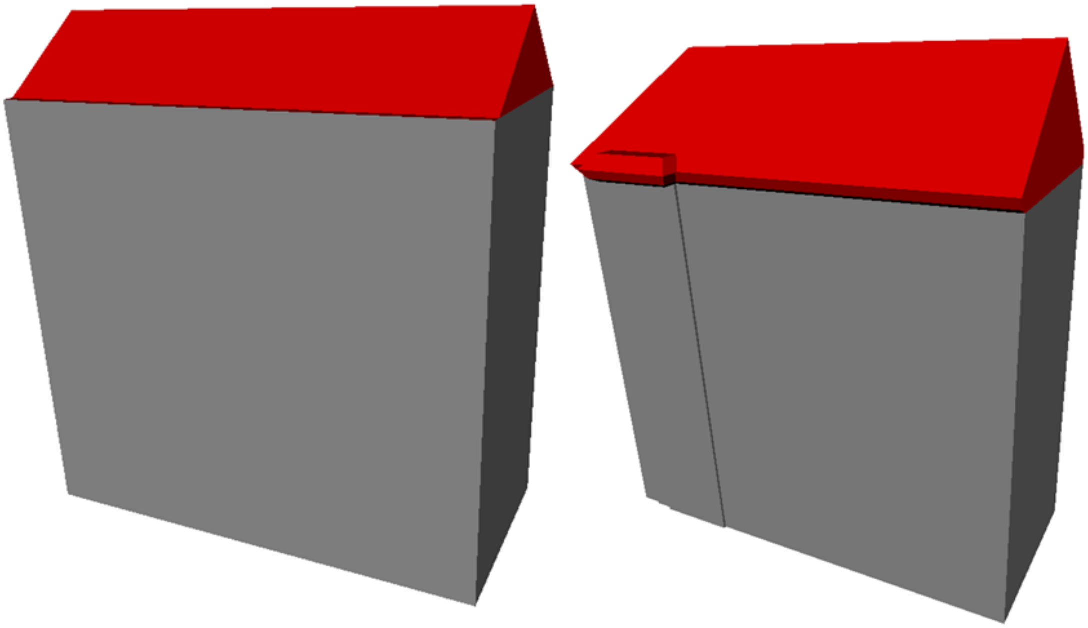

FIGURE 5.5: The base case + simple roof contains roofs without dormers or other extensions to the roofs

5.2.3 Base case + windows

In the window case mainly the material is of importance, since windows have very different material properties from the walls for instance, in terms of emissivity, diffuse and direct reflectivity and refraction index. The geometric details are so subtle that they are not considered here. Instead the windows are projected onto the extruded blocks. The result of this is shown in Figure 5.6.

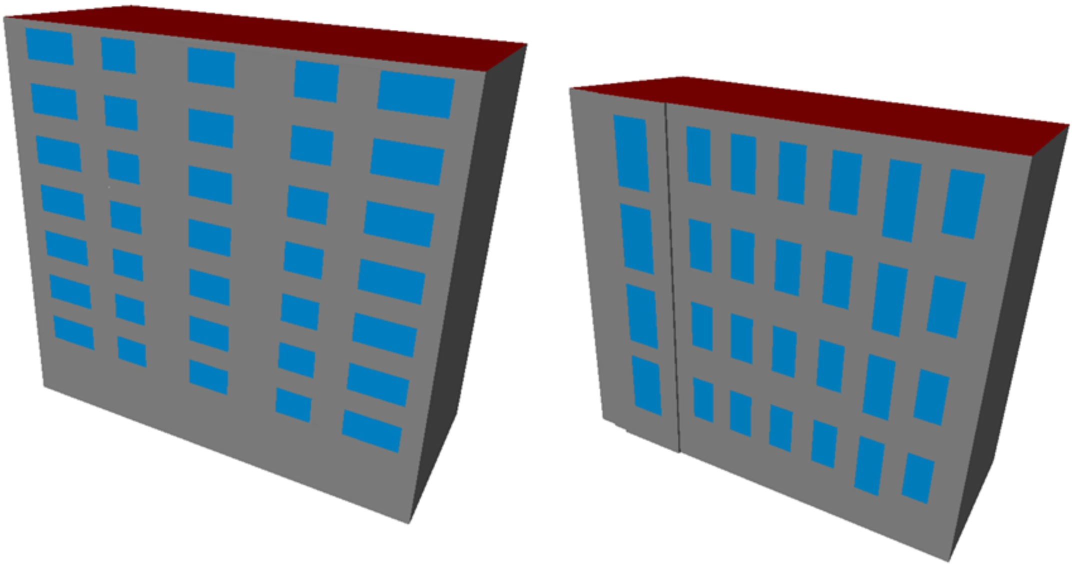

FIGURE 5.6: In the base case + windows the windows are projected on extruded blocks

5.2.4 Base case + balconies

In the balcony case balconies are attached to the extruded blocks. This increases the surface area of the facades of the buildings. However, the increased complexity is also expected to increase the computation time significantly.

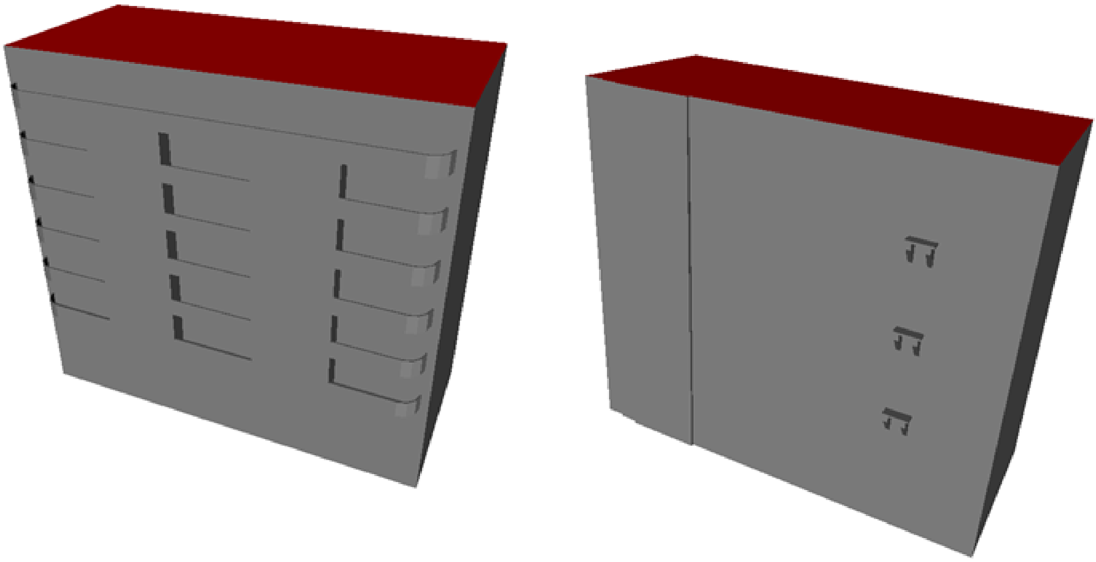

FIGURE 5.7: In the base case + balconies the balconies from the complex geometric model are glued onto the extruded blocks

5.2.5 Complex case

The complex case includes the two buildings as they are present in the AutoCAD model, and are classified to define roofs, walls and windows. The result of this can be seen in Figure 5.8.

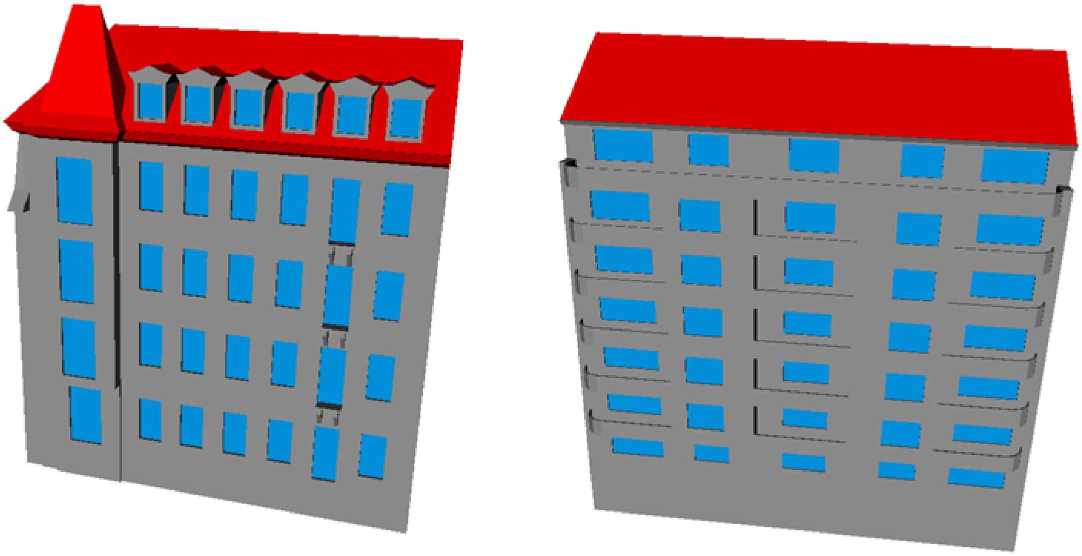

FIGURE 5.8: The complex case has the same geometric representation as in the AutoCAD model

5.2.6 Complex case + vertex welding

This case is a simplified case which ought to be a case which contains all the geometric features. This would basically yield the most complex geometry from the AutoCAD model, but having less triangles which makes it less computationally expensive. The complex geometry is simplified using 'vertex welding'. To obtain the simplified case all the vertices that are closer than 1.0 m are welded together in a random order. The threshold of 1.0 m is chosen such that it minimizes the amount of faces while still represents the building fairly well. The two simplified buildings can be seen in Figure 5.9.

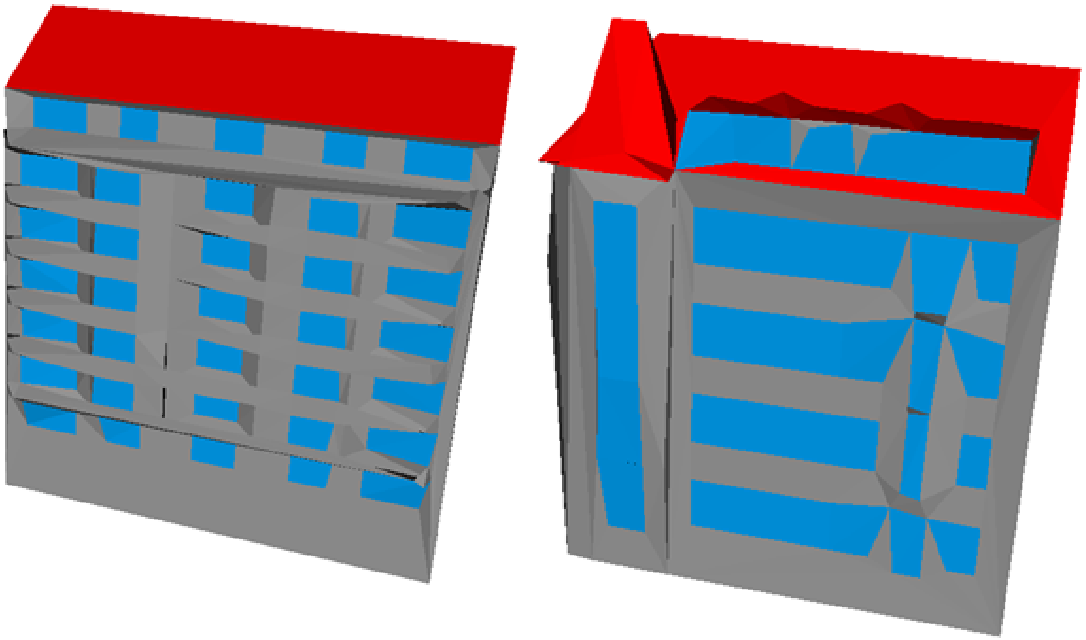

FIGURE 5.9: Simplified buildings are buildings with vertex welding (threshold 1.0 m)

5.3 Additional LASER/F geometry issues

Some geometry issues still remain. In this section the volume of the buildings is discussed as well as the ground layout and the closing of the canyon.

5.3.1 Volume

As stated before the AutoCAD model has been constructed using photogrammetry within the canyon. This means that only accurate geometric details of the facades inside the canyon are present in the model. Therefore the volumes of buildings inside the canyon are not correct. With the use of the layout of the roofs and by looking at imagery from Google Maps, the volumes of the two buildings of interest are reproduced by extending the back of the buildings. This is of importance since it influences the heat capacity of the buildings, causing the surfaces to heat up and cool down differently.

5.3.2 Ground

The ground is modelled as a flat plane which covers the bottom faces of all the buildings present in the canyon. This is done because LASER/F will remove all the touching faces such that the equations will not be solved for the bottom faces of the buildings and the faces that are not visible (for instance faces between buildings). The ground still has volumetric properties (even though all the other type of faces) through the defined material properties in the LASER/F model. Each material type is said to have a number of layers of certain material properties and of a certain thickness. This way each face has volume, but this is not visualized.

5.3.3 Closing the canyon

Purely modelling the urban canyon on itself in LASER/F might not be sufficient as the absence of surrounding buildings can cause the buildings in the canyon to be receiving less reflected radiation fluxes as well as less shadow. A wall of type 'ground' around the urban canyon with the average height, approximate distance and location of the surrounding buildings can however mitigate the absence of radiative fluxes and shadows due to surrounding buildings (see Figure 5.10). As the 'ground' type already encompasses a certain material thickness, heat storage as a function of volume is accounted for without introducing the computational load of modelling complete buildings. Still, simulation time will significantly increase as the number of triangle elements within the simulation increases due to the newly introduced wall configuration (see also Chapter 5).

As simulation time is a crucial factor within the project, the necessity of closing off the canyon should be tested. The results of this case can be found in Section 5.5.

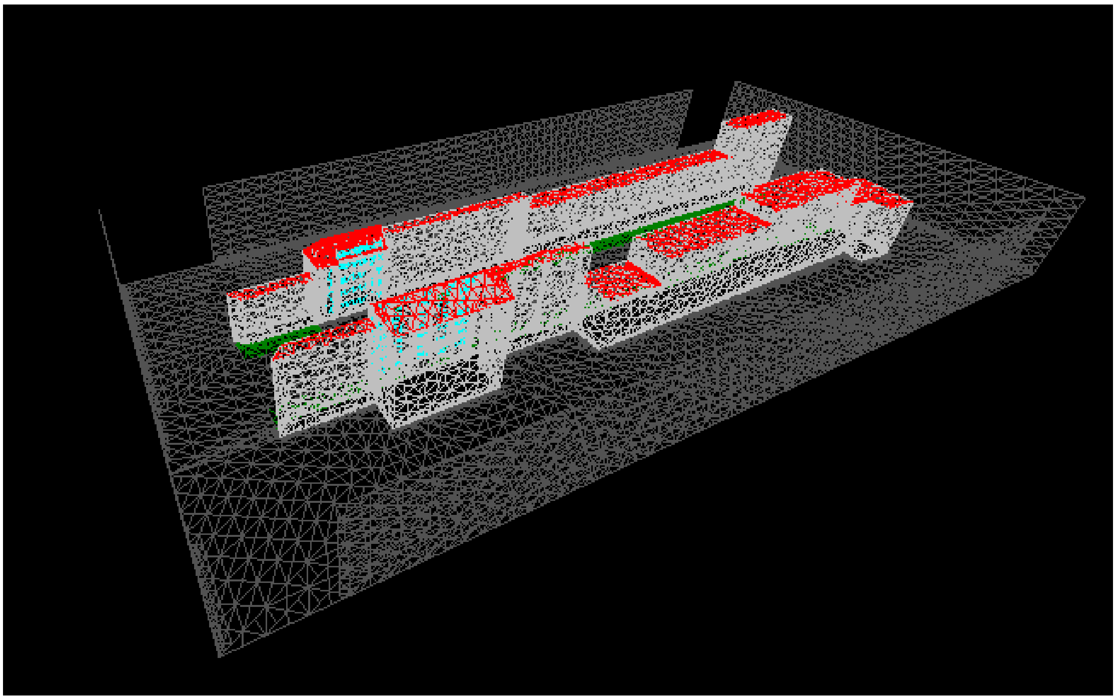

FIGURE 5.10: Overview of the fragmented version of the closed case

5.3.4 Vegetation in the canyon

In LASER/F modelling the vegetation is only implemented to a certain extent at the time of writing. Only ground-cover vegetation (such as grass) can be modelled. To be able to accurately compute the latent and sensible heat flux in the canyon strips of grass at each side of the canyon are modelled. At the buildings where the validation is done the grass is modelled more accurately. Because trees and bushes cannot be modelled, only the grass patches in front of the buildings are modelled. The dimensions of the grass patches are determined using Google Maps (see Figure 5.11). At building 1 there are no grass patches (although there are a few trees and bushes), while at building 4 there are two grass patches. In front of the other buildings there is a continuous strip of grass of 5 m width (see Figure 5.12).

FIGURE 5.11: Size of grass is determined using Google Maps [5]

FIGURE 5.12: Grass layout in the canyon model

5.4 Forcing conditions and measurements

The LASER/F model requires a number of meteorological forcing conditions in the form of a forcing file. This way the same conditions are applied to the model as they were present on field during the measurements. By doing so the environmental conditions for both model will be correct for the comparison. The parameters in the forcing file and the set-up of the measurements of these parameters is elaborated on in this section.

The LASER/F model requires some meteorological forcing conditions in the form of a forcing file. This way the same conditions are applied to the model as they were present during the field campaign. By using consistent environmental condtions, results from the LASER/F, the CFD model, and the thermal measurements can be compared. The parameters in the forcing file and the set-up of the measurements of these parameters is elaborated in this section.

5.4.1 Set-up of meteorological station

With the need for meteorological data now clear, the parameters of interest followed by a overview of the equipment used to measure these unknown quantities will be presented here. To make the set-up complete, the frequency of acquisition is discussed before this subsection concludes with the positioning of the meteorological station.

Meteorological station parameters

Standard meteorological measurements are used to create the input file for LASER/F. Furthermore, they also serve as input for the CFD model. The standard measurement parameters are:

- Air temperature [K]
- Relative humidity [%]
- Wind speed [$\mathrm{m\,s^{-1}}$]
- Wind direction [°], North = 0
- Direct/diffuse/terrestrial irradiance [$\mathrm{W\,m^{-2}}$]

Meteorological station equipment

The following instruments are used to be able to measure the aforementioned parameters.

- *Vaisala HMP45AC probe* - A thermometer to measure the air temperature and a hygrometer to measure relative humidity are combined in this probe.

- *Young 05103 anemometer* - The measurement of wind speed and direction of wind flow is performed by this device.
- *Vaisala PTB110 barometer* - The barometer is used to measure air pressure.
- *Kipp Zonen CMP11 pyranometer* - This pyranometer is used to measure global broadband solar (short-wave and visible light) irradiance. When the direct solar irradiance is subtracted from this broadband measurements, the diffuse irradiance is obtained.
- *Kipp Zonen CGR4 pyrgeometer* - The pyrgeometer measures atmospheric infrared (long-wave) irradiance.
- *Kipp Zonen CHP1 pyrheliometer* - A pyrheliometer is specifically designed to measure direct solar irradiance. It needs a suntracker to be pointed at the sun at all the time. The field of view is limited to 5°.
- *Kipp Zonen SOLYS 2 suntracker* - This suntracker is a robot that is used to make sure the direct solar radiation is received by the pyrheliometer. It has a GPS receiver to automatically receive location data and time to prevent it from clock drift. Additionally, it has a built-in sun sensor for active tracking and a visible check is provided on the device itself.
- *Campbell Sci. CR10 data logger* - The data-logger is used to record data over time of a device that is connected to the logger. The data that is recorded can be averaged over a predefined time window. In the research set-up, the data logger takes measurements every 5 seconds and averages them to one data entry every 15 minutes.

Measurement frequency

The frequency of the measurements is set at delivering one data-entry every 15 minutes, based on averaging all acquisitions taken within that time window. This is sufficient to derive the forcing parameters for the LASER/F model.

Measurements are taken for five days in order to get sufficient data to be aware of the prevailing conditions around the day of measurements with the thermal camera.

Location of the meteorological station

The meteorological station is positioned on top of Institut de Physiologie et de Chimie Biologique (Université de Strasbourg). The direct distance to the canyon of interest is about 650 m, which is shown in Figure 5.13. The large distance may cause irregularities in the forcing parameters determined from the measurements. The meteorological station is positioned on top of the UCL, however the exact is not measured but is about 15m to 20m above the ground.

FIGURE 5.13: Distance between meteorological station and buildings of interest [5]

5.5 Baseline determination

In Section 5.2, different simulation scenarios are presented for which simulations can be run. To run the simulations properly, a good baseline needs to be determined. To this end the necessity of three simulation conditions are investigated: stabilization period, closing the canyon and the presence of vegetation within the canyon.

All these simulation adjustments need to be assessed on whether they yield a significantly different output result and whether the simulation time needed using the adjustment is still within reasonable margins. This can be directly translated into the following criteria:

- Simulated results should not show a difference larger than 1 K.
- Simulations should provide guaranteed results within 1 week.

The first criterion is based on the precision of the FLIR SC655 thermal camera used in the measurement campaign [39]. The second one is based on the timing of the project.

The effect of the simulation adjustments is investigated by comparing the surface temperature of the facades of the buildings to be validated. To calculate the average surface temperature correctly, temperature is first converted to radiant exitance before being averaged. The averaged exitance is then converted back to temperature.

It should be noted that all results presented here is generated with forcing data obtained by LSIIT in 2002 [36], as the forcing data obtained during the most recent 24-hour measurement campaign was not processed completely at the time of simulation.

5.5.1 Stabilization period

Although thermal measurements are taken over a 24-hour period, the LASER/F simulations should run over a longer time period as to model the heat capacity of buildings and soil more properly. Ideally the simulation should run over two days. To check this assertion, a case with constant diurnal forcing conditions over a simulation period of two days is run.

In Figure 5.14 the results of the first and the second day can be seen. The temperature difference between the two days is significant (up to 5 K). It is interesting to see that the surface temperature during the second simulation day is lower than the surface temperature of the first simulation day. This could be explained by the fact that the LASER/F model already assumes a surface temperature of buildings at the start of the simulation, which might be too warm.

As the base case of extruded footprints without closure takes about 2 hours to run, linear increase of simulation run time is still well within reasonable margins for this adjustment.

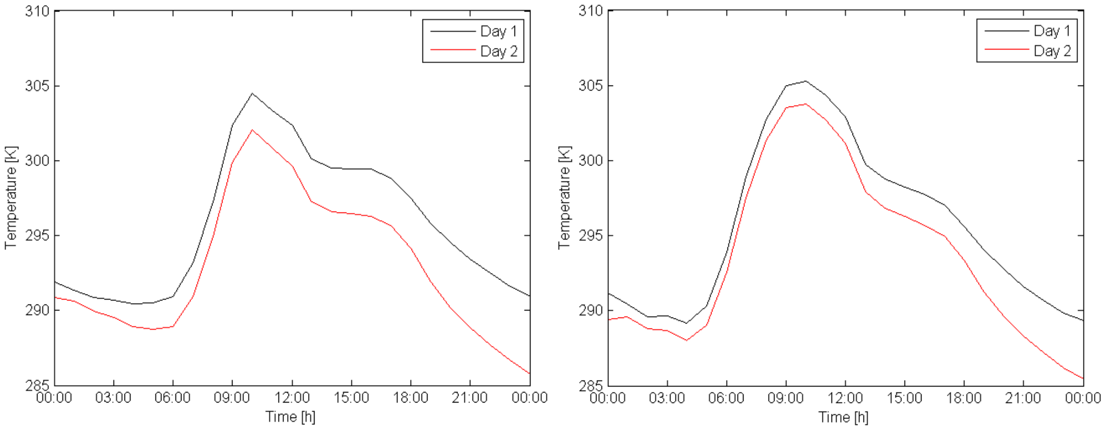

(A) '1 Rue de l'Argonne' (B) '4 Rue de l'Argonne'

FIGURE 5.14: Results of simulation with constant diurnal forcing conditions

5.5.2 Closing the canyon

As is stated in Section 5.2, closing of the canyon is needed to mitigate the loss of radiation and shadow effects due to the absence of surrounding buildings in the model. As can be seen in the results in Figure 5.15, the effect is most notably presented during night time as long-wave radiation will be trapped within the canyon over a longer period of time. The closed case also takes slightly longer to warm up on the first day, which could be attributed to the shadow effects. Temperature difference is significant (up to 5 K).

As expected, the closed case increases simulation time drastically because of the introduction of extra elements into the model due to the fragmentation of the added wall and surrounding ground (see also Figure 5.10). The simulation for the simple base case takes about 2 hours in the open case, while the closed case takes about 8 hours.

Still, considering the significant temperature differences and the criterion of guaranteed results within a week, it is necessary to add this adjustment to all the other cases.

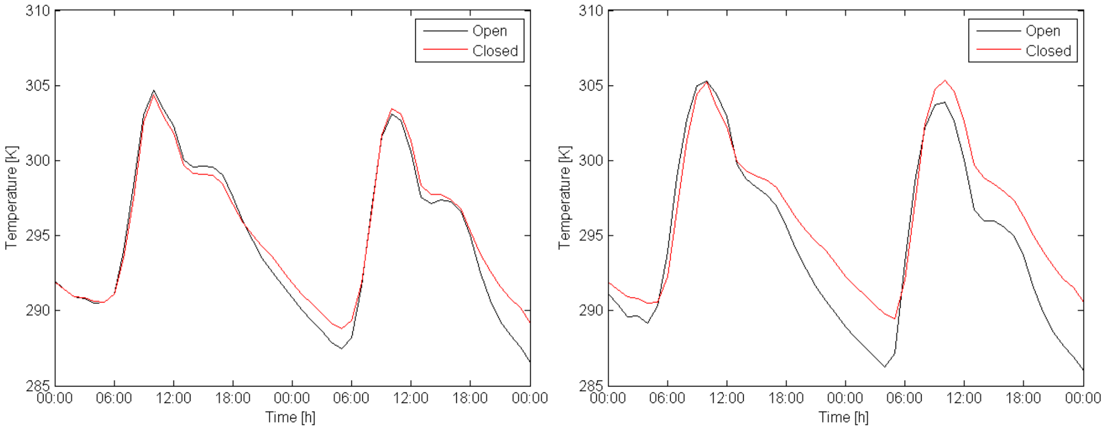

(A) '1 Rue de l'Argonne'

(B) '4 Rue de l'Argonne'

FIGURE 5.15: Results of simulation with and without closing

5.5.3 Vegetation in the canyon

Although vegetation does not influence surface temperature directly, it does contribute to the latent heat flux within the energy balance due to evapotranspiration. The effect of adding grass to the simulation can be seen in Figure 5.16. The maximum temperature differences (up to 2 K) are observed in the afternoon around 14:00 hours. In general, the adjusted model with grass has a lower surface temperature. Since energy is needed for evapotranspiration processes, this is not strange. Even though in case of building 1 no grass is modelled in front of the building (see also Section 5.2), the effects are still present.

Adding grass to the model does not influence simulation time significantly. As the fluctuations in temperature differences are significant, this adjustment can also be added to all the simulation scenarios.

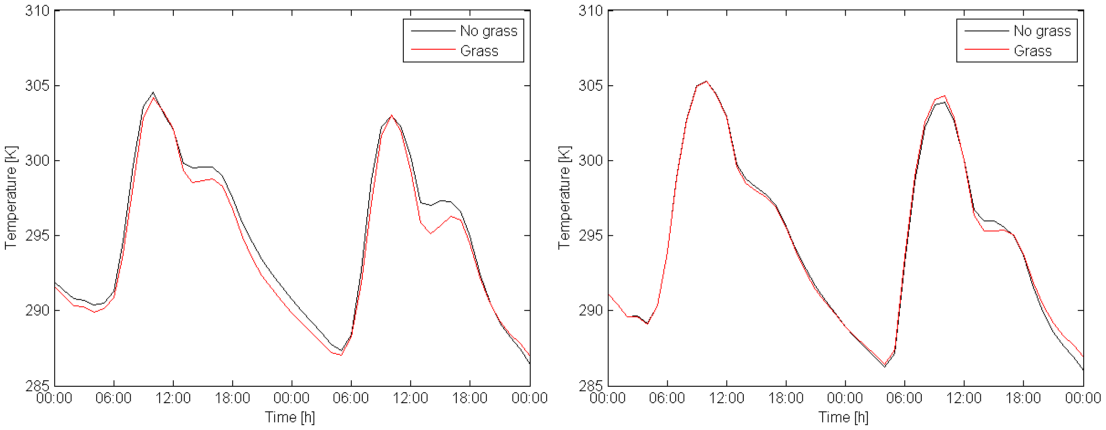

(A) '1 Rue de l'Argonne'

(B) '4 Rue de l'Argonne'

FIGURE 5.16: Results of simulation with and without grass

Chapter 6

Sensitivity test methodology

In order to determine the sensitivity of LASER/F to 3D geometry complexity, a methodology is developed, which is elaborated in this Chapter.

For the sensitivity test, thermal imagery is used. In Section 6.1 it is discussed how the thermal images are acquired and how they relate to surface temperature and radiant exitance. In Section 6.2 it is described why a comparison between the LASER/F surface temperature output and the brightness temperature from the thermal images is not valid and thus radiant exitance should be used. Different projection methods from LASER/F into the image domain and vice versa are discussed in Section 6.3. The determination of the camera position as well as the transformation method from the 3D model to the image space are described in Section 6.4.

The final projection implementation is in more detail described in Section 6.5. Why and how to exclude vegetation and windows from the comparison, as well as how to prevent occlusion, is elaborated on in Section 6.6. Finally, in Section 6.7, different evaluation methods are described in order to accurately determine LASER/F sensitivity to 3D geometry complexity.

Appendix E part B provides an overview of the work flow of the processes described in this chapter and how it relates to the others.

6.1 Thermal image acquisition

To be able to determine which simulation scenario yields the best results in the LASER/F simulations, measurements of the surface temperature are required. Due to the fact that each object at a temperature above the absolute zero emits energy in the form of radiation, its temperature can be sensed remotely. The amount of emitted radiation depends on the temperature as well as the wavelength of the radiation and the emissivity of the object surface.

This radiation can be measured by two types of infrared detectors, namely thermal detectors and quantum detectors. Both are based on the fact that through impinging photons a change of state in the detector is induced, which is then used to determine surface temperature of the object, if the emissivity of the surface is known. Nevertheless they differ in the way how the change of state is induced. Thermal detectors work on the basis of changes in temperature of the detector, which is induced by the incoming photons. The temperature change subsequently induces a change in current, voltage or conductivity within the detector. From this change the temperature of the target object can be derived. Quantum detectors however work on the basis of incoming photons directly inducing a change in current, voltage or conductivity, which is then related to the temperature of the target.

During the measurement campaign a FLIR SC665 thermal camera is used. The camera works with a microbolometer, a thermal detector which does not require cooling. This section focuses on the main specifications of this thermal camera, the measurement methodology, followed by an explanation of how the surface temperature can be obtained from the measurements.

6.1.1 Thermal camera specifications

The FLIR SC665 thermal camera is equipped with a lens that has a spectral filter to limit the spectral range to 9-11 µm. In this spectral band the variation in emissivity of the surface materials is minimized and the transmissivity of the air is high, resulting in a reduction of inaccuracies in the determination of the surface temperature. Further it can be calculated from Wien's displacement law,

$$\lambda_{max} = \frac{2898}{T} \quad [\mu\mathrm{m}], \tag{6.1}$$

that the radiant emittance of objects with a temperature T near 300 K is maximized at around 10 µm.

The most important specifications of the device are listed below [39]. The camera has a Field of View (FoV) of 25 x 18.8°. As the measurements from buildings are taken at an approximate distance of 19 m each time, an area of 8.4 x 6.3 m of the building facade is captured.

Resolution:	640 x 480	pixels
Focal length:	24.5	mm
Pixelsize (with 19 m distance to object):	1.3125 x 1.3125	cm
Spectral range:	7.5 - 13	µm
with spectral filter	9 - 11	µm
Detector pitch:	17	µm
Accuracy:	± 2	K

6.1.2 Measurement methodology

The most important buildings in the canyon for which the simulation results are obtained are buildings 1 Rue de l'Argonne and 4 Rue de l'Argonne, as described in Chapter 3. Although measurements could have been taken over the whole canyon, it was decided to focus only on the facades of the most important buildings. The main reasons for this are: measurements over the whole canyon would take too much time to do consistently and simulation results are only analysed over the most important buildings as the geometry of the AutoCAD model is inconsistent (see also Subsection 5.1.1).

An overview of all the measurement positions can be found in Figure 6.1. Four positions are used to measure building 4 Rue de l'Argonne (measurement points (MP 1-4), three positions for building 1 Rue de l'Argonne (MP 5-7) and finally one position on the second floor of the faculty of geography (3 Rue de l'Argonne). The last position offers additional information on 4 Rue de l'Argonne and the surface temperature of the ground. Measurements from the last position are only taken when sufficient time is available.

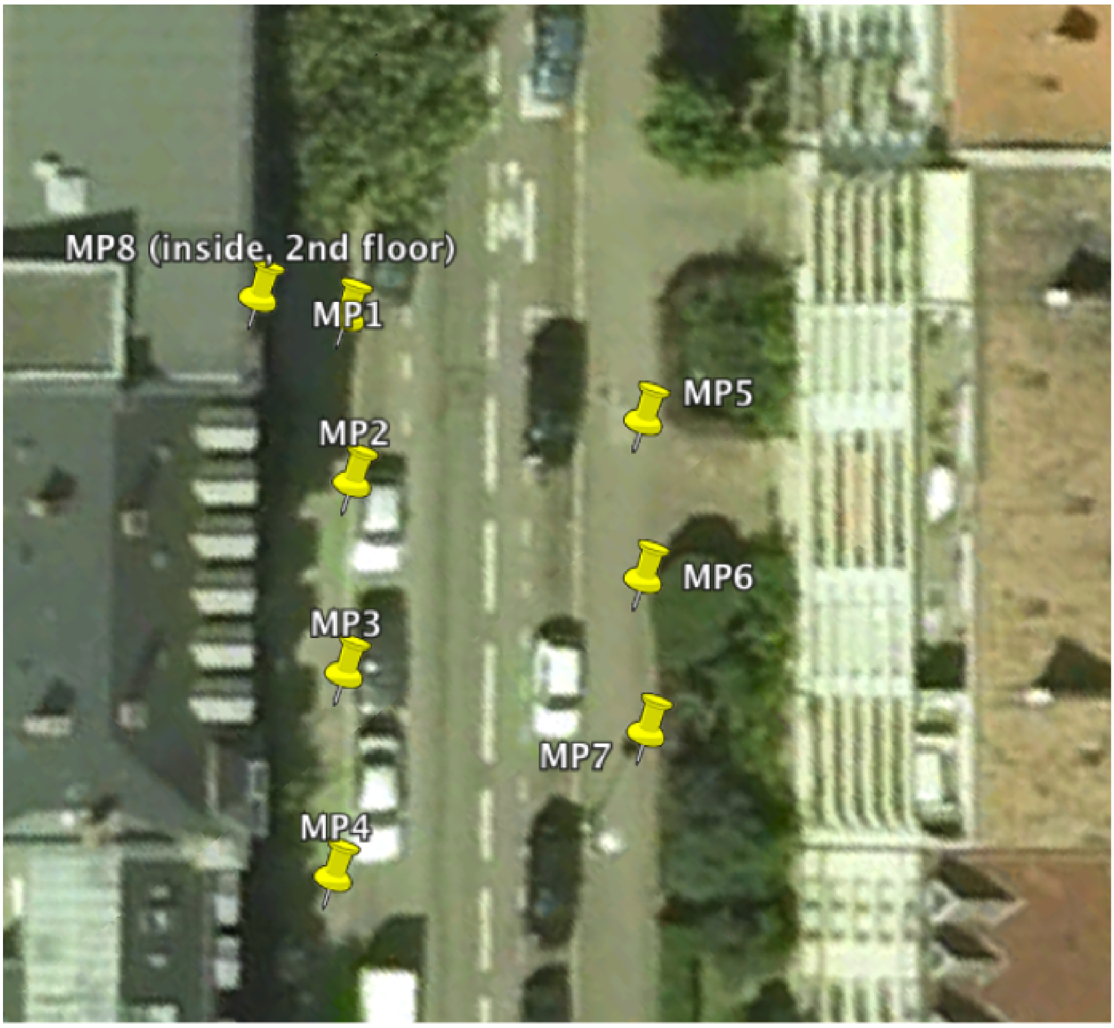

Figure 6.1: Measurement points within the urban canyon [5]

Measurements are taken during a time frame of 24 hours to capture the cooling and warming of the surfaces sufficiently. As normally surface temperature will decrease linearly from sunset till sunrise, measurements during the night (21:00-06:00) are set at a 3-hour-interval. In all the other cases, measurements are taken during a 1-hour-interval. Taking the sunrise/sunset times (according to Time and AS [40]) into account this results in 20 epochs to take measurements during the 24 hour time frame.

Considering the FoV mentioned in Subsection 6.1.1, multiple images need to be taken to capture the important building facades completely. For the ground positions this results in 12 images of 1 Rue de l'Argonne and 20 images for 4 Rue de l'Argonne per epoch. The additional position in the faculty of Geography yields 18 additional images of 4 Rue de l'Argonne per epoch.

6.1.3 The measurement formula

The thermal camera measures all radiation that impinges on its detector. If the thermal camera would measure a black body at a very close distance, a simple measurement formula could be used to obtain the surface temperature of the object. The radiant emittance W_{tot} of the object could then be related to the temperature T by the Stefan-Boltzmann law given in Equation 6.2, where σ is the Stefan-Boltzmann constant.

$$W_{tot} = \sigma T^4 \quad [\mathrm{W\,m^{-2}}] \tag{6.2}$$

Nevertheless, the object is not a black body at close distance and therefore all impinging radiation stems from three sources, which can be seen in Figure 6.2. These are the emitted radiation from the target object, the radiation reflected from the target and the radiation emitted from the air between the target and the camera. The individual components are also given in Equation 6.3.

$$W_{tot} = \epsilon\tau W_{obj} + (1-\epsilon)\tau W_{refl} + (1-\tau)W_{atm} \quad [\mathrm{W\,m^{-2}}] \tag{6.3}$$

On the left hand side of the equation the term W_{tot} is the total radiant flux density, the density that is measured by the camera. As in the above simplified case with the black body the camera then finds the temperature that is matching exactly to this radiant flux density. It is thereby clear that the obtained temperature is derived from all radiation impinging on the camera and that it is not the surface temperature, which is the desired quantity.

The first term on the right hand side of the equation is the radiant emittance of the object with the surface temperature T_{obj}. Because the object is not a black body the black body radiant emittance W_{obj} is multiplied with the emissivity ϵ of the surface. The radiant emittance is also attenuated by absorption and scattering particles in the

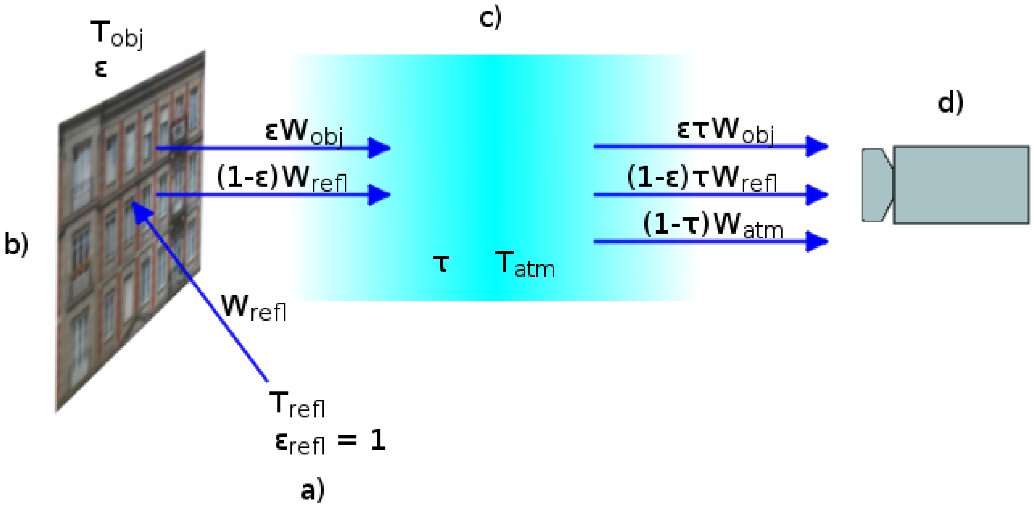

FIGURE 6.2: Radiation sources for thermal measurements. a) Surrounding; b) Target object; c) Atmosphere; d) Infrared camera (adapted from [6])

atmosphere between the target and the camera. Therefore the transmissivity τ of the atmosphere is taken into account in the measurement formula.

The second term of the equation expresses the radiation of the surroundings at temperature T_{refl}, which is reflected from the object surface. Similarly to the previous term its intensity is also attenuated by the atmosphere. The reflectance of the surface is $(1-\epsilon)$.

The last term is the radiation emitted from the atmosphere at a temperature T_{atm}. Here $(1-\tau)$ is the emissivity of the atmosphere. In general this radiation is small. Further the transmissivity of the atmosphere can be assumed to equal one. This assumption can be made because the distance from the facade surface to the thermal camera is short. Additionally the room in between contains air only, whose transmissivity in the thermal band of 9 to 11 µm is high. Since the transmissivity equals one, the radiation emitted from the air between the target surface and thermal camera drops out of Equation 6.3. Taking this into account the measurement formula simplifies to Equation 6.4.

$$W_{tot} = \epsilon W_{obj} + (1-\epsilon) W_{refl} \quad [\mathrm{W\,m^{-2}}] \tag{6.4}$$

This simplified formula can be used to correct the measured temperature for emissivity and reflected radiation . W_{tot} can be obtained from Stefan-Boltzmann's law using the temperature obtained from the camera measurement. The emissivity and reflected radiation are not known, such that values for these have to be assumed. The emissivity of the facade surface can be measured. However, measuring the emissivity is too complicated to do within the time frame of the project. Further a constant emissivity for each measurement has to be taken. Another less coarse option is to correct every thermal image with an emissivity value belonging to the different materials, however intensive processing of the data would be needed.

Knowing all terms in Equation 6.4 the value of radiant emittance ϵW_{obj} can be calculated as shown in Equation 6.5.

$$\epsilon W_{obj} = W_{tot} - (1-\epsilon)W_{refl} \quad [\mathrm{W\,m^{-2}}] \tag{6.5}$$

With Equation 6.6, derived from Stefan-Boltzmann's law, the surface temperature of the object can be obtained from the calculated radiant emittance.

$$T_{obj} = \sqrt[4]{\frac{W_{obj}}{\sigma}} \quad [\mathrm{K}] \tag{6.6}$$

As the camera uses a spectral filter it would be more accurate to calculate the surface temperature using radiance values at the central wavelength of the filter instead of radiant flux density. To do this the spectral radiance can be calculated from Planck's law, as given in Equation 6.7.

$$L_\lambda(T) = \frac{2hc^2}{\lambda^5(e^{hc/\lambda kT}-1)} \quad [\mathrm{W\,m^{-2}\,m^{-1}\,sr^{-1}}] \tag{6.7}$$

Then the simplified measurement formula given by Equation 6.4 changes into the formula given by Equation 6.8, which can be solved for the object's surface temperature T_{obj}.

$$L_\lambda(T_{tot}) = \epsilon L_\lambda(T_{obj}) + (1-\epsilon)L_\lambda(T_{refl}) \quad [\mathrm{W\,m^{-2}\,m^{-1}\,sr^{-1}}] \tag{6.8}$$

In the next section a sensibility study is done to show how the different values of emissivity and reflected radiation influence the accuracy of the object's surface temperature and which other error sources influence an accurate determination of the surface temperature.

6.2 Thermal image correction

As with any measurement corrections to the measurements need to be made in order to obtain accurate results. In the case of the measurements with the thermal camera two types of corrections need to be considered.

The first correction relates to the values of the measured quantity. As is explained in Subsection 6.1.3 the camera calculates the temperature on basis of the radiant exitance of the surface, which is the sum of emitted and reflected radiation. This temperature cannot be directly compared to the surface temperature of the LASER/F simulations and must be therefore either corrected or alternatively the radiant exitance has to be compared to the radiant exitance of the simulation. Because many variables influence the correction of the temperature it is arguable whether it can be corrected with reasonable accuracy. The second option would then give the more accurate comparison approach.

The second error source that has to be investigated is the geometric distortion of the camera. Because the values of the pixels in the images have to be compared with the simulated values at certain points of the model it is required that their geometric relation is accurate.

6.2.1 Determination of the surface temperature

The temperature measured by the camera is based on the total thermal radiation impinging on the camera, which implies that it does not equal the surface temperature of the target. As can be seen in the simplified measurement formula in Equation 6.4 it is therefore necessary to account for emissivity of the target surface and reflected radiation in order to obtain the surface temperature. Since these factors have not been measured it necessary to make assumptions for them. However, because not only the building facades but also each individual image contain targets with different material properties, geometry and surrounding thermal conditions, an accurate estimate of these values is often difficult or better to say, impossible. Taking into account these and other error sources this section aims to give an overview of the difficulties to determine the surface temperature. Further it is investigated in a sensibility study whether the targets can be assumed to be blackbodies due to a cavity effect and it is discussed whether this or the surface temperature are sufficiently accurate quantities to make comparisons with the LASER/F simulations.

Emissivity

Emissivity is the most important parameter to set correctly. For many of the building materials the emissivity value in the spectral band from 9 to 11 µm is similar, and lies around 0.95. Nevertheless, small deviations from this value result in considerable deviations in the surface temperature. Further the facades of both buildings consist of different materials, but assigning an individual emissivity for each object in the facade seems not feasible and therefore a single value has to be assumed for the whole facade.

An example of different material is shown in Figure 3.2 and 3.3, where parts of the facade are made of red brick and others of grey concrete. The measured temperature for a small part of the facade is given Figure 6.3, in which it can be seen that the measured temperature of the different materials is different. This difference must be regarded with care, as it is not clear how much of the difference is a result of varying emissivity values. Further, objects made of glass or metal have much lower emissivity values in the measured thermal band. For glass values of 0.8 to 0.9 can be assumed and for metal values go even down to 0.1. If for the whole image an emissivity of 0.95

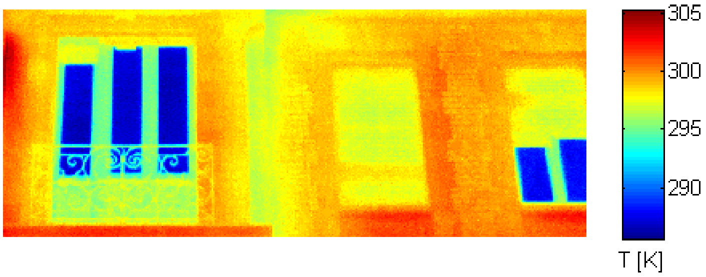

Figure 6.3: Measured temperature of a faade part that has different emissivity values

is assumed, objects with a lower emissivity appear colder than they are in reality. It therefore appears in Figure 6.3 that the windows are much colder than the rest of the facade. If on the other hand a lower emissivity is assumed for a surface, then it appears warmer than it is.

Reflected radiation

Because the facade materials are not blackbodies they reflect thermal radiation, which is emitted from other sources in the surrounding. This results in a higher measured temperature than the real surface temperature of the measured object. On the largest scale the sources of reflected radiation can be divided into scattered thermal radiation from the sky and thermal radiation from the objects in the urban canyon, like the facade of the opposite building, the street and pavement. An accurate estimation of these two quantities is already difficult and inaccurate. In addition, the complex shapes of the facades of close by objects might have a large contribution as a radiation source. To illustrate this one can consider the balconies in 4 Rue de l'Argonne. These are caved in and therefore each wall within a balcony reflects the radiation coming from the other walls of the balcony.

Because the reflectance is related to the emissivity through $(1-\epsilon)$ a lower emissivity results in a larger value of the reflectance. As most materials on the facade have high emissivity, their reflected radiation is relatively small. For materials such as glass the reflectance however is high and reflected radiation becomes a major source of error.

Further it has to be mentioned that most materials are diffuse reflectors. The glass of the windows in the facades is an exception here, as it is a specular reflector. An additional point is that its reflectance changes with the incidence angle and refractive index, e.g. for an refractive index of 2.25 the reflectance changes from 0.15 at an incident angle of 0° to 0.4 at an incident angle of 80° [41]. From these two points it follows that windows at different heights reflect radiation with varying intensity and from different sources. Windows at high height reflect radiation from the sky, whereas windows at lower height reflect the radiation from the opposite facade as can be seen in Figure 6.4. The reflected sky radiation could be removed from the measurement formula, the reflected radiation from other sources however is due to its high variation the windows.

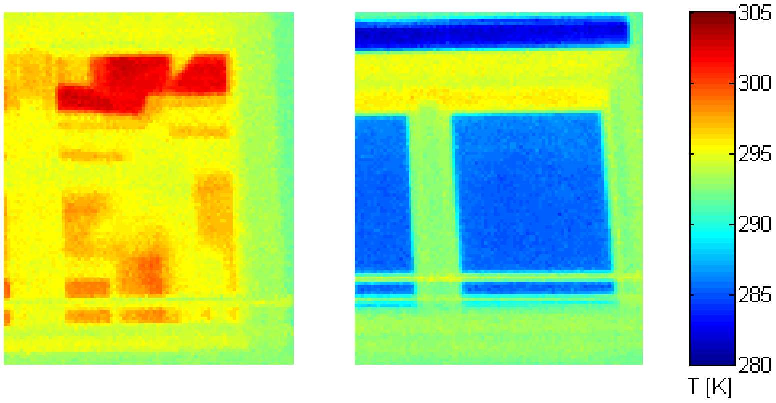

FIGURE 6.4: Measured temperature of two different windows with reflections from the opposite facade (left) and reflections from the sky (right)

Knowing the potential error sources it becomes clear that it is not possible to account for them during the derivation of the surface temperature of each object accurately. As such it is much more important to find a simplified correction method for the measured temperature in order to find a surface temperature which can be compared to the LASER/F simulations. An alternative would be to use the calculated radiant exitance from the measured temperature and compare it to the radiant exitance values of the simulation, which is going to be used for the comparison in this project.

Compensation effect

Because the measurements are taken in a canyon it could be assumed that the influence of reflected radiation and emissivity compensate for each other. This can be clarified when the temperature of the surroundings is equal to the surface temperature of the measured object as written in Equation 6.9.

$$L_\lambda(T_{tot}) = \epsilon L_\lambda(T_{obj}) + (1-\epsilon) L_\lambda(T_{obj}) \quad [\mathrm{W\,m^{-2}\,m^{-1}\,sr^{-1}}] \tag{6.9}$$

This formula would then simplify to Equation 6.10. In this case the measured radiance would be the same as the radiance of the surface at temperature T_{obj}, and T_{tot} would equal T_{obj} Therefore T_{obj} could be obtained without making any corrections, i.e. without knowing the values of the emissivity and reflected radiation.

$$L_\lambda(T_{tot}) = L_\lambda(T_{obj}) \quad [\mathrm{W\,m^{-2}\,m^{-1}\,sr^{-1}}] \tag{6.10}$$

It is clear that this assumption might not be exact because the reflected radiations come from different sources at different temperatures and not at the surface temperature of the measured object itself. One major source of the reflected radiation is the sky, which has a much lower temperature then the building surfaces. During the campaign it was measured to be approximately −50 °C, which was the case during clear sky conditions. During non-clear conditions its value increases. The other source, the canyon itself, is however at a similar temperature as the measured object.

To investigate, how the measured temperature T_{tot} and the surface temperature T_{obj} are related under this assumption, a sensibility study is simulated. This study shows how the emissivity, surface temperature, surrounding temperature and measurement point influence this assumption. To calculate the parts of irradiance incident on the facade, i.e. from the sky and the canyon, at a certain height of the building their proportion has to be calculated at each height x. In Figure 6.5 building 1 and 4 in Rue de l'Argonne are represented. Here, representatively, only the calculations for building 1 are considered, as they are similar for building 4. The angle θ is related to the total height H (26.9 m) of building 4, the horizontal distance L (29.6 m) of the facade to the roof top of building 4 and the variable height x by .

$$\tan\left(\frac{\pi}{2} - \theta\right) = \frac{H - x}{L} \tag{6.11}$$

The proportion of the sky view α is then obtained from Equation 6.12 and the proportion of the canyon view is $1 - \alpha$.

$$\alpha = \frac{\theta}{\pi} \tag{6.12}$$

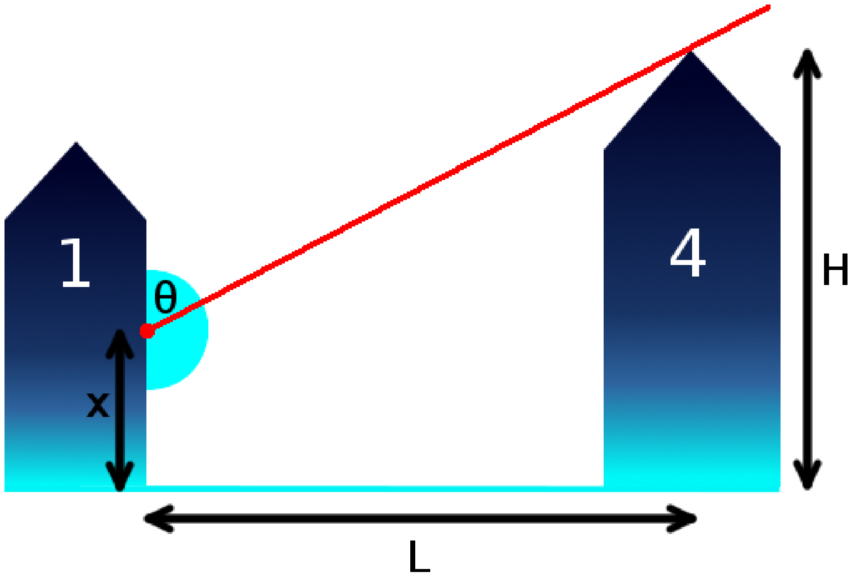

FIGURE 6.5: Schematic representation of building 1 and 4 in Rue de l'Argonne to derive the proportion of the sky view at each facade (not to scale)

Knowing these proportions the measurement formula can be adapted such that radiation from the sky and the canyon are treated separately, where it is assumed that the canyon has the same temperature T_{obj} as the measured object and the sky has temperature T_{sky}:

$$L_\lambda(T_{tot}) = \epsilon L_\lambda(T_{obj}) + (1-\epsilon)\left[(1-\alpha)L_\lambda(T_{obj}) + \alpha L_\lambda(T_{sky})\right] \tag{6.13}$$

The radiance values on the right hand side are calculated with Planck's law (Equation 6.7) at a wavelength of 10.5 µm to obtain the spectral radiance $L_\lambda(T_{tot})$ on the right hand side. From this the temperature T_{tot} that would be measured by the camera can be calculated by inverting Planck's law. The difference between T_{tot} and T_{obj} can be seen in Figure 6.6.

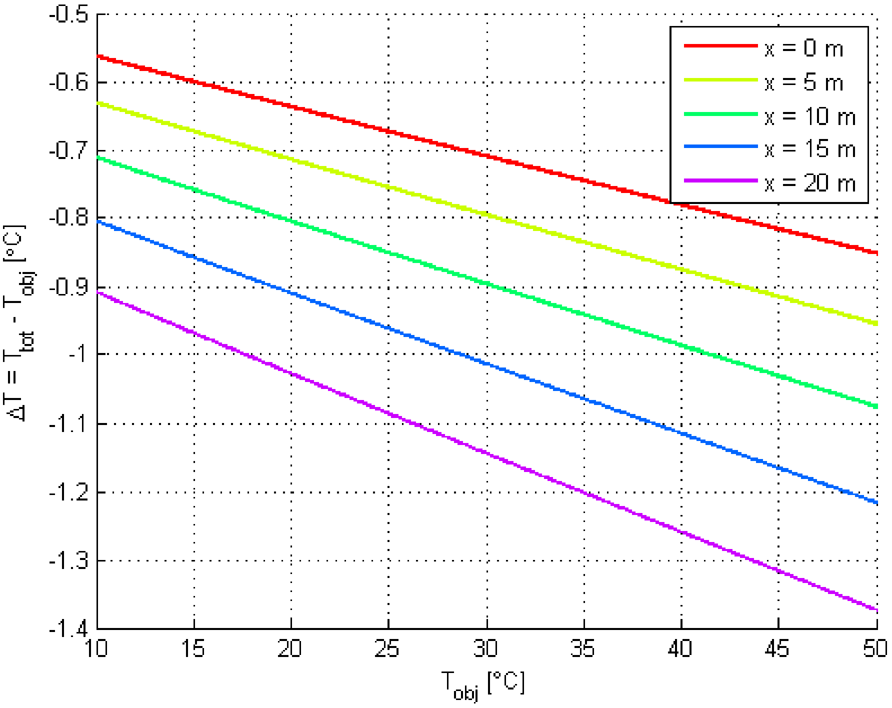

FIGURE 6.6: Difference between T_{obj} and T_{tot} with $\epsilon = 0.95$ and $T_{sky} = -50\,°C$

From this graph it can be concluded that the measured temperature is slightly lower than the surface temperature. This is expected for surface temperatures above the sky temperature. If the sky temperature rises the error also becomes smaller. Further the error is larger at the top of the facade, because the proportion of sky view is largest there. At the bottom of the facade the error is smallest. With ϵ equal to 0.95 and T_{sky} equal to $-50\,°C$ the lowest difference is $-0.6\,°C$ and the largest $-1.4\,°C$ for surface temperatures in the range from 10 to 50°C. For a sky temperature of $-20\,°C$ these values would reduce to $-0.3\,°C$ and $-1.1\,°C$, respectively. For materials with lower emissivity the difference increases more. For ϵ equal to 0.9 and T_{sky} equal to $-50\,°C$ the lowest difference is $-1.1\,°C$ and the largest $-2.7\,°C$.

It can be seen from the study that using the measured temperature for comparisons with the surface temperature of the LASER/F simulations would lead to inaccurate results. This is certainly the case as the aim of the project is to investigate how sensitive the simulation is to small changes in detail of the modelled facades. Nevertheless the results of this study could be used to improve the accuracy of the measured temperature.

LASER/F validation based on radiant exitance

As the derivation of an accurate surface temperature is problematic an alternative approach can be used to compare the measurements with the LASER/F simulations. The measurement formula shows that the measured temperature is based on the sum of radiant emittance and reflected radiation, i.e. the radiant exitance. It was shown that the radiant exitance cannot be split back into its two components. Nevertheless, the LASER/F simulation supplies the individual values of radiant emittance and reflected radiation. Their sum, the radiant exitance, can be used to make comparisons with the radiant exitance from thermal imagery, which can be calculated from the measured temperature with Stefan-Boltzmann's law (Equation 6.2). In this case no error sources, like emissivity or reflected radiation, must be accounted for.

6.2.2 Geometric camera calibration

By calibrating the camera geometrically, parameters as lens distortion coefficients and focal length in pixels can be estimated. Lens distortions coefficients are useful to investigate as they can help in rectifying images. Estimation of focal length can serve as an indicator of whether the focal length stated by the supplier is correct and as useful input for providing estimates for methods as space resection (see Section 6.4).

There are many ways to calibrate images [42]. In this project, two different approaches are used: the Matlab camera calibration toolbox as implemented by Bouguet [43] and a calibration algorithm of the TU Delft (Ben Gorte, Optical and Laser Remote Sensing).

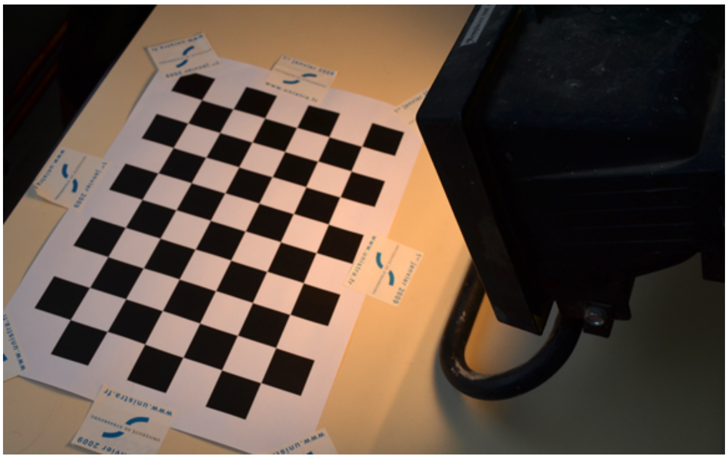

FIGURE 6.7: Set-up for obtaining thermal calibration images

As the FLIR SC665 camera is a thermal camera, images were obtained by capturing thermal imagery from a regular chessboard pattern heated by artificial lighting (Figure 6.7). As a heated pattern is captured, the pattern is rather diffuse making it harder to detect corners (Figure 6.8).

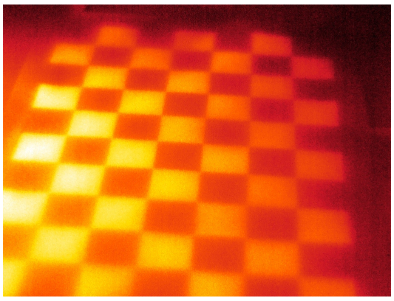

FIGURE 6.8: Example of a calibration image

The results of corner detection can be seen in Figure 6.9. The Matlab camera toolbox makes use of Harris' corner detection method [44], while the TU Delft algorithm makes use of least-squares matching to obtain corners. The diffuse pattern makes it harder to automatically detect corners. In the case of the Matlab camera toolbox, which needs multiple calibration images as input, a selection needs to be made based on quality of the calibration images. Also several iterations are needed to improve corner extraction. In the case of the TU Delft algorithm one calibration image is sufficient.

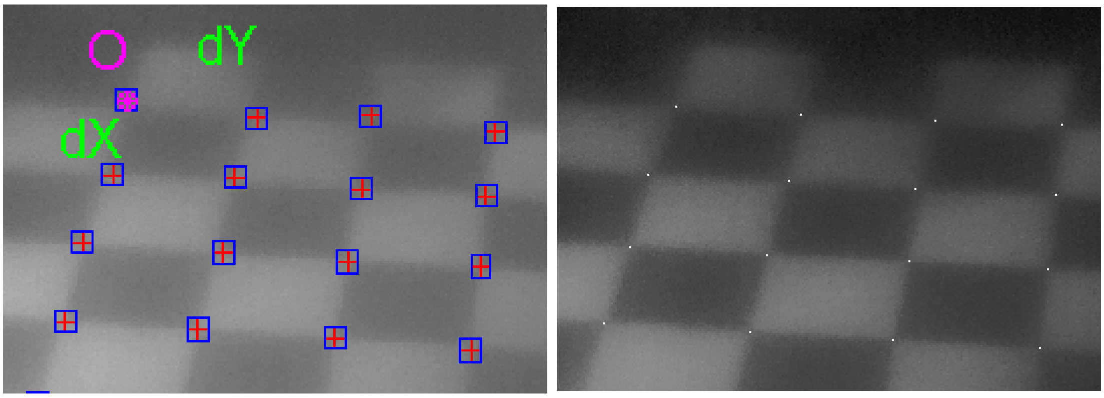

(A) Matlab camera calibration toolbox (B) TU Delft algorithm

FIGURE 6.9: Results of corner detection of different programs used for camera calibration

Considering the specifications offered by the manufacturer of the thermal camera, the focal length should be ± 1442 pixels [39]. The Matlab camera calibration toolbox yields a focal length in x-direction of 1528 ± 37 pixels and in y-direction of 1535 ± 38 pixels. The algorithm of the TU Delft yields a focal length of approximately 1523 pixels. As both methods make use of the deformation of a rectangular grid to estimate the parameters of the camera, the quality of estimations is dependant on the automatic detection of grid corners in the images used. As the imagery is thermal imagery, noise will be present causing the difference between the estimation and the specifications of the manufacturer, causing estimations to be coarse. Whether the specification of the manufacturer is reasonable can still be checked by calibrating with a fixed focal length. The residuals of the estimation at corner locations of this case are slightly larger, but do not increase significantly. This indicates that the manufacturer information is correct.

Lens distortions are negligible in both cases. In the case of the Matlab toolbox the distortion coefficients are found equal to zero within their uncertainties, in the case of the TU Delft algorithm the effect of re-projection of the image with distortion coefficients is found to be negligible compared to the one without.

Both methods yield similar values, which are heavily influenced by the quality of the thermal imagery. The focal length as given by the manufacturer can be used as an estimate in methods as space resection (see also 6.3.1).

6.3 Projection methods

The output of the LASER/F model needs to be compared with the thermal images. The comparison is to be based on both the simulated and the measured values which have been converted to radiant exitance for reasons described in Section 6.1. The difficulty in making this comparison is that the thermal images are 2D whilst the output of the LASER/F model is 3D. As such, either the thermal images need to be converted to the 3D domain or the LASER/F output need to be converted to 2D. In this section the different methods are discussed.

6.3.1 Conversion of LASER/F output to 2D

Perhaps the most straightforward method for evaluating the results is to recreate the thermal image in the the LASER/F model. To do so an image needs to be captured in the 3D scene from the same location and orientation of the camera and with the same internal camera parameters as during the measurements. However the rendering in LASER/F uses a perspective projection from computer science which differs slightly from the collinearity equations which are used to determine the camera position. An example is the use of FoV instead of the focal length used in the collinearity equation, though they are related by the diagonal of the film, x, as can be seen in Equation 6.14.

$$FoV = 2\arctan(x/(2f)) \tag{6.14}$$

A thermal image can only be compared with one image from the LASER/F model at the same time. After the image has been taken, every pixel can be compared with one in the measured thermal image.

Creation of the 2D model image

The LASER/F model provides two kinds of output, both of which can be used in a different way to obtain a 2D image. A visualisation is provided in which the radiances can be mapped onto the surfaces. Like can be seen in Figure 6.10 also a color bar is provided so that the radiant exitance can be calculated for each pixel in the image and can then be compared with those in measured image. LASER/F also provides an ASCII output containing the 'x,y,z' coordinates of the triangle's vertices, their center points and the corresponding attributes. An example output can be seen in Appendix D. The location of each of these points within the view of the camera can be calculated using the collinearity equations. More about this can be found in Section 6.5. Some points are behind a wall, this should be taken into account by using the distance to the camera. Once the points have been mapped onto the image it can be compared to the thermal image.

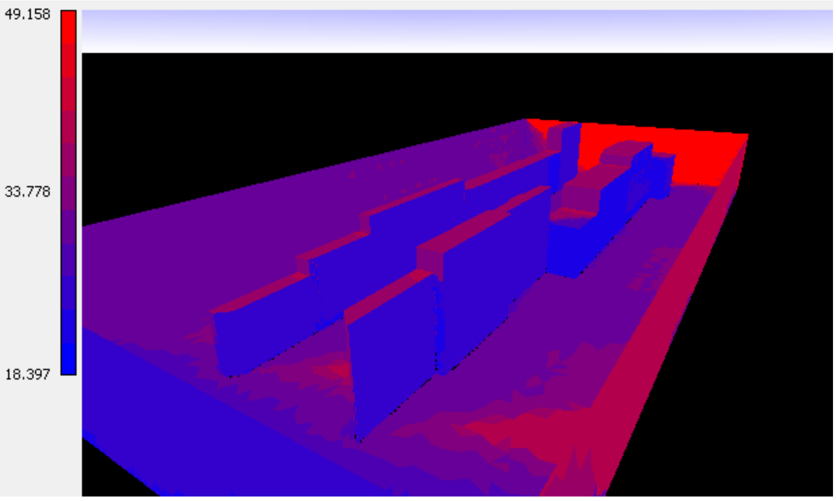

FIGURE 6.10: An example output of the LASER/F model

A slightly different approach is to map one point to every image from the time step and check which image captures the point best and evaluate the point there. The process should then be repeated for every simulated point separately. The accuracy of both of the images depends mostly on the accuracy by which the camera orientation has been determined. When enough data is used as input the accuracy can be very high.

6.3.2 Projection of thermal images onto the 3D model

To get the thermal image into the 3D scene the image can be wrapped or projected onto the 3D AutoCAD model. There are multiple ways for obtaining this result. A distinction can be made between finding and writing software to do the processing. The in- and output needed for existing software will depend on the software, however it is likely that points in the image should be matched to points in the 3D AutoCAD model and that the output are textures for the triangles in the model. The main disadvantage here is that the 3D geometry has to be added to the 2D thermal image, while in the previous options the third dimension is removed from the data. As such when either using texture mapping software, or projecting the thermal image, in both cases the accuracy of the output is expected to be lower.

Relation between the thermal images and the 3D model

Before the thermal images can be mapped, the relation with the 3D model needs to be found. One option is obtaining the camera orientation, like discussed in Subsection 6.3.1. Alternatively, using orthography the simulated images can be created. An orthophoto is a rectified image which also considers 'height' differences in the surface [45]. The orthophoto can be created from multiple images. Once created, just a few reference points are needed to project the image straight onto the building. The downside is that the creation of orthophotos is very time consuming. By only rectifying the image and then projecting it, the process is much faster however the assumption of a flat facade is not very accurate, especially considering the balconies of 4 rue de l'Argonne.

The actual projection

There are also at least two options for the mapping of the thermal pixels onto the 3D scene. The first is by casting rays from the camera position, through each pixel in the thermal image and determining the first surface intersected by the ray. The location of intersection is where the pixel should be mapped to. Another approach is to map the triangles from the Computer-Aided Design (CAD) model onto the thermal image, extract the pixels covered by the mapped triangle and use it as the texture for that triangle. When implementing this method it is important to consider the footprint of projected pixels and interpolation within the textures. The projected pixels might be clustered in areas, which negatively impacts the validity of the results.

6.3.3 Creation of a 3D point cloud from the thermal images

Instead of using the 3D AutoCAD model the 3D geometry can also be reconstructed using images only, although the model is still needed for conversion to the correct coordinate system. A 3D point cloud can be created by obtaining the distance to the 'camera' from stereo images. By calculating the parallax of corresponding points between pictures the distance to the cameras can be determined. After converting the points to the same system as the 3D AutoCAD model, the measurements can be compared with the simulated model.

Stereo viewing requires overlapping photographs which are truly perpendicular and there should be no relative tilt between the two images. Furthermore the eye base should be parallel to the translation direction of the camera and the photographs should be of the same scale. Since most of these requirements are not met by the thermal images, trying to implement this is ruled out as the likelihood of success or otherwise accurate result is too small. However when software becomes available this option can be reconsidered.

6.3.4 Validation method comparison

Since trying to create a point cloud from just the thermal images does not appear to be feasible it is not considered in the comparison. This basically leaves two options: one in which the validation will be performed in 2D (image recreation) and one in 3D (texture mapping).

2D Images allow for more advanced validation methods, for example methods that use neighbouring pixels. In the case of point clouds or separate textures this is much less so. The 2D method also has fail safes ensuring that validation will at least be possible. On the other hand texture mapping in 3D provides a visibly more appealing result and it requires more technical skills. The latter will however not hold when available software tools will be used to process the images. More important is that, since in 2D data is removed while in 3D data needs to be added, the accuracy of the 2D approach is expected to be higher.

For validation purposes the 2D image recreation method is more feasible. As such the validation is expected to be between sets of two images, one measured and one simulated.

6.4 Camera positioning

As is described in Section 6.3, the external orientation (camera position and orientation) of the thermal camera is needed for the 2D image recreation approach. There are different methods to obtain these positions. They can either be manually measured during the acquisition of thermal imagery, or acquired through photogrammetric methods. As at the time of the project there was no equipment available to determine the precise orientation of the camera, only the approximate position could be measured with help of GPS. The results of these GPS measurements can be found in Section 6.4. Considering photogrammetric methods both bundle adjustment as space resection are considered, which are detailed in Subsection 6.4.2 and Section 6.4 respectively.

6.4.1 GPS positioning for thermal camera

The exact position of the thermal camera during the measurement campaign was decided to be obtained by using Differential Global Positioning System (DGPS) in order to achieve an accuracy of 2 to 3 cm. The receiver used for this method is a dual frequency Leica GPS1200 using carrier phase measurements for better accuracy. However, since the measurements are taken in an urban canyon some difficulties have been encountered which led to unacceptable accuracies. As a consequence, data cannot be post-processed. The problems that are encountered are briefly explained here.

The most important problem is that the camera during the field measurements was set up near tall buildings in the canyon. This causes significant multipath errors which degrades the accuracy of the positioning by 5 to 7 m. Another noticeable issue was the weak geometry of the satellites during the measurement. The Geometric Dilution Of Precision (GDOP) was changing from 6 to 10 during the measurement period which explains a very weak geometry of GPS satellites. Normally, this value should fluctuate from 2 to 3.5 for having reasonable accuracies. These two problems are the main reasons that the accuracy of the measurements could not get better than 2 m even when the GPS receiver was fixed for approximately 2 hours.

Another problem that is encountered is that buildings in the street caused sky obstruction which led to occurrence of *cycle slips*. This means that the receiver is not able to track GPS satellites and the signal was interrupted during the measurement period. This problem could have been solved by using assisted GPS (aGPS), however, measurement devices using this technique were not at hand during the project.

All the above-mentioned problems caused GPS positioning to be unsuccessful. Therefore, it is not possible to post-process the data and it is decided to calculate the position of the camera by using photogrammetric methods which is explained in the following subsections.

6.4.2 Bundle adjustment

Bundle adjustment offers a method to simultaneously determine camera calibration parameters as well as camera position and orientation [46]. As it can process a lot of images from different positions and orientations at once, it seems ideal to use for finding the external orientations of the thermal camera per building facade.

Considering the time frame of the project and the popularity of bundle adjustment as a method, it is decided to try using available freeware for bundle adjustment: Bundler [47] and VisualSFM [48]. Although main interest involved obtaining camera position and orientation, these software packages also offer possibilities to extract 3D point clouds from imagery.

Even though both packages are able to work with the thermal imagery, there are several issues encountered during the processing:

- Characteristic features in images are harder to automatically detect and match in thermal imagery

- Overlap between thermal images from one epoch is relatively small
- Results are presented in a different coordinate system

The first two issues cause a lot of thermal images to be rejected during processing and affect the accuracy of the output. Although for 4 Rue de l'Argonne decently overlapping images were available due to the measurements from inside the faculty of geography (MP8), the first issue still caused rejection. Since even over different epochs the same images get rejected, it is impossible to obtain camera orientations and positions for each thermal image.

Furthermore, as the coordinate system of the output is unknown, it is harder to transform it to the correct coordinate system of the 3D model. Not only translation and rotation have to be taken into account, but also scale. VisualSFM does offer an option to specify ground control points, but as only a few thermal images get accepted it is not enough.

Bundle adjustment could have been used as a method for obtaining camera parameters if there would have been more overlap between the thermal images, or if more control over the detection and matching of features could be exercised. As it would take too much time to solve the issues encountered, it was decided not to use bundle adjustment to position the thermal images.

6.4.3 Space resection

Space resection is a method to determine the camera position and orientation from an image knowing at least three ground control points. To do this the method makes use of the collinearity equations 6.15a and 6.15b.

$$x = -f\frac{m_{11}(X - X_c) + m_{12}(Y - Y_c) + m_{13}(Z - Z_c)}{m_{31}(X - X_c) + m_{32}(Y - Y_c) + m_{33}(Z - Z_c)} \tag{6.15a}$$

$$y = -f\frac{m_{21}(X - X_c) + m_{22}(Y - Y_c) + m_{23}(Z - Z_c)}{m_{31}(X - X_c) + m_{32}(Y - Y_c) + m_{33}(Z - Z_c)} \tag{6.15b}$$

In this equation x and y are the pixel coordinates of a ground control point in the image. X, Y and Z are the respective coordinates of the ground control point in ground space coordinates. X_c, Y_c and Z_c are the camera position coordinates in ground space coordinates. The terms m_{ij} result from the rotation matrix, which rotates the camera view by the angles ω, ϕ and κ.

The collinearity equations are constructed for each ground control point, taking the respective values for x, y, X, Y and Z. Next these equations are linearised and least squares adjustment is used iteratively until the best values for the external camera orientation, X_c, Y_c, Z_c, ω, ϕ and κ, are obtained. This method can be applied to one image or many images at the same time.

Ground control points

To obtain the external orientation parameters of the camera from one image, it is required to have at least three ground control points in the image. Because a 3D model of both facades is available, the coordinates of the ground control points can be easily obtained. For 1 Rue de l'Argonne 139 ground control points are taken from the model and for 4 Rue de l'Argonne 122. These points are selected such that they can be identified easily in the thermal images. They include the corners of windows or window frames, balconies and corners at the roof. To each control point an individual identification number is assigned, such that its coordinated can be extracted easily.

The next step is to select the ground control points in each of the thermal images. For 1 Rue de l'Argonne three images were acquired from each of the three positions MP5 to MP7 (see Figure 6.1), resulting in nine images per epoch. For 4 Rue de l'Argonne five images were acquired from the four positions MP1 to MP4 and eighteen from position MP8. Nevertheless the lowest images of positions MP1 to MP4 are images of the street and do not contain the facade. Also, although position MP8 offers additional information on 4 Rue de l'Argonne, measurements from this position were not taken over each epoch consistently. Processing these images would cost additional time without guaranteed results. It was therefore decided not to use these extra images in the space resection. Sixteen images from positions MP1 to MP4 for 4 Rue de l'Argonne are used in the end. Since measurements are taken at twenty epochs, the pixel coordinates of the ground control points in 500 images have to be found.

To accelerate this process an user interface has been created in Matlab. The interface makes it possible to adjust the scale of the temperature, such that the contrast of the image is enhanced and the ground control points are found easily. Next the pixel coordinates of the ground control points are selected by clicking them in the image and subsequently the correct ID to the point in the image is assigned, such that the pixel coordinates can be linked to the ground coordinates of the model. The pixel coordinates and the ground coordinates of the ground control points are saved in a separate file for each image. An image of the interface is shown in Figure 6.11.

Even though it is possible to zoom into the images, it is often difficult to select the ground control points in the thermal images accurately. The reason for this is that the thermal images are not as sharp as RGB images and that the contrast of the values at the control points is not high. Further some images are badly focused, such that the position of the ground control points can only be estimated. Further several parts of the 3D model seem to be inaccurate. It was therefore avoided to select ground control points in these parts, if not necessary. Due to these error sources on average five to eight points were selected in order to minimize errors in the result of the space resection.

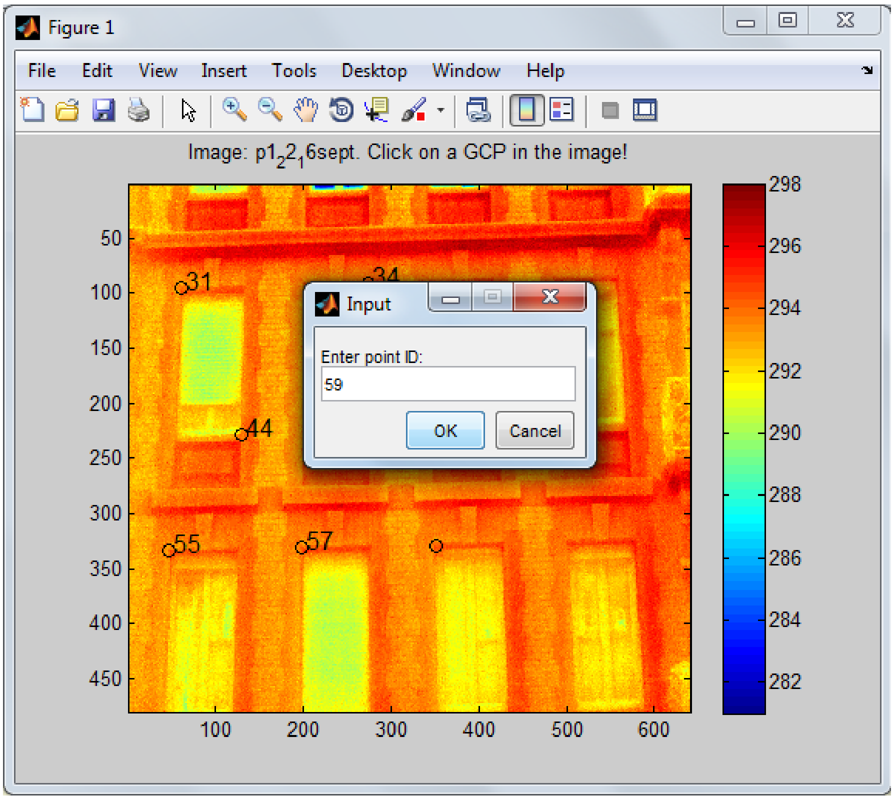

Image: p1$_2$2$_1$6sept. Click on a GCP in the image!

Enter point ID: 59

FIGURE 6.11: User interface to select ground control points in thermal images

Assuming the same position

At each individual epoch several images are taken from each of the seven positions. Further at each other epoch the camera was positioned back to the same position. It is assumed that the position of the camera did not change more than a few centimetres throughout all epochs, because the position of the camera's tripod was marked on the pavement. This fact was exploited during the space resection. Space resection recursively solves a system of equations with least squares adjustment. For a single image the variables of this system are the six external camera orientations, namely the three orientation angles κ, ω and ϕ and the three Cartesian coordinates X_c, Y_c and Z_c. The system of equations can be expanded by adding the equations of additional images. Each additional image adds three new variables, namely κ_i, ω_i and ϕ_i, where i is the number of the image. The values for X_c, Y_c and Z_c stay the same of all images, as the camera position does not change.

Initial estimates of the external camera orientations

To solve for the external camera orientations an initial estimate of those is required for the first iteration. If these values are considerably off from the true values it is possible that the results of the iterations do not converge. Therefore the initial camera position is estimated visually on basis of a point cloud plotted from all ground control points, since it is known approximately where the camera was positioned with respect to the facades. The initial estimates of the orientation is a bit more difficult. Here the sequence of the rotation matrices must be taken into account. The orientation for the first image was found by trial and error. Based on these values the initial orientations for other images could be concluded.

Focal length

The space resection has first been performed with the focal length as an additional variable and at one epoch only for testing purposes. This resulted several times in an unstable behaviour of the space resection. If the space resection algorithm did not crash, the resulting focal length varied often by tens or even hundreds of pixels. As a consequence also the camera position varied when tested at other epochs. Despite these uncertainties the method also yielded frequently a focal length not more than a few pixels off of the value 1441.2. This is exactly the focal length calculated from the focal length of the camera given in mm and the detector pitch (see Equation 6.16).

$$f = \frac{24.5\,\mathrm{mm}}{17\,\mu\mathrm{m}} = 1441.2\,\mathrm{pixels} \tag{6.16}$$

This value of the focal length is used as a fixed value for the space resection of all images of the twenty epochs at each of the seven positions.

Resulting external camera orientations

The resulting coordinates of the camera positions are given in Table 6.1. The Z_c value give an indication on the accuracy of the camera positions. Since the Rue de l'Argonne appears to be street without inclination and the height of the camera's tripod is constant, all camera positions should have a similar height, i.e. a similar Z_c value. It can be seen that five of the values lie within a range of 14 cm. The Z_c values of MP2 and MP7 deviate slightly more, but are within 30 cm to the mean value of 21.27 m. According to the similarity of these values it can be concluded that the accuracy of the positions is reasonable.

In Table 6.1 also the mean pixel error is given. With the obtained external camera orientation parameters the ground control points can be projected back onto the thermal images. The distance of the projected points to the points that where selected is the pixel error. This error value is calculated for all selected points and their mean is calculated. These values seam high at first, but it has to be considered that errors are accumulated from inaccuracies in the 3D model and the clicking of the ground control points in the thermal images. The discrepancy of selected and projected points for an example image with rather large error is shown inFigure 6.12.

Position	$\mathbf{X_c}$	$\mathbf{Y_c}$	$\mathbf{Z_c}$	**Mean pixel error**
MP1	−51.42 m	18.49 m	21.16 m	5.16 pixels
MP2	−54.66 m	13.90 m	21.41 m	5.00 pixels
MP3	−58.47 m	8.05 m	21.24 m	5.93 pixels
MP4	−61.73 m	3.70 m	21.27 m	7.05 pixels
MP5	−45.88 m	6.58 m	21.13 m	4.12 pixels
MP6	−49.53 m	1.97 m	21.13 m	4.12 pixels
MP7	−52.55 m	−3.63 m	21.57 m	5.42 pixels

TABLE 6.1: Cartesian coordinates, X_c, Y_c and Z_c, of camera positions MP1 to MP7 (as in Figure 6.1) in the coordinate system of the 3D model

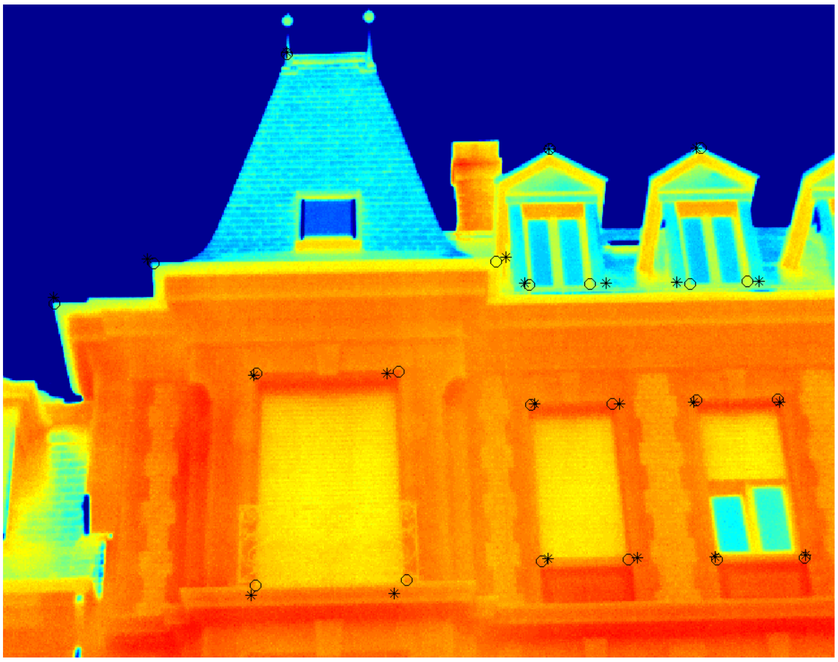

FIGURE 6.12: Selected points (marked by circles) and projected points (marked by asterisks)

6.5 Projection method implementation

In Section 6.3 is described why the comparison is to be done by projecting the 3D model into the image domain. This section explains how the projection is implemented. The camera orientation parameters acquired in Section 6.4, together with the geometry from the LASER/F ASCII output serve as an input to the projection. The result of only the projection algorithm is an unfiltered image geometrically similar to the measured thermal image.

6.5.1 Projection of points

Where space resection iteratively solves the collinearity equations with known points to get the camera orientation (Subsection 6.4.3, projecting points from the 3D model into the image is exactly the opposite. To project a known 3D point, the camera rotation parameters ω, κ, ϕ, the camera translation parameters X_c, Y_c, Z_c and the focal length f of the camera are needed to solve the collinearity equations. The outputs of one such calculation are the lower case x and y parameters which indicate the location of the point in the image.

For correct positioning, the resulting x and y still need to be rounded to the nearest integer and translated by half the image height and width. When this is done an image like Figure 6.13 can be created in which the center points of each of the triangles have been projected onto the thermal image. Points projected outside the boundaries of the image have been removed.

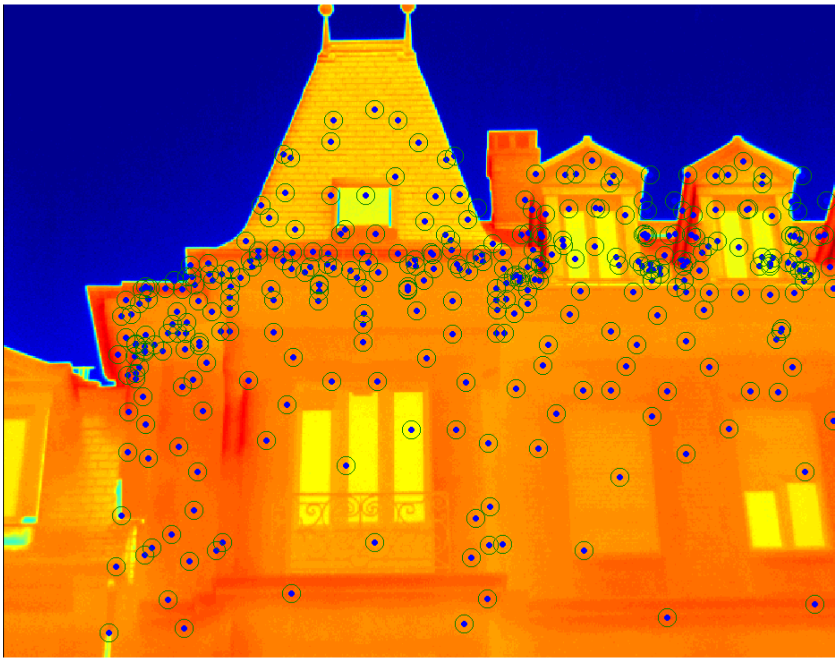

Figure 6.13: LASER/F center points projected onto the thermal image

6.5.2 Projection of triangles

Before the 3D model can be projected into the image domain, the list of triangles should be filtered in such a way that only the triangle of the front of the facade and the roof of the building of interest are included. The back and side walls of the building are removed by using a manually defined bounding box. Triangles with center points inside the bounding box are selected. To filter the neighbouring building the object number for which most triangles had previously been selected is used to determine which of the semi-randomly assigned object numbers is the building of interest.

Calculating how triangles should be mapped is an extension to projecting single points. For a triangle in the 3D model the vertices are projected into the image domain. The three vertices are snapped to the grid of the raster image after which they are connected by lines. The edges of the triangle have now been projected. A filling algorithm is used to identify every pixel contained by the triangle. The identified pixel can then be given the radiant exitance value from the corresponding triangle of the LASER/F model. It is important to use a raster algorithm opposed to vector algorithms such as point-in-polygon, because the computation time is much shorter, while giving the same results.

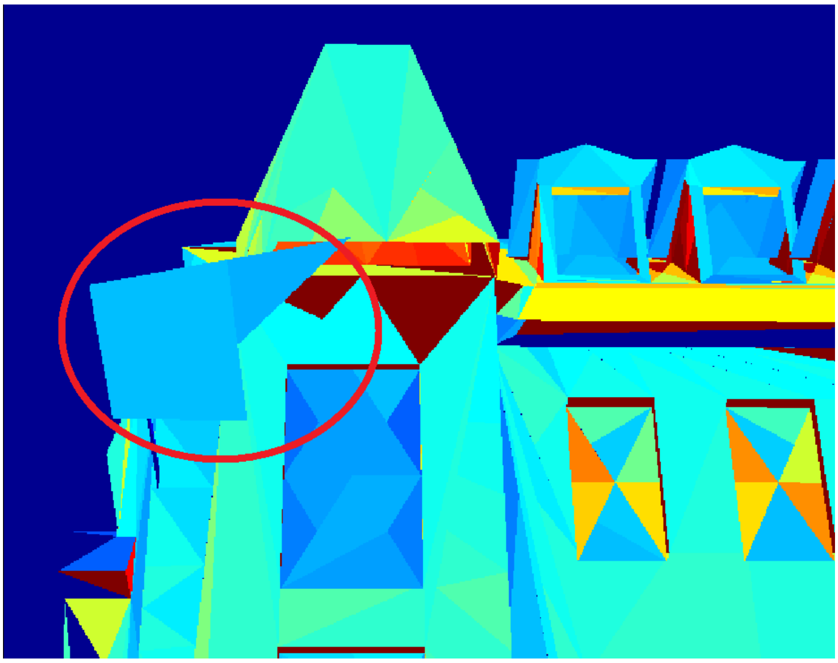

Figure 6.14: Triangles projected in a random order

If the triangles are drawn without sorting them first the result will be like shown in Figure 6.14. To prevent this from happening the triangles with the highest distance between their center point and the camera are drawn first, by doing so a so called z-buffer is created. This way closer triangles replace those drawn before it, which is how it should be. In the implementation the distance to the camera is only calculated for each triangle. This could cause some rendering issues since ordering the triangles does not guarantee that the right surface is shown. A vertex of one triangle might be in front of a second triangle, while the center point is further away. Therefore it would be better to determine the visible surface on a per pixel basis instead. However no occurrences of the issue are spotted, so it was decided that there is no need to implement this for the purpose of this project and to leave it as a recommendation. The result of a correctly rendered image is shown in Figure 6.15.

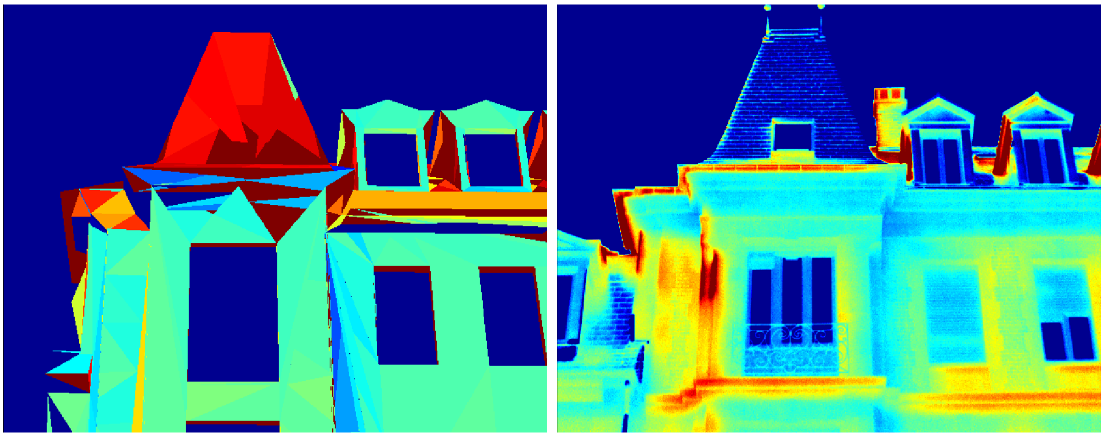

(A) Projected triangles from LASER/F (B) The corresponding thermal images

FIGURE 6.15: Results after projecting the triangles onto an image

6.6 Filtering

In Section 6.5 is discussed how the the 3D model is projected into the image domain. However both the thermal and the simulated images are not yet ready for the comparison. For instance the windows should not be considered in the comparison as is discussed in Section 6.2, but also fences, vegetation and neighbouring buildings should be removed simply because they do not belong to the facade of interest. In this section it is discussed how both images are prepared so that the results of the comparison are going to be valid and consistent.

6.6.1 Removal of the sky from the thermal images

Removing the sky from the images is a fairly straightforward process. A clear sky is characterised in the thermal images by a default minimum temperature of 223 K. Clouds do appear in the thermal images, but the temperature of the clouds, at least in the acquired dataset, is always significantly lower than the temperatures of the facades. Therefore the clouds can be filtered from the thermal images by applying a simple thermal threshold. Since clouds reflect the long-wave radiation from the buildings, the measured temperature of the clouds also varies during the day. This requires the thermal threshold to vary as well. In Figure 6.16 it can be seen how the sky (blue) is separated from the facade.

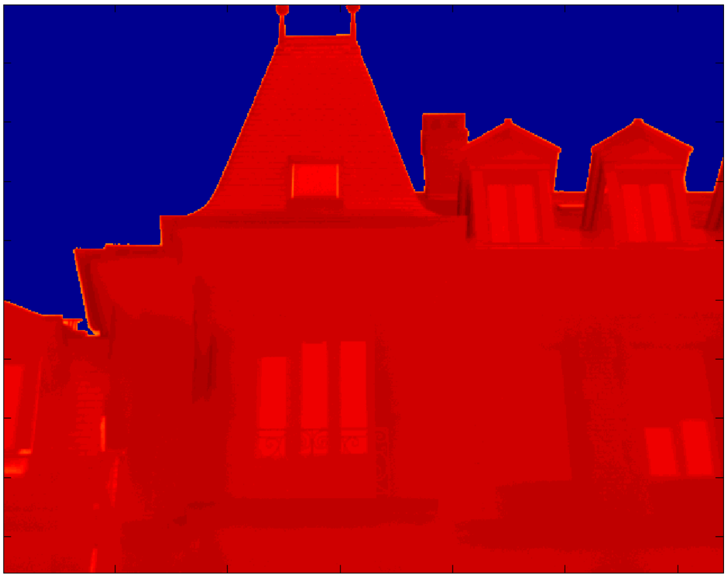

FIGURE 6.16: A thermal threshold is used to separate the sky

6.6.2 The problem of masking thermal images

The problem with vegetation in the thermal images is shown in Figure 6.17. The images are not taken with the exact same orientation, as such it is not possible to create one mask for the vegetation in the image domain and apply it to all images. One can manually identify all the vegetation (and other obstacles) in every image, but that would be an exhaustive process. There are several ways to filter out the vegetation. In general it is better to compare a smaller amount of correct data than a larger amount of more incorrect data.

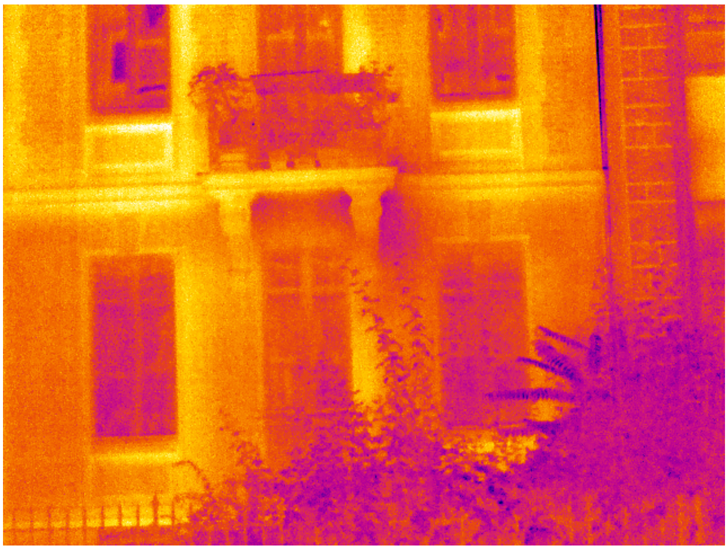

FIGURE 6.17: Relatively more complicated is filtering out vegetation from the thermal images

By analysing the thermal images, regions can be identified which are likely to not contain vegetation in any image from the series. For example one can only select the upper half of an image to use it for further processing. Another way would be to look for patterns with which vegetation can be detected. For example the presence of vegetation would give a lot of fluctuations in the thermal image. Sadly, there does not seem to be patterns like that which could be used to remove all the vegetation. An attempt could be made to check the results of a filling algorithm which gathers all neighbouring pixels which have approximately the same temperature.

These methods would be able to remove obstacles from the image, one more effective than the other, however none of them use the added information provided by the relation with the 3D model. The vegetation and buildings in the thermal images move, however in the 3D model they do not. By creating a mask in the 3D model and projecting it onto the thermal images, in a similar manner to how the triangles from the model were projected in Section 6.5, the mask is always at the right position in each of the thermal images. This method is implemented and the results can be seen in Figure 6.18.

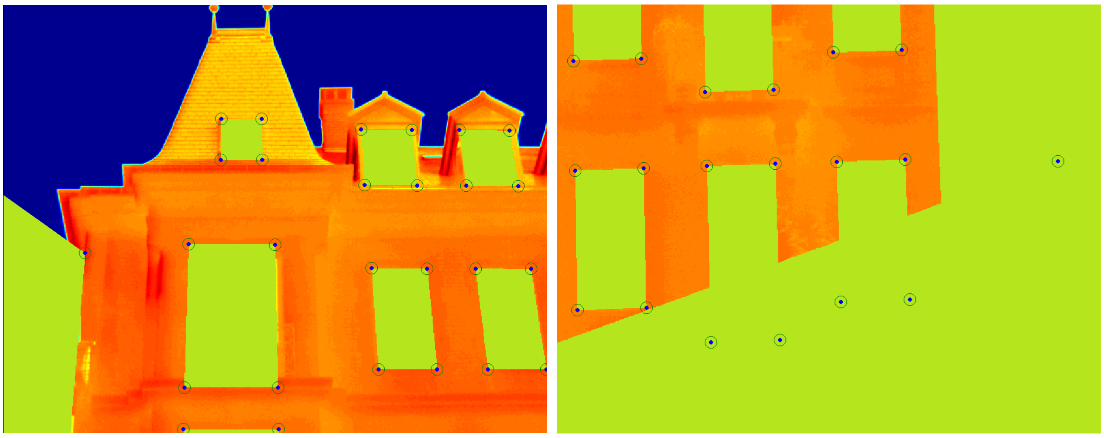

(A) Projected mask for vegetation and neighbouring building (B) Projected mask for the vegetation in Figure 6.17

FIGURE 6.18: Results after projecting the 3D masks onto the thermal images

6.6.3 Preparing for a fair comparison

The comparison between the measurements and the model should be as valid as possible. Ideally every pixel in the measured image should correspond to the one in the model image. Therefore the filters previously created for the thermal image are reused for the model image. The result of masking the model image can be seen in Figure 6.19. The images are however not yet geometrically identical, which is caused by the model not being an accurate model of reality, especially in the cases where no roofs are present. To make them identical, so every pixel with a value in one image also has a value in the other, the model image is also used as a mask for the thermal image.

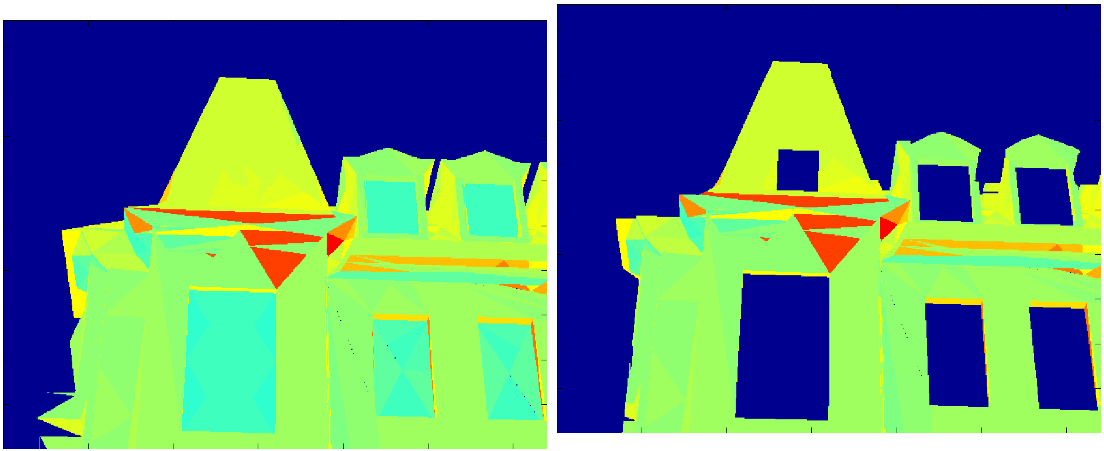

(A) The original unmasked simulated image

(B) The simulated image masked by the filtered thermal image

FIGURE 6.19: The filters are applied to the simulated image by copying the filter of the thermal image

The different simulation cases are characterized by their differences in geometry. Since the geometry differs also the triangles in the mesh differ. This generalization should however not influence the comparison between the geometry cases. The way this is implemented is by also applying the generalization to the thermal images. What this effectively means is that the thermal image is reconstructed by assigning the triangles from the generalization the average value of the pixels from the filtered image contained by set triangles. Triangles which are hidden only partly will have the average value of the whole triangle instead of only the visible part. The results are thermal images generalized in the same way as the model images are. An example can be found in Figure 6.20.

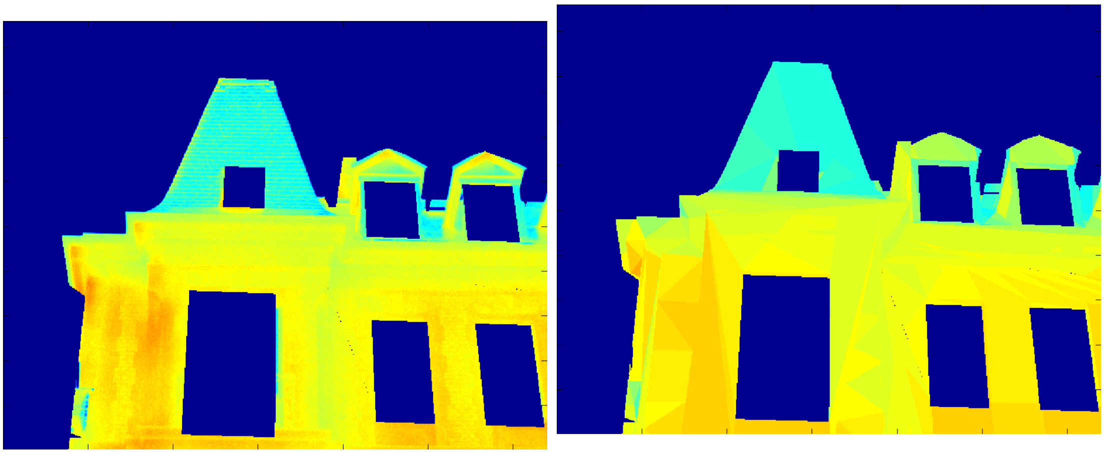

(A) The filtered thermal image

(B) The thermal image where values are averaged for each triangle

FIGURE 6.20: For a fair comparison the generalization is also applied to the thermal image

In the current implementation the mask is applied after the triangles have been projected. However there are also windows behind balconies, in those cases not the complete window is visible, yet the whole window is used as mask. To fix this issue the windows should therefore be sorted, based on distance to the camera, together with the model triangles. However, due to time constraints and the philosophy of at least making sure the data is accurate opposed to having as much data as possible, this is not implemented.

6.7 Evaluation methods

As discussed in Section 6.3 the comparison between the output of the LASER/F model and the measurements taken from the thermal camera is performed by comparing pairs of 2D exitance images. This approach allows more advanced comparison methods taking into account the statistics of the measured and simulated images. It is good to add that the comparison is made between different geometry complexity scenarios discussed in Section 5.2 for all the simulated and measurement images.

This section describes different methods of comparing these two sets of images and discusses each method's advantages and disadvantages. Finally, the selected method is presented in details.

6.7.1 Image window matching

The first option is *Image window matching.* When the geometry of the model is changed, at the same time the 3D positions of the surface points in the simulated images at which the exitance is modelled are changing. Therefore, point to point comparison of the simulated and measured images is a complex and time-consuming procedure. Bearing this in mind, the first solution that comes into mind is using image window matching. In this method, both the mean and the distribution of exitances in each window are meaningful statistics that can be used for the comparison. The idea is using identical windows in both simulated and measured images and define a test to quantitatively check the similarity of statistical behaviour of the two sets.

One of the best-known tests that can be a good criteria to compare the mean values is the t (t-student) test. There are various methods to calculate the t-test statistic depending on whether they only consider the means of the groups or also taking into account the variances, whether the group sizes are equal or not and also two groups follow a certain distribution. Based on the above-mentioned conditions, in our case t statistic is defined according to Equation 6.17.

$$t = \frac{\mu_1 - \mu_2}{\sqrt{\frac{s_1^2}{n_1} + \frac{s_2^2}{n_2}}}, \tag{6.17}$$

where μ_1 and μ_2 are the mean values , s_1 and s_2 are variances and n_1 and n_2 are the samples of measured and simulated exitance values in each window, respectively. It is noticeable that this formula is chosen because of the fact that the number of samples are not equal to each other as the model elements in simulated images are less than the measured pixels in each window. The null hypothesis of the test is that the two data sets consist of independent random samples following normal distribution with equal means and equal variances against the alternative that the means are not equal. The result of the test is either equal to 1 or 0 which indicates rejection or acceptance of the null hypothesis at a predefined significance level.

This method is implemented for different window sizes ranging from 100×100 to 2×2. Choosing an appropriate size of window is extremely critical since the distribution of samples in windows strongly depend on window sizes. For instance, in very large windows it is possible that data samples distributions differ from each other because various parts of the building facade with different materials are present.

Unfortunately, this approach fails in comparing the two sets of images due to two reasons. First there is an insufficient number of samples in the simulated windows. Since the simulated images are obtained from the projection of the 3D simulation model onto 2D images, the number of samples in these images are by far less than the number of samples in measurement images. Therefore, it is probable that in some of the comparison windows the number of samples in the simulated images are less than 30. This means that statistics such as mean and standard deviation are not appropriate statistics any more. For example, the standard deviation of the exitance values in image windows of simulated images are very close to 0 and this causes the t statistic to become very large leading to the rejection of the window in the test.

Secondly there is a non-similar distribution of measured and simulated data in the sampling windows. The *t test* is mostly applicable to two sets of samples that follow normal distribution. However, in our case the measured exitances in each window follows normal distribution while most of the simulated samples follow a distribution which is not normal. Therefore, *t test* will not be an appropriate statistical inference since for most of the image windows the initial condition of using the test is not met. The following figure illustrates the above-mentioned problem.

From Figure 6.21 it is apparent that the simulated samples are not normally distributed since a great number of samples only have one value of exitance. The important point here is that even changing the window size is not useful since the behaviour of the simulated samples in each window is not predictable. With above explanations it is inferred that using image windows and defining the *t test* to compare the results is not the best statistical analysis that can be done. Therefore, this method is rejected.

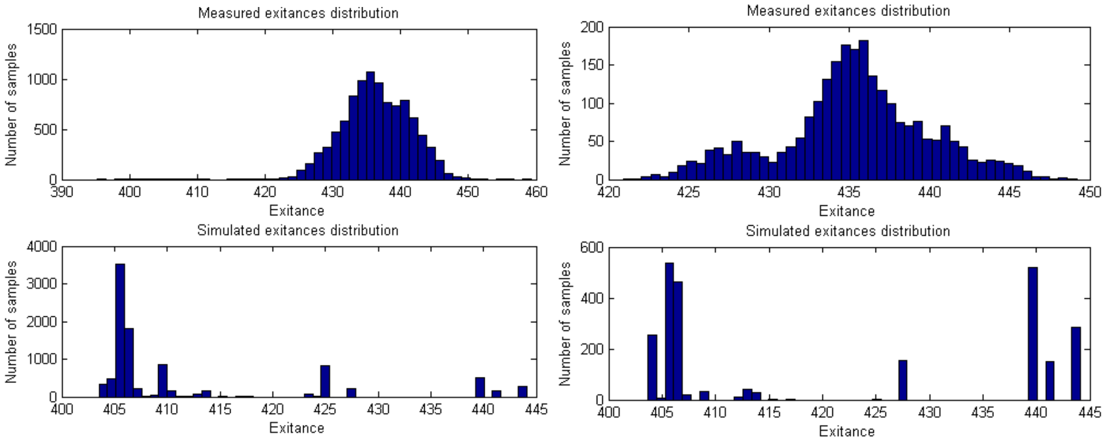

(A) 100 × 100 window size

(B) 50 × 50 window size

FIGURE 6.21: Distribution of measured and simulated images for two different window sizes

6.7.2 RMSE analysis based on differently sized windows

Another method to check how large the mean exitance values vary between the measured and simulated images is by calculating the RMSE. In this method, again the image windows are used to do the comparison but in a different way. This time two sizes of windows are defined. A big image window is defined similar to the previous approach and then it is subdivided to smaller windows. Defining smaller windows inside the big windows is mainly due to choosing homogeneous distribution of samples (i.e. samples from single part of the facade) and reduce the underlying noise. It is noticeable that the window sizes should be chosen in a way that they minimize the auto-correlation. After subdividing big windows, between each corresponding small window in simulated and measured images, the mean difference is calculated. Therefore, the RMSE of each big window is obtained by having the mean error values of each small window. Furthermore, for each paired images a single value of RMSE is obtained using the RMSE values of big windows. The same procedure can be done for all images in one epoch and then one value of RMSE can be calculated for the entire time step for each case of geometry complexity. Finally, the RMSE values can be plotted on a graph for the whole time steps and the comparison between each complexity scenario can be done based on the graph.

This approach is also rejected. The problem is that for instance in the most complex geometry case some parts of the facades consist of smaller triangles in comparison with the less complex cases. This issue affect the value of the calculated RMSE. Therefore, it is not wise to compare the RMSE values when they are not solely dependent on the value of the measured and simulated exitances.

The mentioned problem is the reason for changing the comparison strategy to a different one which is also based on RMSE analysis and will be discussed below.

6.7.3 RMSE analysis on generalized measurements

This method as is discussed in Section 6.5 is significantly different in comparison with the two previous methods since it includes changing the geometry of the measured images. This means for each case of geometry complexity of the simulated images, the measured images are generalized in the same way so that a pixel by pixel comparison can be made. This method also relies on calculating the RMSE values for each generalization scenario with the difference that these values are obtained in another way. In this approach, for each of the two considered buildings separately, all the measured exitance values for all epochs for each case of geometry complexity are stored in a vector. The same holds for the simulated images. Since the measured images are generalized and in terms of geometry they are exactly the same as the simulated images, each element in the measured vector is subtracted from the corresponding element in the simulated vector. Bearing this in mind, the RMSE value of each case of complexity through the entire time interval can be obtained using Equation 6.18.

$$RMSE(m,s) = \sqrt{\frac{\sum_{i=1}^{n}(m_i - s_i)^2}{n}}, \tag{6.18}$$

where m and s are the measured and simulated pixels respectively and n is the number of pixels in each vector which is the same for both datasets. These values can be calculated for each simulation scenario for all the epochs. This means that each case of geometry complexity has only one value of RMSE. Therefore, a very coarse comparison can be made between each case based on the corresponding RMSE values.

Another benefit of generalizing the measurements and doing a pixel by pixel comparison is that the temporal graph of exitance RMSE values for each simulation scenario can be drawn. This graph is very descriptive in terms of showing how the RMSE values behave over 24 hours. Also from these graphs it can be inferred that at what specific epochs the model is working more accurate and the differences between measurements and simulations are less.

6.7.4 Other possible tests and conclusion on methodology

Besides comparing the RMSE values, the error vectors can also be investigated. The error vector of each complexity scenario consists of the differences between corresponding pixel values of the measured and simulated vectors and they describe how well the model fits the measurements in each simulation scenario. The histogram of these vectors should follow Gaussian distribution with zero mean. This comparison can tell more about the precision of the model in different epochs, since the standard deviation of residual vectors can be estimated using the histograms . In this way an appropriate statistical inference along with comparing the RMSE values can be done.

RMSE analysis on generalized measurements and using residual distribution analysis seems to be the best option for making the comparison between each case of geometry complexity since it includes both numerically and statistically analysis of measured and simulated images. Also, by generalizing the measurements according to simulations we minimize any error in calculating RMSE values which is a certain benefit comparing to the other two approaches.

Chapter 7

Sensitivity test results

This chapter describes the effect of different geometry complexity scenarios implemented in LASER/F model and compares the results with the measurements taken from the thermal camera based on the approved method discussed in Section 6.7. This section is organized as follows.

Firstly, a coarse comparison of RMSE values among each simulation scenario over all epochs is made in Section 7.1. Later, in Section 7.2 and Section 7.3, a more detailed comparison is performed by interpreting the temporal exitance RMSE graphs and residual distributions for each building of interest separately . Finally, the probable shortcomings of the LASER/F model are explained in Section 7.4.

7.1 Coarse comparison of RMSE values

Table 7.1 shows the RMSE values calculated for each scenario of geometry complexity over the entire time step for buildings 1 and 4 Rue de l'Argonne. The first thing that can be concluded from the table is that the values of RMSEs for the two buildings are quite large, which is caused by a large difference between the measured and simulated radiant exitances for all cases.

For building 1, the most accurate result is occurred for the base case + balconies since the RMSE value is smaller compared to other cases. The highest RMSE values are in the base case + windows. For building 4 the same statement stands with the difference that the RMSE values are higher overall compared to building 1.

The hypothesis was that the complex case should have the lowest RMSE value for both buildings, since it best represents the actual facade. However, the results indicate otherwise.

Table 7.1 also shows the required simulation times for each scenario. It is speculated that geometric detail increases the simulation time, since there will be more triangular meshes introduced in the model. The simulation time for the complex case is almost 9 times longer than for the base case while the complex case is only slightly more accurate

Simulation scenario	**RMSE building 1**	**RMSE building 4**	**Simulation time**
Base case	45.84 W m^{-2}	48.85 W m^{-2}	7 h 33 min
Base case + simple roofs	46.30 W m^{-2}	44.25 W m^{-2}	10 h 8 min
Base case + complex roofs	42.85 W m^{-2}	44.59 W m^{-2}	10 h 11 min
Base case + windows	46.93 W m^{-2}	51.29 W m^{-2}	15 h 56 min
Base case + balconies	36.87 W m^{-2}	43.39 W m^{-2}	19 h 1 min
Complex case	40.75 W m^{-2}	44.59 W m^{-2}	46 h 12 min
Complex case + vertex welding	44.68 W m^{-2}	45.52 W m^{-2}	18 h 58 min

Table 7.1: Overview of simulation time and radiant exitance of all simulation scenarios over all epochs

than the base case. This particularlity might be because LASER/F may be incorrectly computing the radiant exitances, especially at finer levels of detail where scaling effects might be present. However, this method is just a coarse comparison between the RMSE values. A more in-depth comparison method is discussed in Section 7.2.

7.2 Comparison based on temporal RMSE exitance graphs

A more descriptive method to compare the results is by comparing the temporal exitance RMSE graphs for each of the buildings separately. Figure 7.1 and Figure 7.2 shows the graphs for building 1 and 4 Rue de l'Argonne respectively.

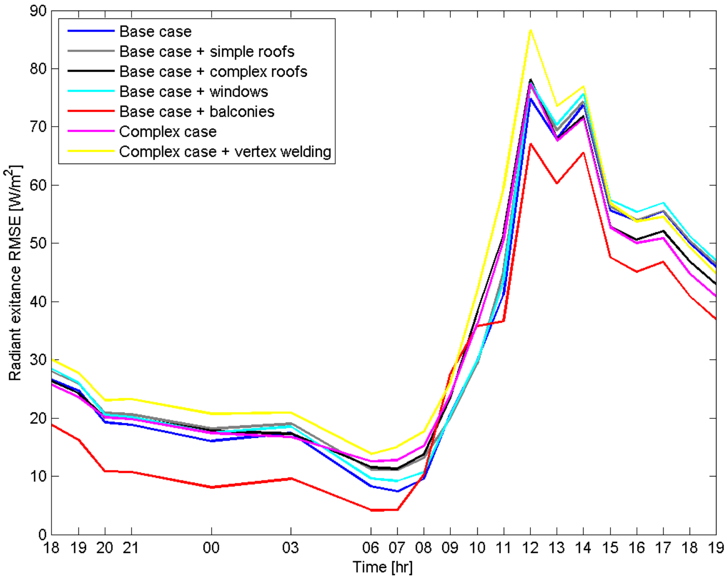

Figure 7.1: Temporal exitance RMSE for building 1 Rue de l'Argonne

Temporal exitance RMSE for building 1 Rue de l'Argonne

As can be seen in Figure 7.1, the overall trend of RMSE values for building 1 is the same for all the different geometry complexity cases. However, the range that these values differ are different between each case. The lowest RMSE values occur for base case + balconies which ranges from approximately4 W m^{-2} to 65 W m^{-2} while the largest RMSE

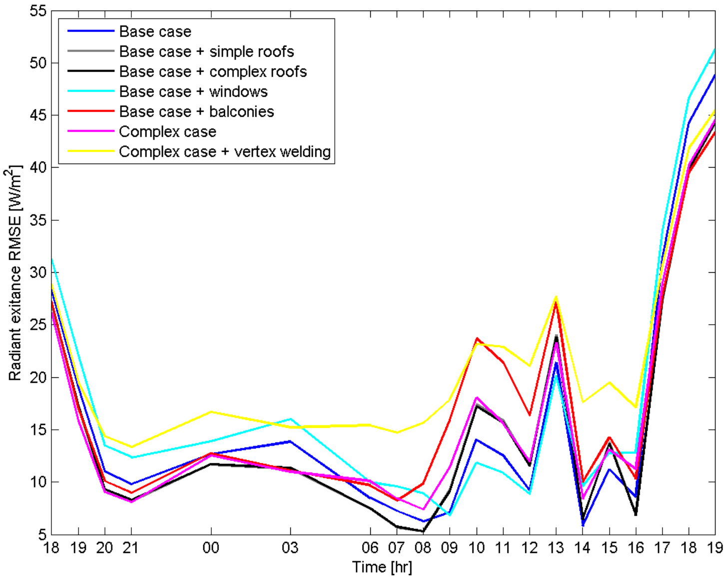

Figure 7.2: Temporal exitance RMSE for building 4 Rue de l'Argonne

values are for the complex case derived from vertex welding($16\,\mathrm{W\,m^{-2}}$ to approximately $85\,\mathrm{W\,m^{-2}}$). The diurnal difference between these two cases is large. This suggests that the balconies have a significant effect on the accuracy of the simulation and should be modelled.

It can also be inferred that the performance of LASER/F is best during the night and early morning when the ambient temperature is lowest. The performance degrades from this point as the air temperature rises throughout the day until noon when the surface temperature is higher (due to direct and diffuse solar radiation). This is not surprising because when the irradiance of the surfaces increases, the RMSE values will also increase. More importantly, this comparison shows that some geometry scenarios do not show significant difference in RMSE values between each other even though their complexities are. This is true for the base case, base case + simple roofs, base case + complex roofs and the complex case, during the warming period (from 8:00 to 12:00). This may imply that the model is not sensitive to level of details in geometry of buildings in warming periods (sunrise to sunset), but does have an effect in cooling periods (sunset to sunrise).

Temporal exitance RMSE for building 4 Rue de l'Argonne

Figure 7.2 illustrates the temporal exitance RMSE values for building 4 Rue de l'Argonne. The RMSE values for exitance vary from 5 to approximately $52\,\mathrm{W\,m^{-2}}$ in total, which compared to building 1 consists of smaller RMSE values. Again, all the trends are similar to each other but very different from building 1. This is probably because building 4 was exposed to direct solar radiation much later than building 1 (in the afternoon, during sunset). In other words, the effect of morning shadow caused the trend to be very different. For this building, the higher RMSE values are for the complex case derived from vertex welding while the lower values are for the base case + complex roofs.

Similar to Figure 7.1 the model performed better during the cooling period (night and early morning). However, different from building 1, the RMSE values increase steeply until they reach their highest value at 19:00 which was around sunset. In terms of geometry complexity, the results are completely different from what is expected since the values of RMSE are not lower for more complex geometry scenarios. For instance, the RMSE values of the base case + simple roofs is approximately identical to the base case + complex roofs and the complex case. So for building 1, the roof geometry detail did not have a significant impact on accuracy of the LASER/F accuracy.

Furthermore, the results from building 1 and 4 Rue de l'Argonne suggest that there may be a systematic error introduced in LASER/F. However, this cannot be deduced by simply comparing the RMSE values. This is where a statistical analysis based on the error vectors become more essential. The next section will elaborate more on this approach.

7.3 Distribution analysis of error vectors

As discussed in Section 7.2 the comparison of RMSE values is a good method to illustrate the differences in the results, however it does not provide any indication about the error distribution between the simulation and measurements. By interpreting the error distributions of some of the geometry scenarios, two important matters can be investigated:

1. If a systematic error is introduced in the model that causes the RMSE values to be large.
2. Statements about the precision of the model in a specific epoch can be given.

To illustrate, in Figure 7.3, the residuals histogram of the base case, complex case and base case + balconies for building 1 are presented.

It is important to note that the error vectors for other cases are similarly distributed which leads to a very important result. The residual histograms show that they are not normally distributed around the mean of 0. This implies that all the measured exitance values are higher than the simulation values. The causes of this systematic error are described in Section 7.4.

As aforementioned, the precision of the model at a specific epoch can be estimated from the residual histogram of each geometry scenario, since the standard deviation and the mean of the error vectors can be derived from the histogram. Here, only the base case + balconies are discussed to show a possible histogram output. The residual

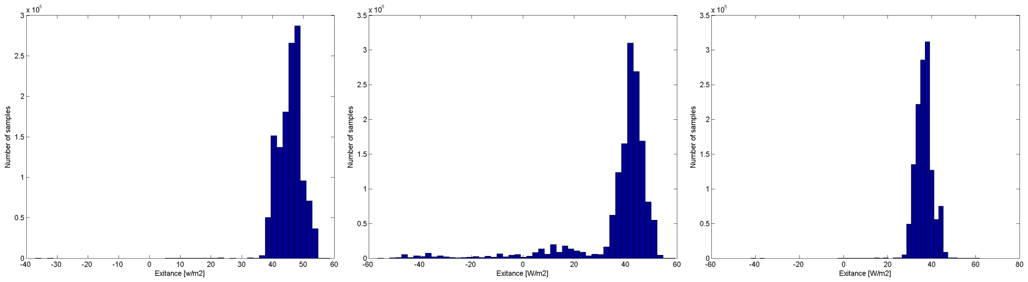

(A) Error distribution of Base case (B) Error distribution of Complex case (C) Error distribution of Base case + balconies

FIGURE 7.3: Residual histograms for 3 different scenarios of Building 1 Rue de l'Argonne

histograms for building 1 Rue de l'Argonne at 6:00 in the morning and 12:00 in noon can be seen in the next page.

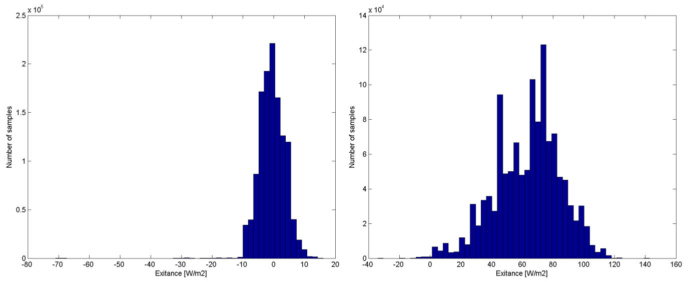

(A) Exitance residuals at 06:00 am (B) Exitance residuals at 12:00 pm

FIGURE 7.4: Residual histograms of Base case + balconies at 2 different epochs for building 1 Rue de l'Argonne

According to Figure 7.1 the lowest value of RMSE occurred at 6:00 am while the worst case happened at 12:00 pm. The standard deviation of this case at 6:00 is equal to 4.12 which is quite smaller than 21.25 which occurs at 12:00. This confirms the results from the Figure 7.1 that the model works more precise in the early morning rather than at noon but it is also gives the exact value of precision which is equal to the standard deviation.

7.4 LASER/F simulation shortcomings

Section 7.3 mentioned that there is a systematic error introduced in the LASER/F model probably due to the fact that the measured exitances are consistently higher than the simulated ones. The magnitude of the differences can be seen in a graph of the mean radiant exitance values of measured and different simulated scenarios throughout the whole time interval (Figure 7.5 and Figure 7.6 for building 1 and 4 respectively).

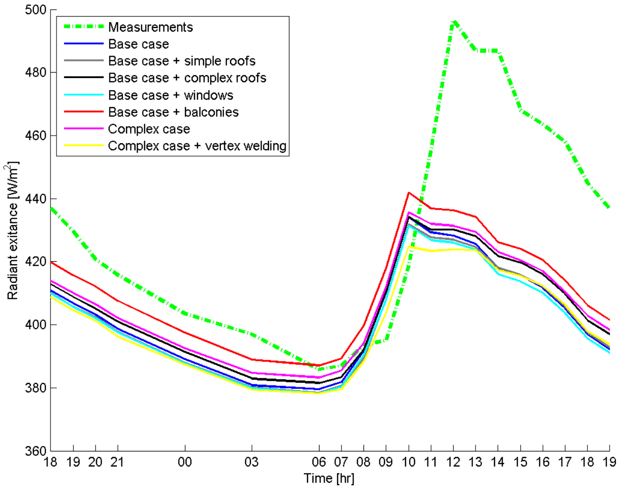

FIGURE 7.5: Mean radiant exitance of measurements and simulation scenarios for building 1 Rue de l'Argonne

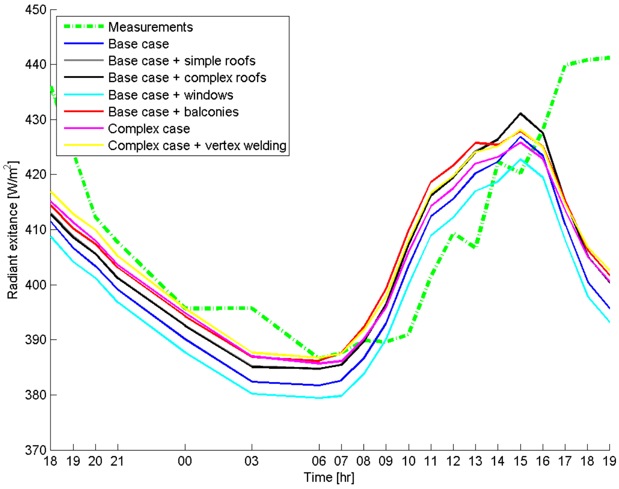

FIGURE 7.6: Mean radiant exitance of measurements and simulation scenarios for building 4 Rue de l'Argonne

It can be clearly seen in Figure 7.5 that the measurements have higher values of mean radiant exitance compared to the simulated ones. Thus, it can be deduced that surface temperatures simulated for each case of geometry complexity is lower than the measured surface temperatures. When it is converted to exitance values, the difference becomes even higher. This is one of the main reasons that the absolute accuracy of the model is low. In other words, the RMSE values are large due to a systematic error introduced by the model. This issue might be caused by several issues:

- *Material properties* - It is probable that thermal properties of the materials used for the buildings are incorrectly assigned or imprecise.

- *Parametrization of surface-air heat exchange* - This causes the sensible heat flux to be overestimated and will systematically lead to lower simulated diurnal surface temperatures.
- *Vertical wind profile* - Wind has an important role in cooling the canyon. The logarithmic vertical wind profile used in LASER/F model may be over-simplistic (see Chapter 8).
- *Modelling of building volumes* - Since the geometric input to the LASER/F model is deduced from the CAD model (which is created using photogrammetry), the volumes of all the buildings in the canyon are not accurately modelled. As a consequence the internal heat storage of as well as the heat inertia of the buildings is lower, causing the radiative fluxes in the canyon to be lower as well.

Chapter 8

Vertical wind profile assessment

Next to testing the sensitivity of the LASER/F model to 3D geometry complexity, it is also interesting to provide a critical view on the parametrization of air transport through the canyon used in LASER/F. This part of the project focuses on determining whether this assumed profile can explain some of the results from the geometric complexity impact tests. The widely used 1-dimensional logarithmic vertical wind profile as is implemented in LASER/F is based on Masson [49] and is compared to the outcomes of turbulent wind flow simulations using a CFD model from TU Delft (Transport Phenomena group).

Section 8.1 gives a brief background to the subject of CFD modeling in general and the model which is used. With these basics one can proceed with the actual methodology that is used to perform the CFD simulations in Section 8.2, followed by the output generation and extraction of the requested wind profiles in Section 8.3. The chapter is concluded with an assessment of the results and the comparison with the LASER/F assumptions which is found in Section 8.4. The work flow for this chapter can be found in Appendix E.

8.1 CFD model

The model that is used to make the critical assessment of the vertical wind profile in LASER/F is the CFD model developed by the TU Delft Transport Phenomena group. For this research project, it is possible to use simple geometry of the canyon to parametrize the vertical wind profile.

8.1.1 TU Delft CFD model

Typically, a CFD model is used to simulate the turbulent flow of fluids over time through a defined space [24]. In this case, it is used to simulate the turbulence of air through the canyon, and in particular, to extract a vertical wind profile through the cross-section of the canyon with buildings of interest (1 and 4 Rue de l'Argonne).

The advantage of using a CFD model to compute a 3D velocity field is the relative ease and precision that can be achieved compared to doing wind tunnel tests that are labour intensive. CFD models discretize the model space into fine grid cells wherein a solution is computed so many configurations can be tried virtually. The resolution of the grid cells is controlled by the user and in the TU Delft model can be very fine at the surfaces of the obstacles to very coarse at the edges of the experimental bounds. This is to save some simulation time, since solutions at the boundary of the simulated grid are more homogeneous. A constant cell expansion factor is used to govern the increase in cell size over the whole grid. As the number of grid cells affect computation time, finding a good ratio is important.

A CFD model finds numerical solutions for fluid turbulence using the physical laws of conservation of mass (Equation 8.1) and momentum (Equation 8.2)

$$\frac{\partial u_i}{\partial x_i} = 0 \tag{8.1}$$

$$\frac{\partial u_i}{\partial t} + u_j \frac{\partial u_i}{\partial x_j} = f_i - \frac{1}{\rho}\frac{\partial p}{\partial x_i} + \nu \frac{\partial^2 u_i}{\partial x_j \partial x_j} \tag{8.2}$$

Coupled with this can be numerical calculations for the concentration of pollutants and temperature as these are properties that are transported by the medium of air. The motion of fluid over time is described by the Navier-Stokes equations in x, y and z direction [24, 50]. It takes into consideration fluid viscosity and pressure and gives a solution as a velocity field (of the fluid). Thus, fluid viscosity parameters must also be set to determine the shear stresses (or inertia) on fluid. The time term is fixed in order to create a steady state solution while the pressure term is solved iteratively for each grid cell [50].

The initial boundary conditions must be defined in order to set the environmental space within which the model should run. Setting inadequate boundary conditions could force the model to give unrealistic solutions. For example, if the simulation space is too small compared to the fluid obstacles, the turbulent wake might not have enough space to stabilize.

Given the Navier-Stokes equations to describe fluid motion, turbulence is solved in the TU Delft CFD model by using the Reynolds Averaged Navier-Stokes (RANS) equations (Equation 8.3). The RANS approach is an approximation approach that models all turbulent motion using the mean values of the fluctuating variables (fluctuating over time).

$$\frac{\partial u_i}{\partial t} + \frac{\partial u_i u_j}{\partial x_j} = \frac{\partial}{\partial x_j}\left[\mu\left(\frac{\partial u_i}{\partial x_j} + \frac{\partial u_j}{\partial x_i}\right) - \overline{u_i' u_j'}\right] \tag{8.3a}$$

$$\overline{u_i'u_j'} = \frac{2}{3}K\delta_{ij} - 2\mu_t S_{ij} \tag{8.3b}$$

In these equations μ represents eddy viscosity, K the turbulent kinetic energy, and S the fluid strain.

The Reynolds stress term is computed using a 'turbulent viscosity' Equation 8.3b, which itself is computed using the k-e model (Equation 8.4).

$$\frac{\partial \rho k}{\partial t} + \frac{\partial(\rho U_j k)}{\partial x_j} = \frac{\partial}{\partial x_j}[(\mu + \frac{\mu_t}{\sigma_k})\frac{\partial k}{\partial x_j}] + P_k + P_b - \rho\epsilon - Ym + Sk \tag{8.4a}$$

$$\frac{\partial \rho\epsilon}{\partial t} + \frac{\partial(\rho U_j \epsilon)}{\partial x_j} = \frac{\partial}{\partial x_j}[(\mu + \frac{\mu_t}{\sigma_\epsilon})\frac{\partial \epsilon}{\partial x_j}] + C_{\epsilon 1}\frac{\epsilon}{k}(P_k + C_{\epsilon 3}P_b) + C_{\epsilon 2\rho}\frac{\epsilon^2}{k} + S_\epsilon \tag{8.4b}$$

The k-e model describes the dissipation of kinetic energy k. In other words, the Reynolds number describes the amount of fluid stress that leads to the fluctuations in turbulence.

8.1.2 Profile comparison

Even without the incorporation of thermal equations to the CFD model, the simulation elucidates the expected behaviour, or pattern, of wind motion through the canyon and can indicate where the cooling effect of wind can be expected, or where there might be a concentration of pollutants. In LASER/F, the assumed vertical wind profile is exponential and without consideration of the frictional forces of the canyon surfaces. Furthermore, the profile is uniform throughout the canyon. That is, a vertical cross-section of anywhere in the canyon would show the same vertical wind profile. Based on many studies of wind profiles using CFD modelling, results indicate that this exponential behaviour of vertical wind speed is not realistic (see also Chapter 2).

8.2 Simulation methodology

This section elaborates on the CFD simulation methodology. The input needed to perform CFD-simulations is explained in Subsection 8.2.1 whereas the actual use of the model to ensure a valid output that is discussed in Subsection 8.2.2.

8.2.1 Input for the CFD-model

Two different external sets of parameters are needed to perform the CFD simulations, i.e. geometry and meteorological information. The geometry is built from a text file with manual extracted coordinates from the 3D AutoCAD model. Objects can only be defined by entering four coordinates: x_{min} x_{max} y_{min} y_{max}. So, every complex building has to be converted to a set of adjacent rectangles. When importing this file into the CFD model, the coordinates have to be transformed. This is needed to undo the mirroring of the buildings along the x-axis through the middle of the canyon and to make sure the canyon is facing north correctly. This incorrect import has to do with the different conventions that AutoCAD and the turbulent wind model have.

The wind conditions are taken from the meteorological data, acquired by the meteorological station as described in Section 5.4. The two parameters needed to perform the simulations are the wind speed and the prevailing wind direction. The input data used for the simulations are taken at September 15^{th}, 15:00, where the wind speed is $2.25\,\mathrm{m\,s^{-1}}$ and wind direction is 33.67°. The time is chosen because it is near the high temperature peak of the day, which coincides with the time with the most turbulent fluxes. This creates the most interesting vertical wind profile in the canyon.

8.2.2 Use of the CFD-model

The overall geometry of the canyon used in these simulations is the same as is used for the LASER/F simulations. However, only the closed case is considered. The closure consists of one building block on the north-east side of the canyon and two blocks at the south-west side. All three building blocks have a 20 m height. With this closure, the flow in the canyon can be modelled more realistically.

The CFD model requires space in front of the building and behind it to ensure the flow is built up correctly and to make sure that the exit flow is stable again. Next to this geometry dependent plane size, other parameters that are set for this simulation (which significantly influence the final outcome of the simulation) are:

- Number of iterations: 1500
- Grid cell size: 1
- Cell expansion factor: 1.25
- Maximum cell size: 10

The larger the number of iterations entered, the more precise the output of the simulations will be. After the initial 100-500 iterations the outcome will already fluctuate around the true solution, but 1500 iterations are done to ensure stability. Every surface is divided into two grid cells at minimum. Regarding the input geometry, the minimum grid cell size is set at 1. The space is divided into cells that grow efficiently to a maximum cell size of 10 where less precision is needed. This expansion is set by the cell expansion factor. Both the 3D geometry model and the grid can be seen in Figure 8.1.

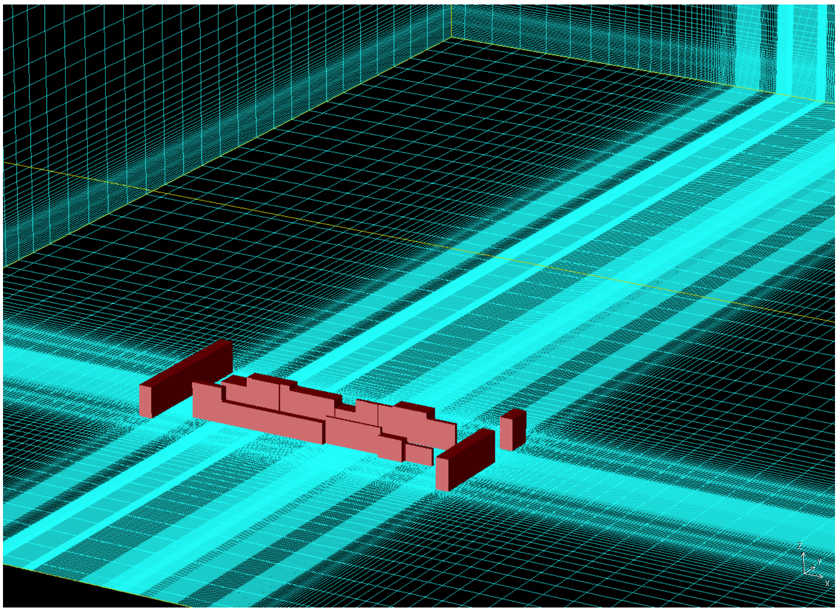

Figure 8.1: The 3D geometry model and the division of grid cells across the model space

8.3 Processing output

After performing the simulations, the output has to be post-processed to extract the wind profile needed for the comparison between the CFD model and the wind profile used in the LASER/F-model. The different outputs per grid cell are displayed in the following list:

- Wind speed
- Turbulent Kinetic Energy (TKE)
- Dissipation of TKE
- Air temperature

The output of the CFD model is not directly accessible. It can be visualized using OpenDX (free visualization program). In this program there is a possibility to extract horizontal line profiles. The position of the line on the x-axis can be entered, as well as the length of the line. In this case, the horizontal profiles are extracted at different heights (1, 2, 3, ..., 27 m above ground level) at a point between the two buildings of interest, see Figure 8.2.

For every height step, the value of horizontal wind speed is taken at this point and plotted against the corresponding height. One profile with a fixed x, y-position in the canyon is taken to qualify the wind profile used in LASER/F, see Section 8.4 for this comparison. The CFD model returns a horizontal wind speed in x- and y-direction.

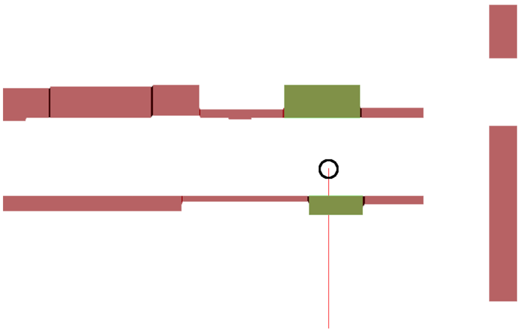

FIGURE 8.2: Extraction point in urban canyon between buildings of interest. 4 Rue de l'Argonne is displayed at the top and 1 Rue de l'Argonne below (both in green)

These can be combined to give the wind speed in the horizontal (xy) plane. All three are displayed in Figure 8.3.

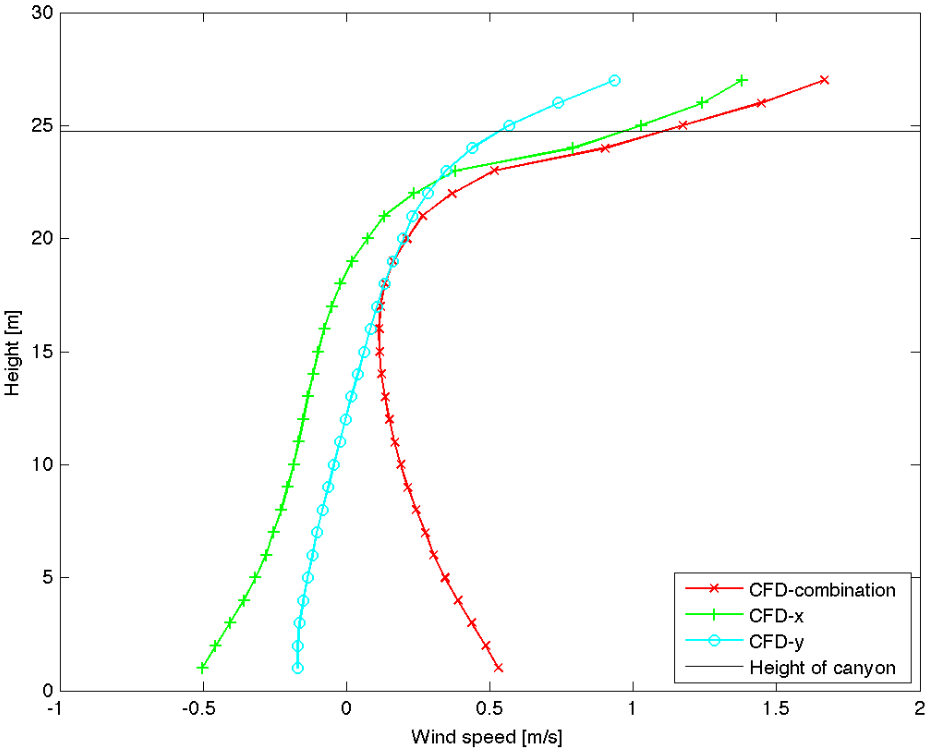

FIGURE 8.3: The vertical profiles of horizontal wind speeds in x- and y-direction are displayed, together with a combined (x,y) profile of the horizontal wind speeds

The horizontal wind speeds in x- and y-direction can also be visualized with OpenDX. Particularly interesting visualizations are the wake fields that are present in the urban canyon. In Figure 8.4 these wake areas can be seen. Also two isoline-figures are presented where one can see the flow in x- and y-direction at half height of the canyon. The wake areas are related to the turbulent kinetic energy ($m^2 s^{-2}$) displayed in Figure 8.5. This is the most important parameter when qualifying CFD simulations. Due to the fact that in this research only vertical wind profiles are compared to each other, the turbulent kinetic energy will solely serve as an indication of the severity of turbulence in the urban canyon.

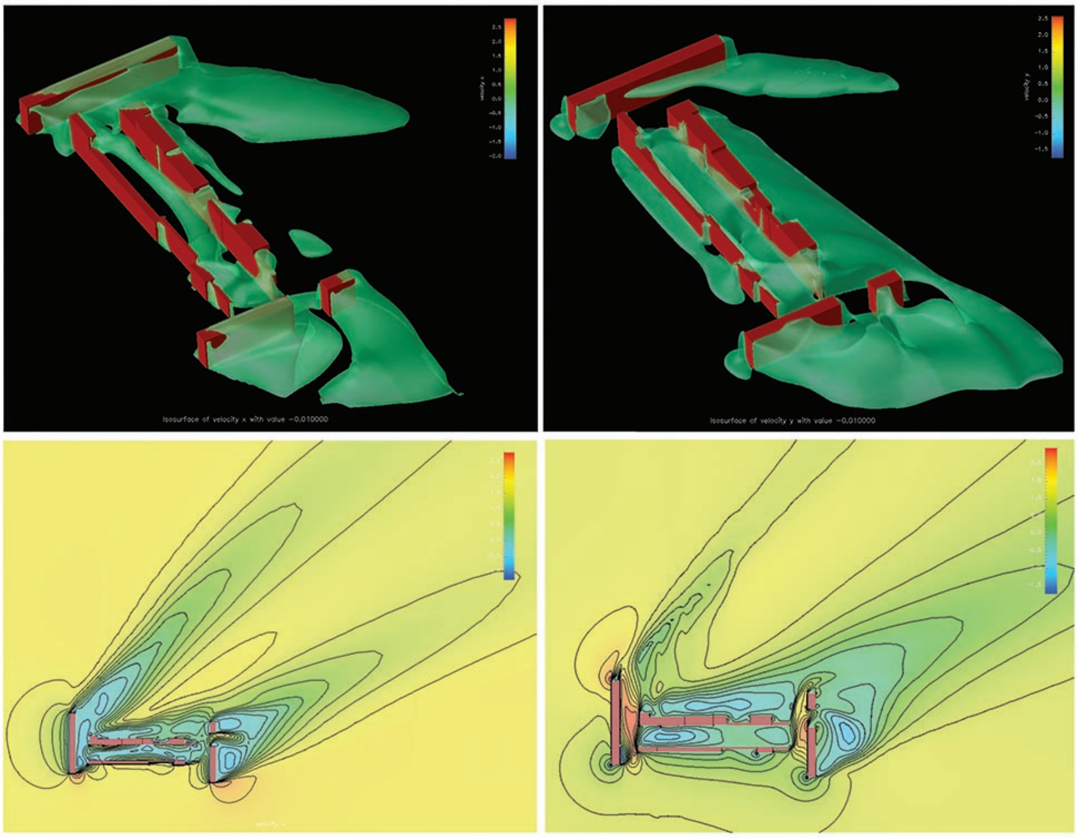

FIGURE 8.4: Top left: x-velocity wake areas. Top right: y-velocity wake areas. Bottom left: x-velocity iso lines at half height of the canyon. Bottom right: y-velocity iso lines at half height of the canyon

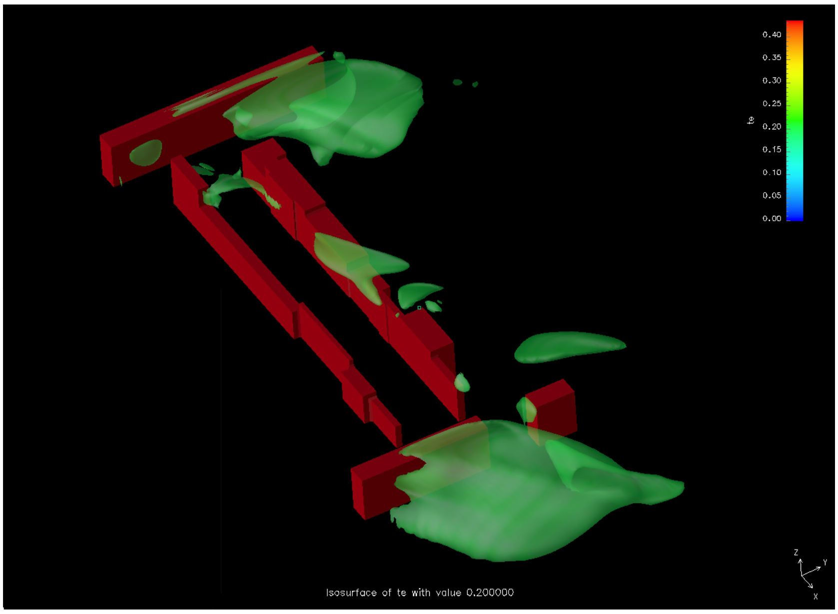

FIGURE 8.5: Turbulent wind flow showed by the amount of kinetic energy (isosurface = 0.2)

8.4 Assessment of the results

The vertical wind profile from the CFD model is extracted at one moment in time and at one place in the canyon. The vertical profile used in LASER/F is based on a parametrization that Masson [49] describes, see Equation 8.5:

$$U_{can} = \frac{2}{\pi} exp(-\frac{1}{4}\frac{h}{w}) \frac{ln(\frac{h/3}{z0_{town}})}{ln(\frac{\Delta z + h/3}{z0_{town}})} |U_a| \tag{8.5}$$

Here, h is the maximum height of the tallest building in the canyon, h/w the aspect ratio of the canyon, with a width w of 20 m. U_a is the wind speed at the first atmospheric model level, $\Delta z = 3$ above the canyon. This level is taken as the top of the urban canopy layer $h + \Delta z$. $z0_{town}$ is defined as the rugosity (or roughness) of the town. In Masson [49], a value of $h/10$ is taken as approximation for this parameter. Wind speeds can be determined by varying the $h/3$ fraction. In this example case, $h/3$ is the position 1/3 from the top of the canyon, thus 2/3 from the ground.

As can be seen, the profile that is used in LASER/F is 1-dimensional. It only gives the horizontal wind speed in one direction, namely the direction of the wind as defined in the forcing conditions, e.g. the horizontal wind speeds are independent of the wind direction. This limits the comparisons that can be made with the outcomes of the CFD simulations.

The angle of incidence of the wind is in this case almost the same for the CFD model and the LASER/F model when one only takes the profile in x-direction of the CFD simulations. Thus, the vertical wind profile of the horizontal wind speeds in x-direction can be compared with the 1-dimensional parametrization. This can be seen in Figure 8.6. With a wind speed of 2.25 $\mathrm{m\,s^{-1}}$ at the top of the canyon, there are differences in the canyon ranging between 0.5-1.0 $\mathrm{m\,s^{-1}}$. These are significant deviations.

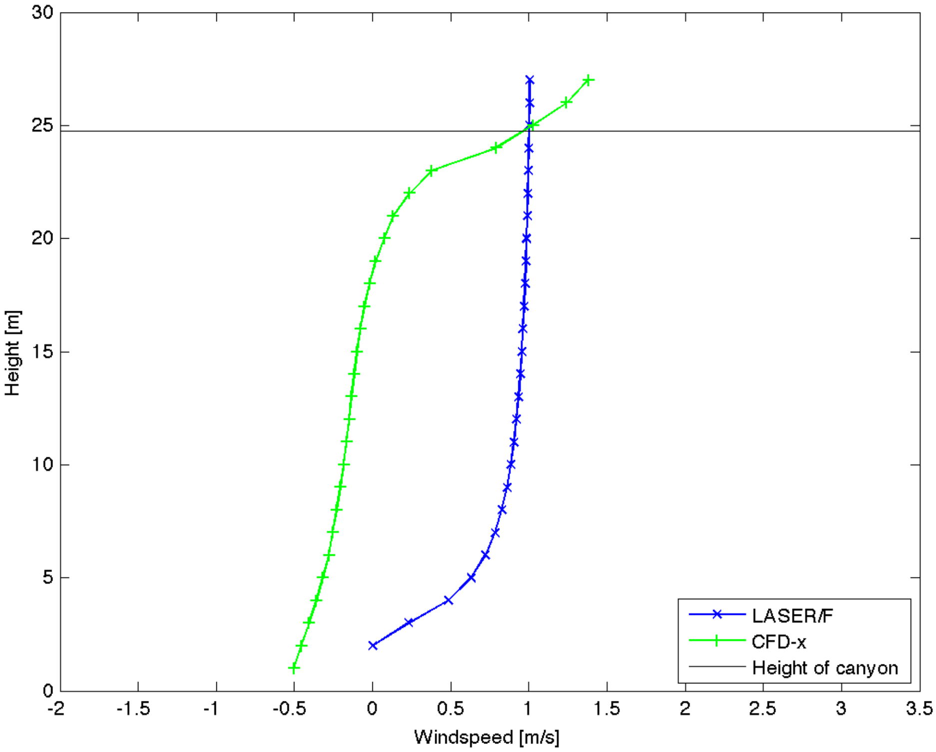

FIGURE 8.6: The vertical profile of horizontal wind speeds in x-direction as extracted from the CFD-model compared with the parameterization from LASER/F

The values retrieved from the LASER/F parametrization are positive only. The height from where the calculations of the horizontal wind speeds are valid is dependent on $z0_{town}$. In the blue, LASER/F, line one can clearly recognize a profile where the wind builds up from the ground, a boundary layer. The profile extracted from the CFD model has an almost straight path, so constant horizontal wind speed values, within the canyon. This is caused by the mixing of air by the buildings. At the top, the geometry is of less influence. Here one can see the start of a boundary layer. Note that the exponential profile used in LASER/F will be replaced by a logarithmic profile for any layer above the canyon.

The combined xy-profile gives a more realistic insight in the wind speeds in the horizontal plane than only the horizontal wind speeds in x-direction. Therefore the combination is plotted against the 1-dimensional LASER/F-profile in Figure 8.7. However, the differences are of the same order of magnitude as the differences in the previous comparison (CFD-x and LASER/F. A value of 0.5 $\mathrm{m\,s^{-1}}$ difference in horizontal wind speeds is very large. This causes considerable deviations in the transport of heat through the canyon, what results in lower surface temperatures in the LASER/F model.

It should be noted that the combination of the two vectors (x and y) hides the direction of the wind flow. To find these directions, one has to check the original profiles in Figure 8.3.

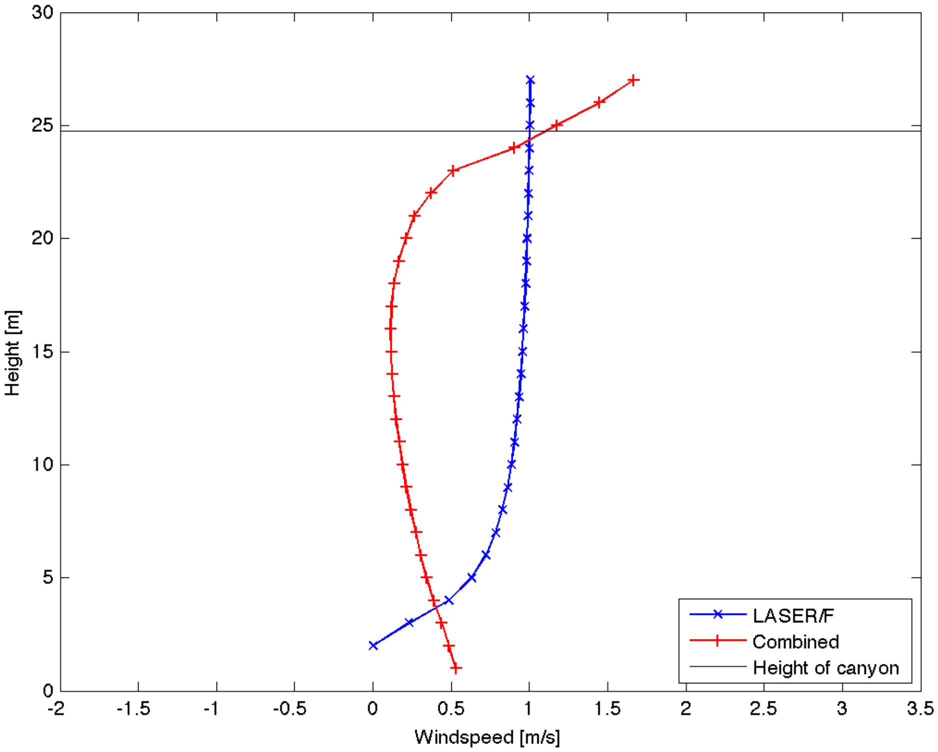

FIGURE 8.7: The combined (x,y) profile of the horizontal wind speeds as extracted from the CFD-model compared with the parameterization from LASER/F

8.5 Further CFD studies

This CFD-part of the research project is a first assessment to consider further investigation on this topic. Some interesting conclusions can be drawn, which are first mentioned in Section 8.4. However, since this is merely an explorative study - to determine the usefulness of continuing investigations of possible improvements of the parameterization used in LASER/F - many recommendations can be made. These will surely improve the validity of the statements listed in the two subsections below; Subsection 8.5.1 and Subsection 8.5.2.

8.5.1 Conclusions

With the overview of the outcomes and their meaning presented in Section 8.4, this subsection can be short and is solely meant to give the reader the opportunity to grasp the essence of the results. These are listed below.

- The horizontal wind speeds are generally more than $0.5\,\mathrm{m\,s^{-1}}$ off for the majority of the measurement points in the canyon. They are all exaggerated, which means that the wind blows harder than the CFD model indicates. This causes more transport of heat by air, which results in lower surface temperatures.
- Based on literature one can assume that the parametrization is incorrect near all surfaces due to boundary layer issues. One cannot assume that the vertical wind profile in the middle of the canyon is equal to one near a wall. Especially roughness of the surface materials is expected to have a large influence on the development of the vertical wind profile near the surface. The shear forces by surfaces, the speed of the synoptic winds, the heating of surfaces creating buoyant air, and the stepping-up or down of canyon walls all induce further turbulence in the cavity air mass in a very complex and dynamic fashion which cannot be explained by a simple logarithmic profile.

8.5.2 Recommendations

Since this research component provides only an exploratory look on the parametrization of the vertical wind profile in LASER/F there are many improvements to this assessment that could give interesting results and are listed below. Most are related to changing the control variable of the simulation to obtain a larger breadth of perspectives on turbulent behaviour in the canyon.

- *Add vertical line as profile in LASER/F* - With the extracted CFD profiles in mind, the parametrization of wind flows in LASER/F would be improved if a vertical line (so constant horizontal wind speeds) is implemented for all heights between 0 and the top of the canyon h. When height h is reached, one could implement a profile that has a clear boundary layer. This is of course a first proposition and therefore it has to be supported by multiple comparisons between the 1D-profile and vertical profiles from the CFD under different circumstances. See hereafter for some options of variations with the CFD model.
- *Vary time* - In this assessment only one profile is taken at a fixed time where it is expected to give the most turbulent wind flow. However, this is gross speculation. The assessment would benefit from a set of profiles extracted at different times of the day, in the same horizontal position. Comparison of vertical wind profiles

throughout the day and between days would be interesting, and is possible with the CFD-model used in this project. One has to keep in mind that this time dependency is very computational intensive, since for every time step several iterations (40-50 at minimum) have to be performed.

- *Vary synoptic wind speed and direction* - Synoptic wind speed and wind direction is fixed in the simulation. This limits the number of comparable results and assumes that the turbulent behaviour is not dynamic. It is known from the field campaign that synoptic wind speed and direction is changing throughout the day and over days. Surely, this is expected to change the turbulent behaviour over and within the canyon. While it is not expected that the outcomes will lead to an clearer overall parametrization, it would give a better indication of the relationship between the synoptic wind conditions and local conditions in the canyon cavity.

- *Take more vertical profiles throughout the canyon* - More cross-sections of vertical wind profiles through the length of the canyon will elucidate the horizontal turbulent behaviour as affected by geometry. This is a very easy experiment to implement since no new simulations have to be run to extract extra lines from the CFDmodel.

- *Take horizontal profiles* - A section looking horizontally through the canyon would also provide interesting results to determine how the geometry and direction of the wind affects the flow of air through the canyon. The literature suggests that if winds are entering on an oblique angle to the canyon orientation, a funneling effect might occur, transporting heat and pollutants through the canyon. Horizontal wind profiles could better illustrate whether this happens or not.

- *Simulate an open canyon* - The simulation used a closed case of the obstacle geometry, to better represent the conditions of the canyon cavity. It could be speculated that when the incoming synoptic wind is perpendicular to the obstacle that closes the canyon, this obstacle creates turbulence before the air reaches the cavity of the canyon. To test this hypothesis, an open case of the canyon could be run, and the same vertical profiles extracted and compared.

- *Increase complexity of the obstacles* - By the same argument as running an open case, the same method could be implemented but with using more complex geometry. While this might not provide any dramatically new results with respect to the general vertical wind profile, it might indicate a sensitivity of the CFD model, just as was done with LASER/F. Moreover, the surface properties of the facade materials could also be incorporated (such as surface roughness term).

- *Use surface temperature as an input* - To make the comparison between the two models more accurate, one can use surface temperatures that are given as an output of LASER/F. The expectation is that the current assumptions of one constant surface temperature for all illuminated surfaces and one for all objects in the shadow are too coarse. This influence has to be investigated in more detail.

- *Increase the number of control points in the line extraction* - The reason for is that one gets multiple profiles next to each other on one line. This is very easy to implement. So one can extract profiles that are not in the middle of the canyon, but more near the facades of the buildings. It is expected that these profiles will be different due to the boundary layers that build up near the walls. This may be another reason to adapt the current general parametrization and therefore it needs to be investigated in more detail.

- *Compare radiant fluxes* - With the current method of comparing the different vertical wind profiles, one cannot conclude much about the influence of the deviating wind speeds on the radiant exitance or the surface temperatures, which are eventually the parameters of interest. Therefore a method has to be found to compare the radiant fluxes. Here, one has to overcome the problem of different grids and cells/surfaces. Next to this, implementation of this recommendation opens the way to qualify the outcomes of both models statistically.

- *Add vertical wind speeds and find comparison methodology* - In terms of total heat transport by air-motion through the canyon, the vertical windspeeds have to be extracted from the CFD-model, which is really easy (there is a option present in OpenDX). Also, these values have to be calculated for the LASER/F-model in order to compare them in a suitable way.

Chapter 9

Conclusions & recommendations

As stated in Chapter 1, the main goal of the GSP 2012 project was to investigate the sensitivity of LASER/F to changes in 3D geometry complexity. Or in other words, the influence of level-of-detail on the accuracy of micro-climate simulations within an urban canyon. The hypothesis was that level of detail does influence the accuracy of the model, especially with respect to the characteristics and design of building facades.

The main model used in this investigation was the LASER/F model provided by the LSIIT group of the University of Strasbourg, which has been developed to simulate radiative, conductive and convective fluxes in an urban canyon [7]. To investigate the effect of the geometry of buildings on the simulations, several different simulation scenarios were proposed and tested. A field campaign was set up at the site of interest, the Rue de l'Argonne in Strasbourg, France, to obtain thermal measurements. The results of the simulations were compared to thermal measurements to assess the accuracy of the micro-climate simulations.

Next to the LASER/F model, a CFD wind model by the Transport Phenomena group of TU Delft was run to obtain more insight into the effects of turbulent wind flow. The results of this investigation, which can also be found in Section 8.4, could provide advice on how the parametrization of the wind model in LASER/F can be improved. In this Chapter all final conclusions and recommendations are presented.

9.1 Conclusions

The initial hypothesis was that specific geometric features would have a significantly higher influence on the accuracy than others and that increasing the complexity in the 3D geometry of the urban canyon would lead to increasingly accurate simulations of radiative, conductive, and convective flux calculations in the LASER/F model. However, the analysis of the results indicate that this is not always the case both because of the systematic errors inherent in LASER/F, the methodology used and the importance of particular geometry features (e.g. balconies and windows) to the characterization of a facade. Thus, the decision on the 3D model level of complexity will have to be based on whether certain geometric features significantly describe the characteristic shape of a facade. For example, it is not important to model the balconies if without them the facade is still recognizeable relative to what it represents.

With the overview of the outcomes and their meaning presented in respectively Chapter 7 and Section 8.4, this section is solely meant to give the reader the opportunity to grasp the essence of the results. These are listed below.

1. A systematic error was observed in all results, and simulated temperatures were consistently lower than measured temperatures. This is caused by measured radiant exitance differing from simulated radiant exitance, the measured one often being higher. This could also be induced by incorrect or over-generalized material properties in LASER/F and the overestimation of sensible heat flux, leading to lower simulated diurnal surface temperatures. Also, since the geometric input to the LASER/F model is deduced from the CAD model (which is created using photogrammetry), the volumes of all the buildings in the canyon are not accurately modelled. As a consequence the internal heat storage of the buildings as well as the heat inertia of the buildings is lower, causing the radiative fluxes in the canyon to be lower as well.

2. The investigated buildings (1 and 4 Rue de l'Argonne) show a different radiant exitance behaviour over time. This is likely due to their location in the canyon and thus the timing of exposure to direct solar radiation. It is also explained by the significantly different shape and materiality of the facades that affects their surface area and rates of flux. 1 Rue de l'Argonne is illuminated in the morning (during warming hours) and 4 Rue de l'Argonne is illuminated in the afternoon (during cooling hours).

3. Compared to the CFD model, horizontal wind speeds are generally more than $0.5\,\mathrm{m\,s^{-1}}$ greater for the majority of the measurement points in the canyon. This suggests that the exponential wind profile of LASER/F is not able to reflect boundary layer flow well at the surface of obstacles. This might also explain why simulated surface temperatures are consistently cooler than measured temperatures. Wind motion is known to have a cooling effect, as it transports heat out of the canyon.

4. In general, increasing the complexity of the 3D model also increased computation time. However, the simulation accuracy did not necessarily increase. The most complex geometry scenario yielded lower errors than the vertex welding scenario, but was less accurate than when balconies were added, especially for 4 Rue de l'Argonne. Moreover, the lowest errors occurred at night during the cooling period

and the highest during the warming period. Attention might need to be paid to introducing a dynamic parametrization of the model depending on sunrise and sunset hours to correct for this effect.

9.2 Recommendations

Based on the conclusions, there are several ways in which either the accuracy of the LASER/F or the methodology used within the project could be improved.

9.2.1 LASER/F

Considering the LASER/F model, of main concern is the systematic error encountered in the results of the simulations compared to the measurements taken. The following recommendations could improve the issue encountered.

- *Improving vertical wind profile* - Adjust the vertical wind profile model in LASER/F to more accurately represent what was found using the CFD model (in general the wind speed should be lower than what is currently modelled using a logarithmic profile). Moreover, conduct further experiments using the CFD model to better parametrize the profile (Chapter 8).

9.2.2 Methodology

Next to the LASER/F model simulation, project methodology could also be improved to obtain better results.

- *Improving material properties* - Verify for each building studied that the thermal properties are correctly parametrized. Ensure that they are specified especially when there are dominant or distinct materials on a facade, each should be described accurately.

- *Modelling of building volumes* - Use building geometry that contains the full volume of the buildings in the canyon, even if it is a rough estimate, as this will better estimate the internal heat storage behaviour of the buildings.

- *Using a consistent model* - The level of complexity of the AutoCAD model should be consistent throughout the canyon, not only on a portion of it as was used in this research. Even though all windows and balconies of 4 Rue de l'Argonne were modelled, re-projection errors were encountered after using model coordinates as ground control points.

- *Thermal image measurements* - Define the ground control points before doing the measurements to yield more consistent results. The area covered by the thermal measurements shows inconsistencies in position at several epochs. To this end some thermal imagery had to be rejected because of the absence of ground control points.

- *Overlap between thermal images* - Increase overlap of thermal images to take advantage of techniques like bundle adjustment and therefore decrease the image processing time.

- *Take exact time instances into account* - As measurements during a campaign might be taken at different time instances than the time instance which the corresponding simulation result represents, care should be taken that the time difference between the two is still within reasonable bounds (e.g. model time interval).

9.2.3 Future work

It is also interesting to think about how the methodology could be applied again (with the improvements mentioned above), but also given more study time. Two suggestions are:

- *Increase sample size* - Select two or three more facades from the same canyon that exhibit similar surface features (similar materiality and geometries). The two facades of 1 Rue de l'Argonne and 4 Rue de l'Argonne are architecturally very different and exhibited different diurnal behaviour. It would be interesting to compare the results of two facades that look similar but are at different positions in the canyon.

- *Change canyon geometry* - Without having to choose a new study site, the orientation and aspect ratio of the canyon could be changed through coordinate transformations in order to determine the sensitivity of LASER/F to aspect ratio and orientation. The expected parametrizations can be taken from the literature and the results compared against these as well as the results in this report.

This short research project has been able to demonstrate that 3D geometry complexity does matter when it comes to accurately simulating radiative, conductive, and convective fluxes in an urban canyon. But the magnitude of influence that geometry plays essentially depends on whether particular facade features are a dominant part of the architectural character of the facade. A rule of thumb might be that in future use of LASER/F, one should consider using facade elements like windows, balconies, awnings if without them a facade is not recognizable in the 3D model. The question might be asked whether the material covers a particular percentage of the facade (e.g. if the fraction of glazing is significant). Ideally, the canyon should not be generalized in a homogeneous fashion, but buildings should be generalized on a case-by-case basis in order to achieve the most accurate results. By this method, LASER/F can continue to act as a useful tool in characterizing climate in urban canyons for research. From an application perspective, the research results may be interesting to consider when modeling heat fluxes for urban neighbourhoods or districts to perhaps predict ’hot-spots’ within the city. It may be that not much facade detail is always necessary to model, although building volumes, roofs, and perhaps signficant balconies are. Significant computational power and time is required for such a study.

Glossary

Absorption The process in which radiant energy is retained by a substance. [51]

Absorptivity The absorptivity is the property that defines the fraction of the incident energy that is absorbed by a surface. By Kirchhoff's law it is equal to emissivity. [52]

Advection Heat advection takes place through the net displacement of a fluid, which translates the heat content in a fluid through the fluid's own velocity. [53]

Air temperature The ambient temperature indicated by a thermometer exposed to the air but sheltered from direct solar radiation. [54]

Albedo The hemispherically and wavelength integrated reflectivity (in general from 0.2 to 4.0 μm) of a surface. This definition applies to simple uniform surfaces as well as to heterogeneous and complex ones. [55]

Anthropogenic heating Heat released to the atmosphere as a result of human activities, often involving combustion of fuels. Sources include industrial plants, space heating and cooling, human metabolism, and vehicle exhausts. [56]

Bounding box A bounding box defines a range of values along each axis which together contain a certain area or volume.

Brightness temperature Brightness temperature of a body is the temperature of the equivalent black body that would give the same radiance at the wavelength under consideration. [57]

Bundle adjustment "Bundle adjustment is the problem of refining a visual reconstruction to produce jointly optimal 3D structure and viewing parameter (camera pose and/or calibration) estimates." [46]

CityGML "CityGML is an open data model and XML-based format for the representation and exchange of virtual 3D city models. It is based on the Geography Markup Language version." [38]

Conduction Conduction is the transfer of heat from one part of a body at a higher temperature to another part of the same body at a lower temperature, or from one body at a higher temperature to another body in physical contact with it at a lower temperature. [52]

Convection Convection, sometimes identified as a separate mode of heat transfer, relates to the transfer of heat from a bounding surface to a fluid in motion, or to the heat transfer across a flow plane within the interior of the flowing fluid. [52]

Cycle slip A discontinuity of an integer number of cycles in the measured (integrated) carrier phase resulting from a temporary loss-of-lock in the carrier tracking loop of a GPS receiver.

Diffuse reflection The radiation is reflected omni-directionally according to Lambert cosine law. [58]

Emissivity The ratio of the radiation emitted by a surface to that emitted by a black body at the same temperature. [51]

Evapotransiparation The sum of evaporation and plant transpiration. Potential evapotranspiration is the amount of water that could be evaporated or transpired at a given temperature and humidity, if there was plenty of water available. [51].

Form factor A geometric property which is defined as the fraction of radiation leaving one surface that reaches another surface. It depends on the orientation of the surfaces to each other and their distance.

Heat capacity Refers to the quantity that represents the amount of heat required to change one unit of mass of a substance by one degree. [53]

Heat flux The rate of heat flowing past a reference datum. [51]

Heat transfer Heat is defined as energy transferred by virtue of a temperature difference. It flows from regions of higher temperature to regions of lower temperature. It is customary to refer to different types of heat transfer mechanisms as modes. The basic modes of heat transfer are conduction, radiation, and convection. [52]

Infrared radiation Electromagnetic radiation of wavelengths approximately between 0.75 and 1000 mm. [54]

Irradiance The irradiance at the surface is defined as the total incident power per unit area and its unit is $\mathrm{W\,m^{-2}}$.

Latent heat The heat that is absorbed or released by a substance when it changes state, for example from a liquid to a gas, while the temperature of the substance remains unchanged. [59]

Orthophoto When the images are captured by the camera, they are created as a central projection of the object space. The central projection introduces some displacements. These displacements are removed in an orthophoto. An orthophoto is basically an orthogonal projection of the objects in an image. [60]

Radiance The radiance $\mathrm{L(W\,m^{-2}\,sr^{-1})}$ of a surface is defined as the amount of radiant flux it emits per unit of projected area and per unit of solid angle. [61]

Radiant energy All bodies constantly emit energy by a process of electromagnetic radiation. This is called radiant energy. [62]

Radiant exitance The outgoing analogue of irradiance. [57]

Radiant flux The radiant energy per unit time. [57]

Radiant flux density See irradiance.

Radiant intensity The amount of radiant flux emitted per unit of solid angle. [61]

Radiation Radiation, or more correctly thermal radiation, is electromagnetic radiation emitted by a body by virtue of its temperature and at the expense of its internal energy. [52]

Radiosity The emitted plus reflected power leaving a surface ($\mathrm{W\,m^{-2}}$). [57]

Reflectivity The fraction of radiant energy reflected by a surface.

Sensible heat The heat absorbed or transmitted by a substance during a change of temperature which is not accompanied by a change of state. Used in contrast to latent heat. [54]

Sky view factor The fraction of visible sky and the entire sky hemisphere from a certain point. It varies between 0 when no sky is seen at all and 1 when the sky hemisphere is entirely visible.

Space resection "Space resection is the determination of the position of the perspective center and the orientation of a frame camera by using features in the object space as control." [63]

Specular reflection The angle of the reflected beam with respect to the targets surface is equal to the angle of incidence. [58]

Thermal radiation All bodies with a temperature greater than absolute 0 K emits thermal radiation. The intensity of thermal radiation is directly related to the temperature of the body.

Transmittance A fraction of the total incident energy which passes through the body is called transmittance. [62]

Urban boundary layer The layer of air above roof level, which is affected by the presence of the urban surface below. It is a local- to meso-scale phenomenon controlled by processes operating at larger spatial and temporal scales. [15]

Urban canopy layer The layer of air extending from the ground up to about the mean roof level in which processes of airflow and energy exchange are controlled by micro scale, site-specific characteristics and processes. [15]

Urban Heat Island The phenomenon in which An urban area has a higher temperature compared to the rural area surrounding it.

Appendix A

Project management and process

The GSP was executed within an eight-week time frame that was divided into four phases. The process was managed in a collaborative fashion, with technical and scientific guidance from the supervisors and partners at TU Delft and LSIIT. Below, a review of each phase documents the objectives, outcomes, risks and mitigation strategies used.

A.1 Project management

The project concept was initiated in early 2012, where work was done to arrange a partnership with LSIIT and TU Delft. The research project itself was selected in a collaborative fashion. At the launch of phase I in September 2012, team roles were also defined collaboratively for each student, according to interest and existing expertise. The tasks and responsibilities were outlined in phase I, and included in the baseline report (Figure A.1). These are primarily project management roles such as the chair of meetings, communications officer, external communications officer and quality assurance. It was important to do so to establish some consistency in the flow of work. At the mid-term, each member's individual role was reviewed and only minor adjustments were made (e.g. changing persons for the communications officer) as it was most efficient for the project to maintain the current roles.

Secondly, preliminary content-based sub-teams were formed in phase I, based on the anticipated tasks for phase II. A sub-team on preparing the 3D geometry for the LASER/F model and another sub-team for coordinating the field work was established.

In phase II, the existing 3D geometry sub-team remained. A fieldwork sub-team was formed with the remaining students, who were present for the installation and training of use of measurement equipment. Students from each of the two groups also formed small working teams to spearhead the literature review, and work specifically on the GPS positioning. Besides this, the students were able to begin writing for the mid-term report, test-run a few simple cases on LASER/F, and arrange additional meetings including a wrap-up.

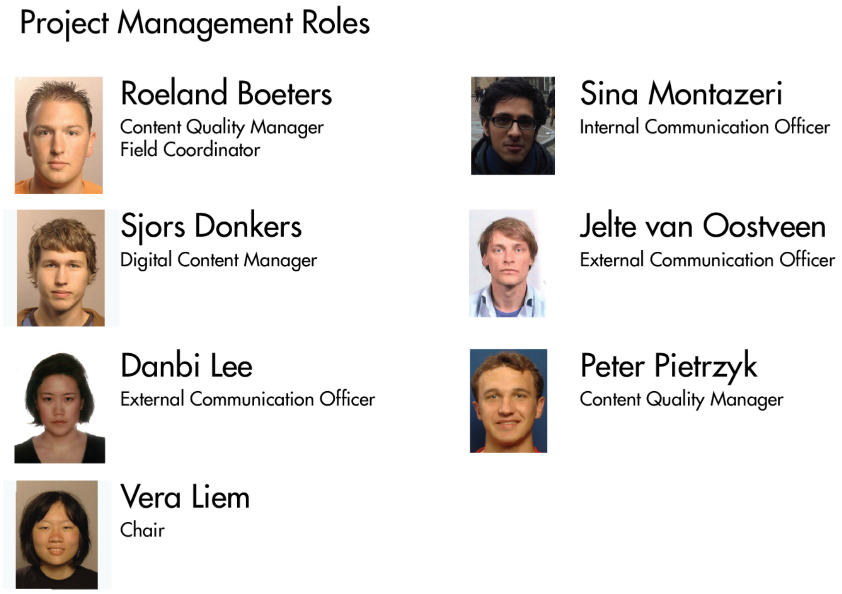

Figure A.1: Team roles at the outset of the project

In phase III and IV, a third sub-team for working on the CFD wind model was formed. And the same work continued with the sub-teams of phase II, with the exception that the literature review team was expanded in order to accelerate the work. Finally, preparations for the GSP symposium also began by securing speakers and other logistics. The allocation was based primarily on existing role structures and the fact that the 3D geometry sub-team was consistently at full capacity whereas others were able to move onto other requires tasks. Consideration was given to having all team members present project work at least once throughout the process. Four presentations were given (baseline presentation, mid-term presentation, final presentation, GSP symposium).

Revisions to the scope of work

One of the key challenges in this process was the compressed time frame within which to complete this research project. Initially, the team was quite ambitious as to what could be completed within the eight weeks allocated. And because the team was given flexibility in refining the research question, it was left rather open in the first phase. It was agreed that the scope of work would be refined in phase II in collaboration with LSIIT.

In the baseline report, two broad research questions were stated. The first was related to experimenting with LASER/F, on the effect of 3D geometry complexity on the simulation of radiative fluxes in an urban canyon. This still remained unchanged and was the focus of the work. A sub-question was about the effect of material or surface properties on radiative flux. The intent would have been to vary the material/surface types of the facades while fixing the 3D geometry complexity and comparing the results. However, because the work for the main research question turned out to be quite substantial, the sub-question was not experimented with explicitly. The only experimentation with material/surface type was in the determination of the baseline conditions on which to test the main research question (so adding grass versus no grass).

The second research question was about the effect of radiative flux on air turbulence in the cavity of the urban canyon. The intent was to use the LASER/F output (of surface temperatures) as an input into a TU Delft CFD model (from the Transport Phenomena group) and to compare this with a simulation without surface temperature as an input. However, upon discussion with the model developers and given the time constraint, it seemed infeasible to execute this experiment. This work was planned already as part of a Ph.D. thesis at TU Delft, so it did not seem realistic to implement it successfully in one or two weeks time, as well as process the results. Instead, what was decided with the supervisors was to simply compare the vertical wind profiles between LASER/F and the CFD model and draw a conclusion on the logarithmic wind profile assumption made in LASER/F.

These decisions on the scope of work was made at every phase in the process. In phases I, II, and III, weekly follow-up meetings and consultations with supervisors helped to refine the scope of work. Also informing the decision was the fact that the time to run the LASER/F simulations, post-processing of thermal images, running the CFD model and validating the results was much more than anticipated based on preliminary runs in phase II and III.

The involved people for each part of the report can be found in Appendix B.

A.2 Phase I review

Phase I, week 1, involved the kick-off of the GSP at TU Delft on September 4^{th}, 2012. Supervisors and students met to discuss the research objectives and work plan and prepared other logistics in preparation for phase II.

A.2.1 Objectives

The objective of phase I was to solidify the research objectives and the work plan over the course of the project. It was also important to begin developing a collective theoretical background about urban climatology and UHI. A presentation on UHI and of CFD wind modelling was arranged to initiate the research.

A.2.2 Outcomes and deliverables

One of the key deliverables for this phase was the baseline report, submitted on September 14^{th}, 2012. The baseline report included a global overview of the research project including all logistic and project management considerations, an outline of the overall research questions, a work plan description and proposed resource allocation for phases I and II. The report was completed in collaboration with the supervisors in order to ensure the inclusion of needed content and level of detail. It also provided a good starting point for the work to be done at the University of Strasbourg.

Besides the baseline report, a presentation by Patrick Schrijvers on the CFD model theory and by Peter Pietrzyk on UHI overview was held at the TU Delft campus. The research paper by Kastendeuch and Najjar [7] was also read to round-off the preparation for field work. An agreement was made between the students and the supervisors to hold weekly feedback meetings on Fridays in order to keep the supervisors informed and allow an opportunity for students to receive feedback on the work done to date.

A.2.3 Risks and mitigation

Due to the short period of the entire research project, and the necessity of working in Strasbourg as early into September as possible, it was essential to shorten this phase to one week. While in a typical project process the kick-off phase would be extensive enough to allow for the establishment of working relationships, an in-depth study period of the literature and the further refinement of the research questions, in the case of the GSP, this scenario was not possible. Essential objectives (noted above) were met and allowed the project to move forward smoothly. Furthermore, there was enough flexibility in phase II to allow for an overflow of tasks from phase I. For example, building the theoretical background was not as extensive in this week, but was picked up in phase II and phase III with only a consequence of time. Working relationships were also built rather quickly while working closely together with the supervisors and LSIIT.

A.3 Phase II review

Phase II, weeks 2 to 3, involved the field campaign at the University of Strasbourg from September 10^{th} to September 21^{st}, 2012. Two supervisors attended a portion of the campaign to provide additional research guidance. These dates were selected based on the recommendation by LSIIT as it was the ideal time for conducting the field work.

A.3.1 Objectives

The objectives of phase II were to collect standard meteorological measurements for input for the LASER/F model and surface temperature measurements of canyon facades in the urban canyon for model validation. In order to meet these objectives, training of using the measurement equipment and the LASER/F model was necessary and was provided by Jerome Colin, Francoise Nerry and Pierre Kastendeuch. Further assistance was provided by Georges Najjar and the Geography Department on Rue de l'Argonne in Strasbourg.

A.3.2 Outcomes and deliverables

The first week of phase II included the introduction and training of LASER/F and the FLIR thermal camera theory and use. In terms of field work, this week was used to install the meteorological station on the roof of the 'Institut de Physiologie et de Chime Biologique' building, about 600 m south-west of Rue de l'Argonne. Data was successfully gathered for an uninterrupted period of five days. In the second week, a 24-hour measurement campaign of the surface temperature of two facades was also completed. The remainder of this phase was used to interpret the data and discuss processing techniques of thermal imagery with the supervisors and LSIIT. A full description of the field work is found in the text. In the office, 3D geometry of the urban canyon was converted, generalized and smoothed. There were several workshops on determining the test cases for input into LASER/F in order to generate interesting comparisons. Moreover, it was possible even to test-run some simple geometry in LASER/F to estimate time budgets for running the full suite of test cases. This was a valuable advancement in the process.

A.3.3 Risks and mitigation

With respect to the field campaign, the main concern was having the right weather/meteorological conditions to conduct the field work. While there was some uncertainty about the weather before beginning this phase, there were luckily more ideal weather days than not. The field work in the canyon was strategically selected for the two most sunny and clear days forecast, and ideally occurred in the middle of the phase. It was necessary to be ready to work on the weekend as well, depending on the weather conditions.

Because the training of LASER/F occurred simultaneously with the 3D model preparation and generalization process, it was not always easy to decide the test cases to prepare (that is, defining different levels of detail while balancing time and quality of the test cases). However, there was adequate expertise in the group to move forward quickly and in parallel, conduct a few pilot runs on LASER/F which helped to identify further questions to ask about the model and understand the model in further depth.

Another risk at the start of phase II was the potential challenges in collaborating with LSIIT. It was possible that scheduling conflicts or even language barriers could exist. However, this turned out not to be a problem, as everyone was in daily contact and communication with each other and responded to meeting requests promptly. The team at LSIIT in particular were highly accommodating and available for consultation at all times. Each day the students were able to check-in with the supervisors and LSIIT to ensure schedules were aligned. Two follow-up meetings, emailing, telephone calls, and simply having an office next to the supervisors was important in mitigating this risk.

The last risk in this phase was due to not having a strong theoretical background of the research topic prior to undertaking field measurements. It probably increased the time taken to develop proper measurement methods (extra time taken to understand precisely what is measured and how to optimize the measurement success). Discussions with LSIIT and the supervisors could have been enhanced and more specific a stronger theoretical background had been established. Nevertheless, this challenge did not compromise meeting the phase II objectives as material was learned on an ad-hoc basis.

A.4 Phase III review

Phase III, weeks 4 to 6, involved the synthesis and validation of the data gathered in phase II and the preparation of the symposium. This was conducted back at TU Delft in the Geomatics lab of the Faculty of Architecture. Several consultations with the supervisors and LSIIT were necessary to establish an appropriate method for LASER/F validation. The team was also able to present the work to date at the Mid-term Review and the section meeting of Optical Remote Sensing at Civil Engineering and Geosciences.

A.4.1 Objectives

The objective at this point was to process the data collected in phase II, run the simulations of LASER/F using the seven different geometry scenarios and finally to generate a set of results following a validation of the results. It was also critical to run the CFD model to conduct a comparison of the vertical wind profile between the LASER/F model and CFD model. Finally, the symposium was also organized, including the confirmation of four speakers (see Section A.6).

A.4.2 Outcomes and deliverables

Phase III began with the completion of the 3D geometry scenarios and the preliminary runs of these cases in LASER/F. The first week was also used to resolve the issues with the GPS measurements (which in the end were not successfully processed) and defining a method to rectify, correct and compare the thermal imagery to the LASER/F outputs. Week 4 also included a visit to Patrick Schrijvers who introduced the CFD model tutorial to a sub-team. After some discussion about the time versus the relevance of using the model as part of the research, it was decided to continue with using the CFD in week 5, at least as a method of testing the hypothesis on the effect of an gross simplification of the wind profile in LASER/F. While all the tasks in this phase took longer than expected, the LASER/F simulations were all successfully run, a validation method was decided upon and executed, and the CFD model was also run successfully. The symposium was organized within two weeks time, with ample time to advertise and generate interest in the event.

A.4.3 Risks and mitigation

Initially, there was concern with the amount of available time to validate the test cases and moving forward with the CFD model. For example, the balcony cases could not be run successfully by LASER/F and had to be resolved quickly. So in order to keep balconies as a test case, it was necessary to add balconies as part the facade geometry (same material type and object). Additionally, to run the CFD model, additional preparation for the 3D model had to be made (the extraction of building points that represent the building envelope). Thus, some additional work had to be done in order to use the CFD model, with other tasks slightly delayed.

Besides this, there was still a substantial amount of work on building the body of literature that was supposed to initially guide the research. As this became the priority in the beginning of this phase, other tasks had to be pushed back. One of those was moving forward with planning the GSP symposium, such as contacting potential speakers. Fortunately, the dates for the final presentation and symposium were pushed to early November, adding an additional two weeks to the project. The time to complete the CFD component of the project was also delayed, due to technical issues with the computers in the Transport Phenomena computer laboratory. However, results were obtained in time for this report.

It also took more time than anticipated to establish a validation procedure, because there was extensive discussion with the supervisors on how to process the thermal images (whether and what corrections to use, what statistics to use to validate them and balanced with the time available) which meant that the results of the research were obtained well into phase IV.

A.5 Phase IV review

Phase IV, weeks 7 to 8, involved the completion of the validation procedure, and drawing of conclusions and making recommendations. The final technical presentation to the supervisors and the GSP symposium was also held in this last phase.

A.5.1 Objectives

The objective of the last phase was to wrap-up all validation work from the previous phase and to prepare a set of conclusions and recommendations for the research, based on the results. Of course, it was also important to organize the final technical presentation and Symposium to showcase the results.

A.5.2 Outcomes and deliverables

Because this phase was just a short two weeks, the writing of the final report overlapped with the remaining validation tasks of phase III. In particular, it was important to process the thermal images and generating statistics to compare the results between the different geometry scenarios. Final conclusions on the CFD model were also made through visualizations of the turbulence patterns in the canyon and an extraction of the vertical wind profile. Much work was done on finalizing the logistics for the final presentation and symposium.

A.5.3 Risks and mitigation

The major risk at this phase was in generating results to present. Because tasks in phase III took longer than expected, the results were obtained in phase IV, which was not planned. Nevertheless, it was possible to move forward on writing all other parts of the final report such that all remaining time in the last week of work would be devoted to writing conclusions and recommendations.

A.6 GSP Symposium

The GSP Symposium was held on Thursday 8 November, 2012 at the tribune steps of the Faculty of Architecture. The symposium was intended to showcase the main results of the research to a broad public audience interested in the issue of urban heat. It is also intended to be a platform to relate this research to other fields of study and to stimulate thought on collaborative solutions.

A.6.1 Speakers

The following speakers presented at the GSP symposium:

- Drs. Peter Bosch of TNO presented a broad overview of work by Knowledge for Climate Proof Cities consortium. Dr Bosch gave a broad overview of urban climatology and its relevance to society.

- Dr. ir. Frank v/d Hoeven, Research Director at the Faculty of Architecture, TU Delft, presented his project 'Amsterwarm' on the application of observation data of urban heat in city building policies in Amsterdam, with a focus on the importance of such data in planning processes.

Time	**Symposium item**
12:30 - 13:30	Students welcome the speakers to the Faculty (main entrance)
14:00	Opening/ welcoming by supervisors
14:10	Keynote Speaker: Peter Bosch (TNO)
14:30	Second Speaker: Frank v/d Hoeven (Architecture - TU Delft)
14:50	Break
15:15	Synthesis Presentation
15:45	Question and Answer
16:00	Third Speaker: Peter Joosten (Cyclomedia)
16:20	Closing Speaker: Bert van Hove (Alterra/Wageningen)
16:40	Message of thanks and borrel at Bouwpub, BKCity

Table A.1: GSP symposium itenary

- Peter Joosten, Senior Consultant of positioning systems at Cyclomedia, presented on the development of technology in street-level acquisition and photogrammetry. The presentation focused on challenges and prospects for city modelling.
- Dr. Bert van Hove, Assistant professor in climate change and air quality at the University of Wageningen, presented a paper on the quantification of the urban heat island effect and human comfort in the Netherlands using data from hobby meteorologists.

A.6.2 Itinerary

The itinerary for the GSP symposium can be seen in Table A.1.

A.6.3 Advertisement and Promotion

The symposium was promoted in two waves. The first wave involved many 'teaser' advertisements that indicated the time, date and place. Screen advertisements in Civil Engineering and Geosciences, Architecture and the Institute for the Built Environment were run for two weeks. Notifications were included in the bi-weekly B-Nieuws magazine and BKCity News (online edition) and the CT Nieuws newsletter. 'Hold the date' emails were spread to faculty, staff and students of whom the GSP team had been in contact with. An event page was made on Facebook to attract more students to the event.

The second wave of advertisements began two weeks prior to the symposium where speaker information was also provided in the advertisements. Posters were placed in the faculty buildings mentioned above and a final reminder email was sent. A full-page article on the project was also featured in B-Nieuws.

Appendix B

Task division

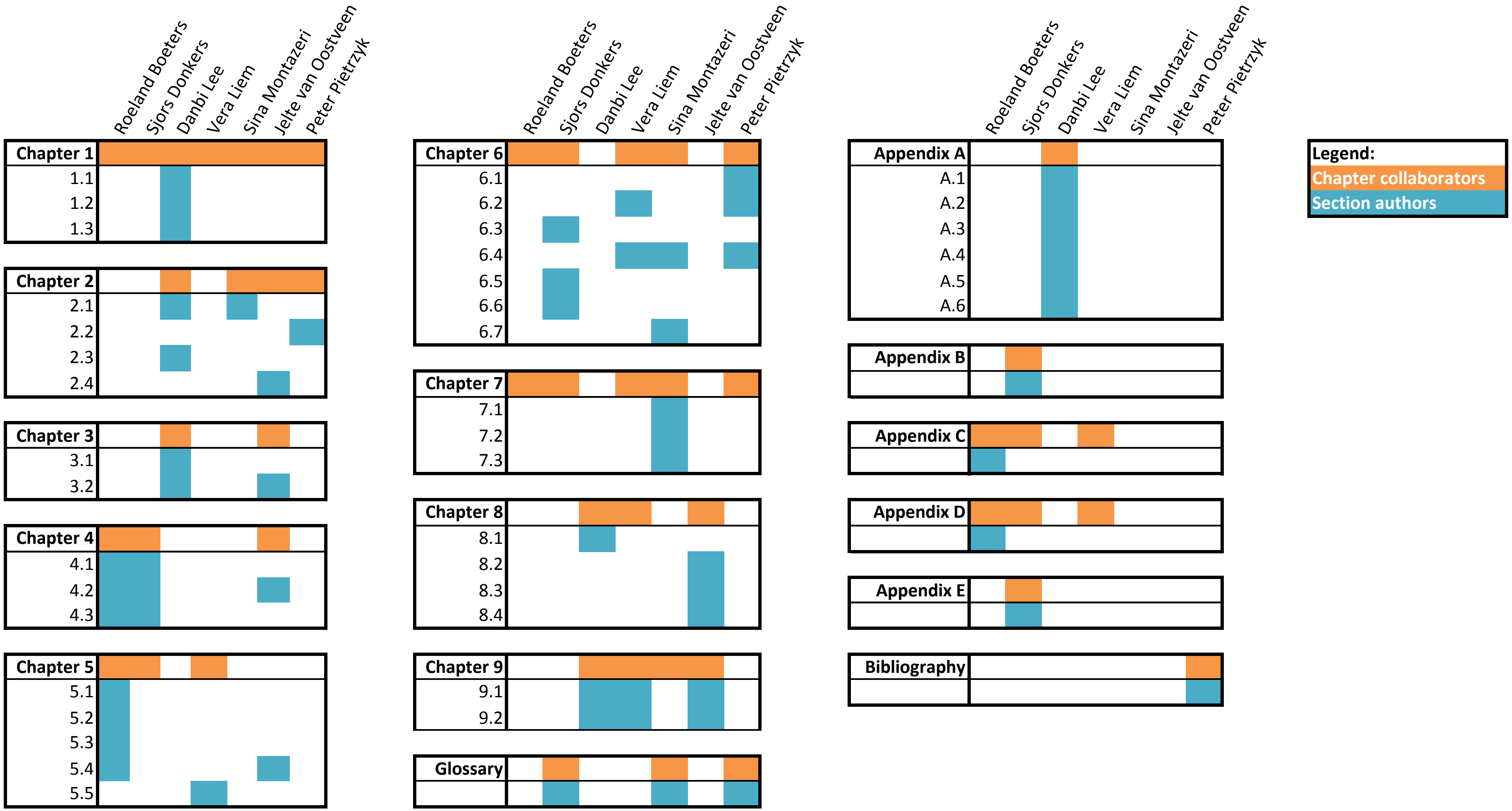

	Roeland Boeters	Sjors Donkers	Danbi Lee	Vera Liem	Sina Montazeri	Jelte van Oostveen	Peter Pietrzyk
Chapter 1	🟧	🟧	🟧	🟧	🟧	🟧	🟧
1.1			🟦				
1.2			🟦				
1.3			🟦				
Chapter 2			🟧		🟧	🟧	🟧
2.1			🟦		🟦		
2.2							🟦
2.3			🟦				
2.4						🟦	
Chapter 3			🟧			🟧	
3.1			🟦				
3.2			🟦			🟦	
Chapter 4	🟧	🟧				🟧	
4.1	🟦	🟦					
4.2	🟦	🟦				🟦	
4.3	🟦	🟦					
Chapter 5	🟧	🟧		🟧			
5.1	🟦						
5.2	🟦						
5.3	🟦						
5.4	🟦					🟦	
5.5				🟦			

	Roeland Boeters	Sjors Donkers	Danbi Lee	Vera Liem	Sina Montazeri	Jelte van Oostveen	Peter Pietrzyk
Chapter 6	🟧	🟧		🟧	🟧		🟧
6.1							🟦
6.2				🟦			🟦
6.3		🟦					
6.4				🟦	🟦		🟦
6.5		🟦					
6.6		🟦					
6.7					🟦		
Chapter 7	🟧	🟧		🟧	🟧		🟧
7.1					🟦		
7.2					🟦		
7.3					🟦		
Chapter 8			🟧	🟧		🟧	
8.1			🟦				
8.2						🟦	
8.3						🟦	
8.4						🟦	
Chapter 9			🟧	🟧	🟧	🟧	
9.1			🟦	🟦		🟦	
9.2			🟦	🟦		🟦	
Glossary		🟧			🟧		🟧
		🟦			🟦		🟦

	Roeland Boeters	Sjors Donkers	Danbi Lee	Vera Liem	Sina Montazeri	Jelte van Oostveen	Peter Pietrzyk
Appendix A			🟧				
A.1			🟦				
A.2			🟦				
A.3			🟦				
A.4			🟦				
A.5			🟦				
A.6			🟦				
Appendix B		🟧					
		🟦					
Appendix C	🟧	🟧		🟧			
	🟦						
Appendix D	🟧	🟧		🟧			
	🟦						
Appendix E		🟧					
		🟦					
Bibliography							🟧
							🟦

Legend:
🟧 Chapter collaborators
🟦 Section authors

Figure B.1: Task division for the project

Appendix C

ASE file example

```
*3DSMAX_ASCIIEXPORT 200
*COMMENT "AsciiExport Version  2.00 - Fri Sep 14 12:48:59 2012"
*SCENE {
*SCENE_FILENAME "6.max"
*SCENE_FIRSTFRAME 0
*SCENE_LASTFRAME 100
*SCENE_FRAMESPEED 30
*SCENE_TICKSPERFRAME 160
*SCENE_BACKGROUND_STATIC 0.0000 0.0000 0.0000
*SCENE_AMBIENT_STATIC 0.0000 0.0000 0.0000
}
*MATERIAL_LIST {
```

```
*MATERIAL_COUNT 1
*MATERIAL 0 {
*MATERIAL_NAME "Material #46"
*MATERIAL_CLASS "Multi/Sub-Object"
*MATERIAL_AMBIENT 1.0000 0.0000 0.0000
*MATERIAL_DIFFUSE 1.0000 0.0000 0.0000
*MATERIAL_SPECULAR 0.9000 0.9000 0.9000
*MATERIAL_SHINE 0.1000
*MATERIAL_SHINESTRENGTH 0.0000
*MATERIAL_TRANSPARENCY 0.0000
*MATERIAL_WIRESIZE 1.0000
*NUMSUBMTLS 2
*SUBMATERIAL 0 {
*MATERIAL_NAME "Roof"
*MATERIAL_CLASS "Standard"
*MATERIAL_AMBIENT 1.0000 0.0000 0.0000
*MATERIAL_DIFFUSE 1.0000 0.0000 0.0000
*MATERIAL_SPECULAR 0.9000 0.9000 0.9000
*MATERIAL_SHINE 0.1000
*MATERIAL_SHINESTRENGTH 0.0000
*MATERIAL_TRANSPARENCY 0.0000
*MATERIAL_WIRESIZE 1.0000
*MATERIAL_SHADING Blinn
```

```
*MATERIAL_XP_FALLOFF 0.0000
*MATERIAL_SELFILLUM 0.0000
*MATERIAL_FALLOFF In
*MATERIAL_XP_TYPE Filter
}
*SUBMATERIAL 1 {
*MATERIAL_NAME "Wall"
*MATERIAL_CLASS "Standard"
*MATERIAL_AMBIENT 0.5804 0.5804 0.5804
*MATERIAL_DIFFUSE 0.5804 0.5804 0.5804
*MATERIAL_SPECULAR 0.9000 0.9000 0.9000
*MATERIAL_SHINE 0.1000
*MATERIAL_SHINESTRENGTH 0.0000
*MATERIAL_TRANSPARENCY 0.0000
*MATERIAL_WIRESIZE 1.0000
*MATERIAL_SHADING Blinn
*MATERIAL_XP_FALLOFF 0.0000
*MATERIAL_SELFILLUM 0.0000
*MATERIAL_FALLOFF In
*MATERIAL_XP_TYPE Filter
}
}
}
```

```
*GEOMOBJECT {
*NODE_NAME "Layer:extruded"
*NODE_TM {
*NODE_NAME "Layer:extruded"
*INHERIT_POS 0 0 0
*INHERIT_ROT 0 0 0
*INHERIT_SCL 0 0 0
*TM_ROW0 1.0000 0.0000 0.0000
*TM_ROW1 0.0000 1.0000 0.0000
*TM_ROW2 0.0000 0.0000 1.0000
*TM_ROW3 21.1877 82.7256 30.0940
*TM_POS 21.1877 82.7256 30.0940
*TM_ROTAXIS 0.0000 0.0000 0.0000
*TM_ROTANGLE 0.0000
*TM_SCALE 1.0000 1.0000 1.0000
*TM_SCALEAXIS 0.0000 0.0000 0.0000
*TM_SCALEAXISANG 0.0000
}
*MESH {
*TIMEVALUE 0
*MESH_NUMVERTEX 16
*MESH_NUMFACES 28
*MESH_VERTEX_LIST {
```

```
*MESH_VERTEX    0 11.2962 79.2588 41.3103
*MESH_VERTEX    1 11.2956 79.2580 18.8784
*MESH_VERTEX    2 12.3044 78.5583 41.3103
*MESH_VERTEX    3 12.3039 78.5575 18.8784
*MESH_VERTEX    4 22.7075 95.6837 41.3094
*MESH_VERTEX    5 22.7070 95.6829 18.8776
*MESH_VERTEX    6 23.7157 94.9833 41.3094
*MESH_VERTEX    7 23.7152 94.9825 18.8776
*MESH_VERTEX    8 26.1695 98.5150 41.3092
*MESH_VERTEX    9 26.1689 98.5142 18.8774
*MESH_VERTEX   10 34.1586 92.9645 41.3092
*MESH_VERTEX   11 34.1580 92.9637 18.8774
*MESH_VERTEX   12 16.4768 66.9371 41.3106
*MESH_VERTEX   13 16.4763 66.9362 18.8788
*MESH_VERTEX   14 8.2173 72.6754 41.3106
*MESH_VERTEX   15 8.2167 72.6746 18.8788
}
*MESH_FACE_LIST {
*MESH_FACE    0:    A:    0 B:    1 C:    2 AB:    1 BC:    0 CA:    1  *MESH_SMOOTHING  *MESH_MTLID 1
*MESH_FACE    1:    A:    1 B:    3 C:    2 AB:    1 BC:    1 CA:    0  *MESH_SMOOTHING  *MESH_MTLID 1
*MESH_FACE    2:    A:    4 B:    5 C:    0 AB:    1 BC:    0 CA:    1  *MESH_SMOOTHING  *MESH_MTLID 1
*MESH_FACE    3:    A:    5 B:    1 C:    0 AB:    1 BC:    1 CA:    0  *MESH_SMOOTHING  *MESH_MTLID 1
*MESH_FACE    4:    A:    6 B:    7 C:    4 AB:    1 BC:    0 CA:    1  *MESH_SMOOTHING  *MESH_MTLID 1
```

```
*MESH_FACE    5:    A:    7 B:    5 C:    4 AB:    1 BC:    1 CA:    0  *MESH_SMOOTHING  *MESH_MTLID 1
*MESH_FACE    6:    A:    8 B:    9 C:    6 AB:    1 BC:    0 CA:    1  *MESH_SMOOTHING  *MESH_MTLID 1
*MESH_FACE    7:    A:    9 B:    7 C:    6 AB:    1 BC:    1 CA:    0  *MESH_SMOOTHING  *MESH_MTLID 1
*MESH_FACE    8:    A:   10 B:   11 C:    8 AB:    1 BC:    0 CA:    1  *MESH_SMOOTHING  *MESH_MTLID 1
*MESH_FACE    9:    A:   11 B:    9 C:    8 AB:    1 BC:    1 CA:    0  *MESH_SMOOTHING  *MESH_MTLID 1
*MESH_FACE   10:    A:   12 B:   13 C:   10 AB:    1 BC:    0 CA:    1  *MESH_SMOOTHING  *MESH_MTLID 1
*MESH_FACE   11:    A:   13 B:   11 C:   10 AB:    1 BC:    1 CA:    0  *MESH_SMOOTHING  *MESH_MTLID 1
*MESH_FACE   12:    A:   14 B:   15 C:   12 AB:    1 BC:    0 CA:    1  *MESH_SMOOTHING  *MESH_MTLID 1
*MESH_FACE   13:    A:   15 B:   13 C:   12 AB:    1 BC:    1 CA:    0  *MESH_SMOOTHING  *MESH_MTLID 1
*MESH_FACE   14:    A:    2 B:    3 C:   14 AB:    1 BC:    0 CA:    1  *MESH_SMOOTHING  *MESH_MTLID 1
*MESH_FACE   15:    A:    3 B:   15 C:   14 AB:    1 BC:    1 CA:    0  *MESH_SMOOTHING  *MESH_MTLID 1
*MESH_FACE   16:    A:    0 B:    2 C:    4 AB:    1 BC:    0 CA:    1  *MESH_SMOOTHING  *MESH_MTLID 0
*MESH_FACE   17:    A:   14 B:   12 C:    2 AB:    1 BC:    0 CA:    1  *MESH_SMOOTHING  *MESH_MTLID 0
*MESH_FACE   18:    A:    2 B:   12 C:    6 AB:    0 BC:    0 CA:    0  *MESH_SMOOTHING  *MESH_MTLID 0
*MESH_FACE   19:    A:    2 B:    6 C:    4 AB:    0 BC:    1 CA:    0  *MESH_SMOOTHING  *MESH_MTLID 0
*MESH_FACE   20:    A:    8 B:    6 C:   10 AB:    1 BC:    0 CA:    1  *MESH_SMOOTHING  *MESH_MTLID 0
*MESH_FACE   21:    A:   10 B:    6 C:   12 AB:    0 BC:    0 CA:    1  *MESH_SMOOTHING  *MESH_MTLID 0
*MESH_FACE   22:    A:   15 B:    3 C:   13 AB:    1 BC:    0 CA:    1  *MESH_SMOOTHING  *MESH_MTLID 1
*MESH_FACE   23:    A:    1 B:    5 C:    3 AB:    1 BC:    0 CA:    1  *MESH_SMOOTHING  *MESH_MTLID 1
*MESH_FACE   24:    A:    5 B:    7 C:    3 AB:    1 BC:    0 CA:    0  *MESH_SMOOTHING  *MESH_MTLID 1
*MESH_FACE   25:    A:    9 B:   11 C:    7 AB:    1 BC:    0 CA:    1  *MESH_SMOOTHING  *MESH_MTLID 1
*MESH_FACE   26:    A:   11 B:   13 C:    7 AB:    1 BC:    0 CA:    0  *MESH_SMOOTHING  *MESH_MTLID 1
*MESH_FACE   27:    A:   13 B:    3 C:    7 AB:    0 BC:    0 CA:    0  *MESH_SMOOTHING  *MESH_MTLID 1
```

```
}
}
*PROP_MOTIONBLUR 0
*PROP_CASTSHADOW 1
*PROP_RECVSHADOW 1
*MATERIAL_REF 0
}
```

Appendix D

LASER/F text output example

```
.......
0;-76.779938;-6.303203;158.877304;3;-77.04177856;-5.766724586;158.8773041;-77.12722778;-6.435009003;158.8773041;-76.17081451;-6.707874775;158.8773041;289.169342;383.953613;11.776645;
0;-76.836906;-6.748726;158.877304;3;-77.12722778;-6.435009003;158.8773041;-77.212677;-7.103293419;158.8773041;-76.17081451;-6.707874775;158.8773041;289.098053;383.574951;11.726176;
0;-73.910378;-2.206930;158.877304;3;-74.61624908;-2.302749872;158.8773041;-73.62005615;-2.520646811;158.8773041;-73.49482727;-1.79739356;158.8773041;289.300690;384.651520;11.869858;
0;-73.246254;-2.352195;158.877304;3;-73.62005615;-2.520646811;158.8773041;-72.62387085;-2.738543749;158.8773041;-73.49482727;-1.79739356;158.8773041;289.241150;384.334961;11.827482;
0;-71.645233;1.209465;158.877304;3;-72.1907196;1.161224961;158.8773041;-71.67568207;0.8005874753;158.8773041;-71.06930542;1.666581154;158.8773041;289.399719;385.178284;11.941087;
0;-71.301880;0.969040;158.877304;3;-71.67568207;0.8005874753;158.8773041;-71.16064453;0.4399500191;158.8773041;-71.06930542;1.666581154;158.8773041;289.338165;384.850708;11.896599;
0;-77.959511;-8.896979;158.877304;3;-77.38357544;-8.439862251;158.8773041;-78.42543793;-8.835281372;158.8773041;-78.06951141;-9.415793419;158.8773041;288.940613;382.740387;11.612098;
0;-78.654083;-9.160591;158.877304;3;-78.42543793;-8.835281372;158.8773041;-79.46730042;-9.230699539;158.8773041;-78.06951141;-9.415793419;158.8773041;289.069885;383.425629;11.704371;
0;-74.354416;-2.839228;158.877304;3;-74.61624908;-2.302749872;158.8773041;-74.70170593;-2.97103405;158.8773041;-73.74528503;-3.243899822;158.8773041;289.275330;384.516663;11.850902;
0;-74.411385;-3.284751;158.877304;3;-74.70170593;-2.97103405;158.8773041;-74.78715515;-3.639318466;158.8773041;-73.74528503;-3.243899822;158.8773041;289.256958;384.418976;11.837605;
0;-81.202568;-10.224276;158.877304;3;-81.71344757;-10.30827522;158.8773041;-80.89429474;-10.88185024;158.8773041;-80.99995422;-9.482700348;158.8773041;288.859406;382.310272;11.544813;
0;-79.669914;-9.972275;158.877304;3;-79.46730042;-9.230699539;158.8773041;-80.18080139;-10.05627441;158.8773041;-79.36164856;-10.62985039;158.8773041;288.807343;382.035065;11.511851;
0;-80.145584;-10.522658;158.877304;3;-80.18080139;-10.05627441;158.8773041;-80.89429474;-10.88185024;158.8773041;-79.36164856;-10.62985039;158.8773041;288.710327;381.522156;11.441745;
0;-81.493225;-9.799891;158.877304;3;-80.99995422;-9.482700348;158.8773041;-81.76628113;-9.608699799;158.8773041;-81.71344757;-10.30827522;158.8773041;289.072113;383.437622;11.699726;
0;-82.004112;-9.883892;158.877304;3;-81.76628113;-9.608699799;158.8773041;-82.5326004;-9.734700203;158.8773041;-81.71344757;-10.30827522;158.8773041;288.986481;382.983490;11.638865;
0;-71.706131;0.391710;158.877304;3;-71.16064453;0.4399500191;158.8773041;-71.67568207;0.8005874753;158.8773041;-72.28206635;-0.0654062033;158.8773041;289.329926;384.806854;11.892492;
0;-72.049492;0.632135;158.877304;3;-71.67568207;0.8005874753;158.8773041;-72.1907196;1.161224961;158.8773041;-72.28206635;-0.0654062033;158.8773041;289.390778;385.130676;11.934100;
1;-17.077219;79.491173;173.111893;3;-16.46870613;80.35720062;174.9570923;-18.07676315;78.06864166;172.7251129;-16.68618774;80.04768372;171.6534729;290.141113;361.616821;36.690037;
1;-4.468992;97.434990;174.453857;3;-3.821001053;98.35720062;174.9570923;-5.22630167;96.35720062;174.9570923;-4.3596735;97.59056854;173.4473724;290.235718;362.088531;37.086563;
1;-23.226072;70.740227;170.114761;3;-24.08383942;69.51947021;169.0461578;-22.08990669;72.35720062;169.9822388;-23.50447273;70.34401703;171.3159027;290.229004;362.055023;37.009136;
1;-13.852286;84.080849;170.912537;3;-13.50771904;84.57122803;169.323822;-13.18619061;85.02882385;172.2784882;-14.86294937;82.64248657;171.1352997;290.259766;362.208374;37.090649;
1;-34.331787;54.934761;174.147949;3;-33.38597488;56.28082275;174.9570923;-35.27759933;53.58869934;174.9570923;-34.33178711;54.93476105;172.5296783;290.116791;361.495422;36.743546;
1;-18.878458;76.927681;172.981934;3;-18.07676315;78.06864166;172.7251129;-19.27930641;76.35720062;174.9570923;-19.27930641;76.35720062;171.2635956;290.143188;361.626984;36.704018;
1;-25.201393;67.928986;168.277115;3;-25.33782768;67.7348175;166.6495056;-24.08383942;69.51947021;169.0461578;-26.18251038;66.5326767;169.1356659;290.285889;362.338959;37.220341;
1;-19.747740;75.690536;173.725922;3;-19.27930641;76.35720062;174.9570923;-20.68460655;74.35720062;174.9570923;-19.27930641;76.35720062;171.2635956;290.117249;361.497711;36.622646;
1;-21.370728;73.380730;167.290802;3;-20.43173027;74.71709442;168.5280762;-22.60427094;71.62516785;167.4320526;-21.07618141;73.79991913;165.912262;290.316223;362.490295;37.290436;
1;-32.114635;58.090176;161.743301;3;-32.66377258;57.30865479;160.6890564;-31.32406235;59.21530533;161.2929382;-32.35607147;57.74656677;163.2479248;290.473206;363.274963;37.922985;
1;-29.397537;61.957104;174.269653;3;-30.08905411;60.97294998;174.9570923;-29.66296768;61.5793457;172.8947754;-28.44059181;63.31901169;174.9570923;290.091003;361.367065;36.608097;
1;-30.084122;60.979969;168.420029;3;-30.89398956;59.82737732;168.1593323;-29.68161201;61.55281448;167.1376953;-29.67676163;61.55971909;169.9630737;290.282837;362.323700;37.254562;
1;-31.929663;58.353424;168.532532;3;-32.0304718;58.20995331;169.9053497;-32.86452484;57.0229454;167.5329132;-30.89398956;59.82737732;168.1593323;290.284119;362.330109;37.281216;
1;-26.854164;65.576790;170.503036;3;-26.80230141;65.65060425;172.4771271;-27.57767868;64.54709625;169.8963013;-26.18251038;66.5326767;169.1356659;290.274323;362.281189;37.207668;
1;-28.565010;63.141941;170.497147;3;-28.44059181;63.31901169;171.6320801;-29.67676163;61.55971909;169.9630737;-27.57767868;64.54709625;169.8963013;290.315613;362.487396;37.371059;
1;-21.708635;72.899818;168.647461;3;-20.43173027;74.71709442;168.5280762;-22.08990669;72.35720062;169.9822388;-22.60427094;71.62516785;167.4320526;290.255066;362.185089;37.082138;
.......
```

Appendix E

Workflow diagram

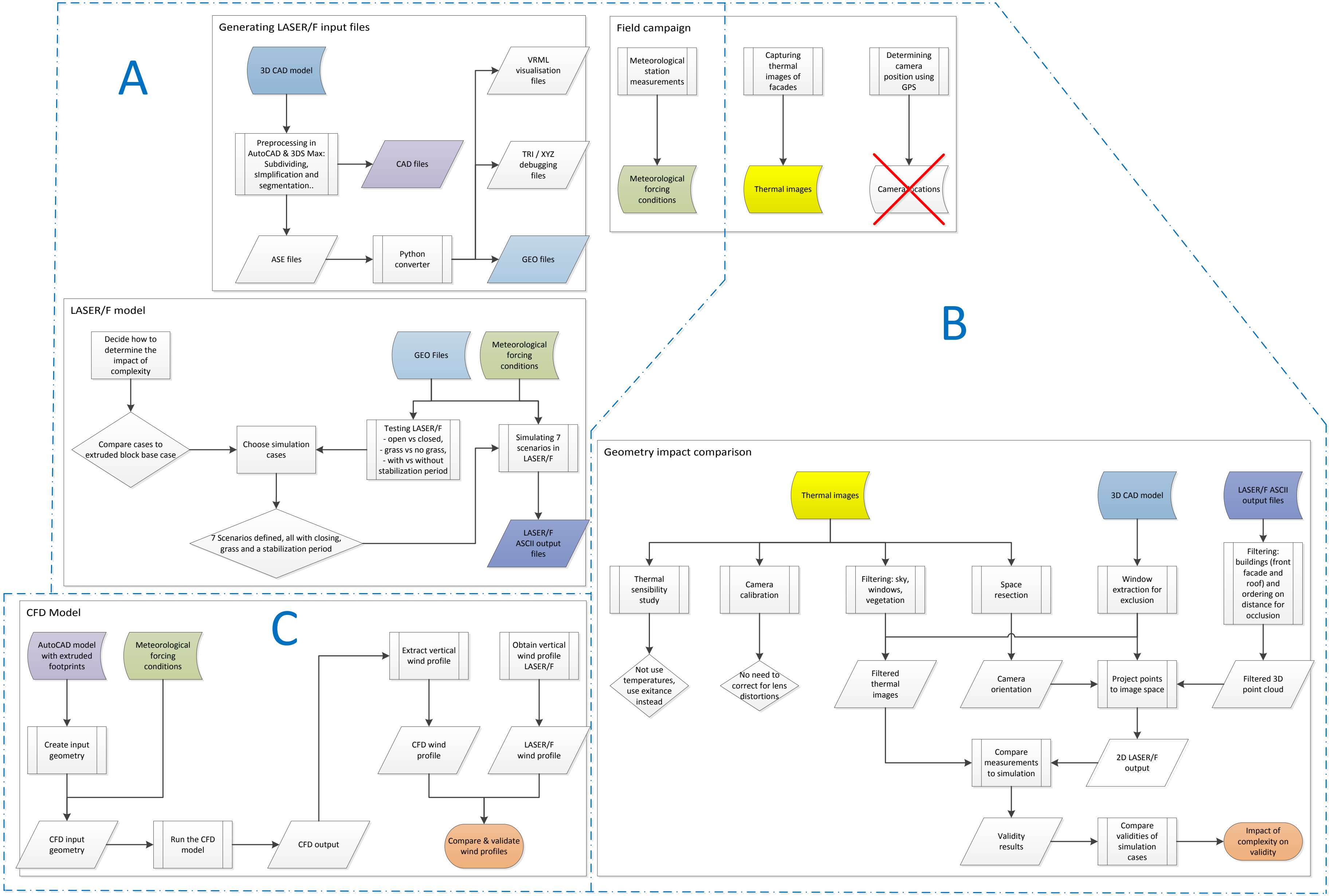

FIGURE E.1: Workflow diagram of the project

Bibliography

[1] T. R. Oke. The Energy Balance of an Urban Canyon. *Journal of Applied Meteorology*, 16(1):11–19, 1977. ISSN 00218952. doi: 10.1175/1520-0450(1977)016⟨0011:TEBOAU⟩2.0.CO;2. URL `http://journals.ametsoc.org/doi/abs/10.1175/1520-0450%281977%29016%3C0011%3ATEBOAU%3E2.0.CO%3B2`.

[2] T R Oke. Street design and urban canopy layer climate. *Energy and Buildings*, 11(1-3):103–113, 1988. ISSN 03787788. doi: 10.1016/0378-7788(88)90026-6. URL `http://linkinghub.elsevier.com/retrieve/pii/0378778888900266`.

[3] Xiaomin Xie, Zhen Huang, Jiasong Wang, and Zheng Xie. The impact of solar radiation and street layout on pollutant dispersion in street canyon. *Building and Environment*, 40(2):201–212, February 2005. ISSN 03601323. doi: 10.1016/j.buildenv.2004.07.013. URL `http://linkinghub.elsevier.com/retrieve/pii/S0360132304001763`.

[4] buildingSMART e.V., October 2012. URL `http://www.buildingsmart.de/2/2_02_03.htm`.

[5] Google Earth. Version 6.2, October 2012. URL `http://www.google.com/earth`.

[6] FLIR. *ThermaCAM Researcher Professional User's manual.* FLIR, 2011.

[7] P P Kastendeuch and G Najjar. Simulation and validation of radiative transfers in urbanised areas. *Solar Energy*, 83(3):333–341, 2009. ISSN 0038092X. URL `http://linkinghub.elsevier.com/retrieve/pii/S0038092X08002090`.

[8] T. R. Oke. *Boundary Layer Climates.* Methuen & Co, London, 2nd edition, 1987. ISBN 0416044220.

[9] Gerald Mills. Luke Howard, Tim Oke and the study of urban climates, 2009. URL `ams.confex.com`.

[10] World Urbanization Prospects - The 2011 Revision. Technical report, United Nations, Department of Economic and Social Affairs, Population Division, New York, 2012.

[11] Adil Rasheed and Darren Robinson. Multiscale modelling of urban climate. In Ecole Polytechnique Fédérale De Lausanne Solar Energy And Building Physics Laboratory, editor, *Building Simulation*, volume 6, pages 505–512, 2009. URL `http://biblion.epfl.ch/EPFL/theses/2009/4531/4531_abs.pdf`.

[12] U.S. Environmental Protection Agency. Reducing urban heat islands: Compendium of strategies, chapter 1: Urban heat island basics. Technical report, U.S. Environmental Protection Agency, Washington, 2008.

[13] Gerald Mills. The urban canopy layer heat island. Technical report, International Association for Urban Climate, 2004.

[14] Laura Kleerekoper, Marjolein van Esch, and Tadeo Baldiri Salcedo. How to make a city climate-proof, addressing the urban heat island effect. *Resources, Conservation and Recycling*, 64:30–38, October 2011. ISSN 09213449. doi: 10.1016/j.resconrec.2011.06.004. URL `http://linkinghub.elsevier.com/retrieve/pii/S0921344911001303`.

[15] A John Arnfield. Two decades of urban climate research: a review of turbulence, exchanges of energy and water, and the urban heat island. *International Journal of Climatology*, 23(1):1–26, 2003. ISSN 08998418. doi: 10.1002/joc.859. URL `http://doi.wiley.com/10.1002/joc.859`.

[16] T R Oke. The energetic basis of the urban heat island. *Quarterly Journal of the Royal Meteorological Society*, 108(455):1–24, 1982. ISSN 1477870X. doi: 10.1002/qj.49710845502. URL `http://onlinelibrary.wiley.com/doi/10.1002/qj.49710845502/abstract`.

[17] I N Harman and S E Belcher. The surface energy balance and boundary-layer over urban street canyons. *Quarterly Journal of the Royal Meteorological Society*, 132 (621):2749–2768, 2006. URL `http://dx.doi.org/10.1256/qj.05.185`.

[18] F Bourbia and F Boucheriba. Impact of street design on urban microclimate for semi arid climate (Constantine). *Renewable Energy*, 35(2):343–347, 2010. ISSN 09601481. doi: 10.1016/j.renene.2009.07.017. URL `http://linkinghub.elsevier.com/retrieve/pii/S0960148109003140`.

[19] Hideki Takebayashi and Masakazu Moriyama. Relationships between the properties of an urban street canyon and its radiant environment: Introduction of appropriate urban heat island mitigation technologies. *Solar Energy*, 86(9):2255–2262, September 2012. ISSN 0038092X. doi: 10.1016/j.solener.2012.04.019. URL `http://linkinghub.elsevier.com/retrieve/pii/S0038092X12001685`.

[20] T Susca, S R Gaffin, and G R Dell'osso. Positive effects of vegetation: urban heat island and green roofs. *Environmental Pollution*, 159(8-9):2119–2126, 2011. URL `http://www.ncbi.nlm.nih.gov/pubmed/21481997`.

[21] Rizwan Ahmed Memon, Dennis Y C Leung, and Chun-Ho Liu. Effects of building aspect ratio and wind speed on air temperatures in urban-like street canyons. *Building and Environment*, 45(1):176–188, 2010. ISSN 03601323. doi: 10.1016/j.buildenv.2009.05.015. URL `http://linkinghub.elsevier.com/retrieve/pii/S0360132309001346`.

[22] Marta J.N. Oliveira Panão, Helder J.P. Gonçalves, and Paulo M.C. Ferrão. Numerical analysis of the street canyon thermal conductance to improve urban design and climate. *Building and Environment*, 44(1):177–187, January 2009. ISSN 03601323. doi: 10.1016/j.buildenv.2008.02.004. URL `http://linkinghub.elsevier.com/retrieve/pii/S0360132308000309`.

[23] F.T. DePaul and C.M. Sheih. Measurements of wind velocities in a street canyon. *Atmospheric Environment (1967)*, 20(3):455–459, January 1986. ISSN 00046981. doi: 10.1016/0004-6981(86)90085-5. URL `http://linkinghub.elsevier.com/retrieve/pii/0004698186900855`.

[24] Sotiris Vardoulakis, Bernard E.a Fisher, Koulis Pericleous, and Norbert Gonzalez-Flesca. Modelling air quality in street canyons: a review. *Atmospheric Environment*, 37(2):155–182, January 2003. ISSN 13522310. doi: 10.1016/S1352-2310(02)00857-9. URL `http://linkinghub.elsevier.com/retrieve/pii/S1352231002008579`.

[25] R.J. Cole and N.S. Sturrock. The convective heat exchange at the external surface of buildings. *Building and Environment*, 12(4):207–214, January 1977. ISSN 03601323. doi: 10.1016/0360-1323(77)90021-X. URL `http://linkinghub.elsevier.com/retrieve/pii/036013237790021X`.

[26] X.-M. Cai, J.F. Barlow, and S.E. Belcher. Dispersion and transfer of passive scalars in and above street canyons—Large-eddy simulations. *Atmospheric Environment*, 42(23):5885–5895, July 2008. ISSN 13522310. doi: 10.1016/j.atmosenv.2008.03.040. URL `http://linkinghub.elsevier.com/retrieve/pii/S1352231008003051`.

[27] P. Salizzoni, L. Soulhac, and P. Mejean. Street canyon ventilation and atmospheric turbulence. *Atmospheric Environment*, 43(32):5056–5067, October 2009. ISSN 13522310. doi: 10.1016/j.atmosenv.2009.06.045. URL `http://linkinghub.elsevier.com/retrieve/pii/S1352231009005585`.

[28] YA Gayev and Eric Savory. Influence of street obstructions on flow processes within urban canyons. *Journal of Wind Engineering and Industrial ...*, 82:

89–103, 1999. URL `http://www.sciencedirect.com/science/article/pii/S0167610598002128`.

[29] Limor Shashua-Bar and Milo E. Hoffman. Geometry and orientation aspects in passive cooling of canyon streets with trees. *Energy and Buildings*, 35(1):61–68, January 2003. ISSN 03787788. doi: 10.1016/S0378-7788(02)00080-4. URL `http://linkinghub.elsevier.com/retrieve/pii/S0378778802000804`.

[30] T R Oke. The distinction between canopy and boundary-layer urban heat islands. *Atmosphere*, 14(4):268–277, 1976. doi: 10.1080/00046973.1976.9648422. URL `http://www.tandfonline.com/doi/abs/10.1080/00046973.1976.9648422`.

[31] L. Wu. An integration of a surface energy balance climate model with TIN and GRID in GIS. In *Third International Conference/Workshop on Integrating GIS and Environmental Modeling*, Santa Barbara, CA, 1996. NCGIA.

[32] Ian N Harman. *The energy balance of urban areas*. PhD thesis, University of Reading, 2003.

[33] Sami a. Al-Sanea. Thermal performance of building roof elements. *Building and Environment*, 37(7):665–675, July 2002. ISSN 03601323. doi: 10.1016/S0360-1323(01)00077-4. URL `http://linkinghub.elsevier.com/retrieve/pii/S0360132301000774`.

[34] TA Howell and SR Evett. The Penman-Monteith Method. *Bushland, Texas: USDA Agricultural Research Service*, 5646(806), 2004. URL `http://scholar.google.com/scholar?hl=en&btnG=Search&q=intitle:THE+PENMAN-MONTEITH+METHOD#0`.

[35] Frank P Incropera, David P DeWitt, Theodore L Bergman, and Adrienne S Lavine. *Fundamentals of Heat and Mass Transfer*, volume 6th of *Dekker Mechanical Engineering*. John Wiley & Sons, 2007. ISBN 9780471457282. URL `http://www.osti.gov/energycitations/product.biblio.jsp?osti_id=6008324`.

[36] Tania Landes, Pierre Grussenmeyer, and Georges Najjar. Télédétection et photogrammétrie, chaînons dans la détermination du climat urbain à Strasbourg. *Revue XYZ*, N°103:25–32, 2005.

[37] P P Kastendeuch. Laser/f geo file format. 19/06/2012.

[38] TH Kolbe. Representing and exchanging 3D city models with CityGML. *3D geo-information sciences*, pages 1–20, 2009. URL `http://www.springerlink.com/index/P3V0U3M226M114P0.pdf`.

[39] FLIR SC655 Technical Specifications.

[40] Time and Date AS, October 2012. URL `http://timeanddate.com/`.

[41] A. Krenzinger and A.C. de Andrade. Accurate outdoor glass thermographic thermometry applied to solar energy devices. *Solar Energy*, 81(8):1025–1034, August 2007. ISSN 0038092X. doi: 10.1016/j.solener.2006.11.014. URL `http://linkinghub.elsevier.com/retrieve/pii/S0038092X06003082`.

[42] T.A. Clarke and J.F. Fryer. The development of camera calibration methods and models. *Photogrammetric Record*, 16(91):pp 51–66, 1998.

[43] J.Y. Bouguet. Camera calibration toolbox for matlab. 2004.

[44] C Harris and M Stephens. A combined edge and corner detector. *Proc 4th Alvey Vision Conference*, 1988. URL `http://www.assembla.com/spaces/robotics/documents/abzMnAOEer3zB7ab7jnrAJ/download/harris88.pdf`.

[45] K Khoshelham. Photogrammetry. 2011.

[46] Bill Triggs, Philip F McLauchlan, Richard I Hartley, and Andrew W Fitzgibbon. Bundle Adjustment - A Modern Synthesis. *Vision Algorithms Theory and Practice*, 34099(298–375):298–372, 2000. doi: 10.1007/3-540-44480-7. URL `http://www.springerlink.com/index/PLVCRQ5BX753A2TN.pdf`.

[47] Noah Snavely, Steven M Seitz, and Richard Szeliski. Photo Tourism : Exploring Photo Collections in 3D. *Image Rochester NY*, 25(3):835–846, 2006. ISSN 07300301. doi: 10.1145/1141911.1141964. URL `http://portal.acm.org/citation.cfm?id=1141964`.

[48] Changchang Wu. VisualSFM: A Visual Structure from Motion System, 2011. URL `http://www.buildingsmart.de/2/2_02_03.htm`.

[49] Valéry Masson. A physically-based scheme for the urban energy budget in atmospheric models. *Boundary-layer meteorology*, (September 1999):357–397, 2000. URL `http://www.springerlink.com/index/X11713072476W703.pdf`.

[50] P Schrijvers. Digital terrain modeling. 2012.

[51] NASA Earth Observatory Glossary, 2012. URL `http://earthobservatory.nasa.gov/Glossary`.

[52] Warren M. Rohsenow, James P. Hartnett, and Young I. Cho. *Handbook of Heat Transfer*. McGraw-Hill, New York, 3 edition, 1998.

[53] Inc COMSOL. Comsol heat transfer module glossary, 2012. URL `http://www.comsol.com/products/heat-transfer/glossary`.

[54] N.A. Zaitseva. Arctic Climatology Project Arctic Meteorology Glossary, 2012. URL `http://nsidc.org/arcticmet/glossary`.

[55] Haider Taha. Urban climates and heat islands: albedo, evapotranspiration, and anthropogenic heat. *Energy and Buildings*, 25(2):99–103, 1997. ISSN 03787788. URL `http://linkinghub.elsevier.com/retrieve/pii/S0378778896009991`.

[56] Glossary of meteorolgy, 2012. URL `http://amsglossary.allenpress.com/glossary/browse?s=a&p=60`.

[57] W G Rees. *Physical Principles of Remote Sensing*, volume 37. Cambridge University Press, 2001. ISBN 0521669480. doi: 10.1111/j.1945-5100.2002.tb01113.x. URL `http://www.librarything.com/work/2066648/book/32217919`.

[58] R Lindenbergh. Digital terrain modeling. 2012.

[59] Cambridge advanced learner's dictionary, 2012. URL `http://dictionary.cambridge.org/dictionary/british/`.

[60] J Hinkler and SB Pedersen. Automatic snow cover monitoring at high temporal and spatial resolution, using images taken by a standard digital camera. *International Journal of . . .*, (October 2012):37–41, 2002. URL `http://www.tandfonline.com/doi/abs/10.1080/01431160110113881`.

[61] Matthieu Liger. *Uncooled carbon microbolometer imager*. PhD thesis, California Institute of Technology, 2006. URL `http://thesis.library.caltech.edu/3841`.

[62] John H Lienhard. *A heat transfer textbook*, volume 82 of *McGraw-Hill Higher Education*. Phlogiston Press, 2011. ISBN 0971383529. doi: 10.1115/1.3246887. URL `http://web.mit.edu/lienhard/www/ahtt.html`.

[63] DC Mulawa and EM Mikhail. Photogrammetric treatment of linear features. *International Archives of Photogrammetry and . . .*, 1988. URL `http://www.isprs.org/proceedings/XXVII/congress/part3/383_XXVII-part3-sup.pdf`.